

**SHORT RANGE ORDER AND CONTINUUM
EXCITATIONS IN FRUSTRATED MAGNETS**

by

Jiajia Wen

A dissertation submitted to The Johns Hopkins University in conformity with the
requirements for the degree of Doctor of Philosophy.

Baltimore, Maryland

October, 2014

© Jiajia Wen 2014

All rights reserved

Abstract

Magnetic materials generally develop magnetic long range order at low temperatures. This standard low temperature instability can however be suppressed in frustrated magnets, a set of magnetic materials where the selection of a particular low energy ground state is “frustrated” due to competing interactions and geometrical constraints. Such a magnetically disordered ground state, called “spin liquid”, represents a novel state of matter that promises exotic properties such as fractionalized excitations.¹

In this thesis, the magnetic properties of three candidate materials $\text{Pr}_2\text{Zr}_2\text{O}_7$, NiGa_2S_4 , and SrHo_2O_4 , all of which elude conventional magnetic long range order, are studied extensively. Neutron scattering is the experimental tool of choice in that it enables direct probing of spatial and temporal spin correlations, which arguably carry the most salient manifestations of a spin liquid state.

$\text{Pr}_2\text{Zr}_2\text{O}_7$ is conjectured to host a quantum spin ice state, a possible realization of $U(1)$ quantum spin liquid.² A recipe was developed for synthesis of high quality stoichiometric single crystalline $\text{Pr}_2\text{Zr}_2\text{O}_7$. Through elastic neutron scattering, quasi-

ABSTRACT

static low temperature spin correlations are found that resemble those of classical spin ice, while inelastic neutron scattering shows a dominant role for quantum spin fluctuations. Analysis of the data indicates these result from a combination of inter-spin interactions and inhomogeneous splitting of the single ion magnetic ground state doublets, which are not protected by time reversal symmetry and can be lifted by sufficiently anisotropic electric field environment. These findings highlight an intricate interplay between spin and lattice degrees of freedom that could be important in related materials. Indeed we shall see that the very fact that the energy scale for ordering is suppressed compared to the bare interactions leads to an inherent sensitivity to symmetry breaking impurities.

NiGa_2S_4 is a rare realization of undistorted spin-1 triangular lattice. Surprisingly only a short range ordered magnetic state is achieved at low temperature. Inelastic neutron scattering uncovers a broad yet dispersive magnetic spectrum that cannot be explained by conventional spin wave theory. The seemingly inconsistency between the continuum neutron spectrum and low temperature specific heat measurements which suggest the existence of coherent quasiparticles³ indicates the excitations could be of novel nature.

Elastic neutron scattering measurements on SrHo_2O_4 showed this material can be viewed as an assembly of two types of $J_1 - J_2$ Ising chains that have Néel ($\uparrow\downarrow\uparrow\downarrow$) and double-Néel ($\uparrow\uparrow\downarrow\downarrow$) ground states respectively. At low temperature the Néel chains develop three dimensional long range order, which causes the double-Néel chains to

ABSTRACT

freeze into a disordered incommensurate state. A “disorder by order” mechanism was proposed to account for this unusual spin disorder.

Primary Reader: Collin Broholm

Secondary Reader: Peter Armitage

Acknowledgments

First of all, I would like to express my sincere gratitude to my thesis advisor Collin Broholm for his continuous support, patience, and encouragement during my Ph.D. study. I deeply appreciate the knowledge and wisdom that I learned from him through numerous inspirational discussions. His guidance helped me grow not only as a researcher but also as a person. I cannot ask for a better role model that I will always look up to.

For this dissertation I would like to thank my defense committee members: Collin Broholm, Peter Armitage, Tyrel McQueen, Jonah Erlebacher, and Howard Katz for their time and help.

I would also like to thank Peter Armitage, Tyrel McQueen, Satoru Nakatsuji, and Oleg Tchernyshyov for helpful discussions and collaborations. Special thanks to Satoru Nakatsuji and his group for their generosity and hospitality during my visit to ISSP in 2011. I am also grateful to all professors in the department for their wonderful lectures, especially Zlatko Teseanovic whose lectures on Quantum Mechanics will always be one of my favorites.

ACKNOWLEDGMENTS

I feel indebted to Seyed Koohpayeh, Satoru Nakatsuji's group in particular Yusuke Nambu and Kenta Kimura, and Haifeng Li for their amazing crystals that make the study in this thesis possible. Many thanks to postdocs and my fellow graduate students that I have the privilege to work with and to ask advise from: Ivelisse Cabrera, Anirban Ghosh, Sunxiang Huang, Ssuyen Huang, Zhihao Hao, Jian Kang, Mingen Li, Wei Liu, Martin Mourigal, Yusuke Nambu, James Neilson, Kate Ross, Vivek Thampy, Yuan Wan, Weigang Wang, Jiadong Zang. I also wish to thank my current office mates Shan Wu and Wesley Fuhrman for the lively office environment and their friendship.

It gives me great pleasure in acknowledging the help and hospitality I received at various neutron facilities: John Copley, Yamali Hernandez, Juscelino Leao, Yiming Qiu, Jose A. Rodriguez-Rivera, Qiang Ye at NCNR NIST, Doug Abernathy, Georg Ehlers, V. Ovidiu Garlea, Garrett Granroth, Matthew Stone, Wei Tian at ORNL, Jiri Kulda, Paul Steffens at ILL.

My time at Hopkins was made fun in large part due to many friends I have made over the years. You have become a part of my life. I will miss my basketball buddies and the Sunday morning games, and I will never forget the many tournaments that we have fought through together.

Last but not least I thank my families for their unconditional love and support. Thank you Mum and Dad for always being there for me. Thank you Weiwei and Zaijian for being my sister and brother and for all the laughters and tears we shared

ACKNOWLEDGMENTS

growing up. And most of all thank you Xiaoge for being a loving and supportive wife and for being by my side during this ride. Thank you.

Contents

Abstract	ii
Acknowledgments	v
List of Tables	xi
List of Figures	xii
1 Introduction	1
2 Quantum Spin Ice $\text{Pr}_2\text{Zr}_2\text{O}_7$	14
2.1 Introduction	14
2.2 $\text{Pr}_2\text{Zr}_2\text{O}_7$ Sample Synthesis	18
2.2.1 Polycrystalline $\text{Pr}_{2+x}\text{Zr}_{2-x}\text{O}_{7-x/2}$	20
2.2.2 Single Crystal Synthesis of $\text{Pr}_2\text{Zr}_2\text{O}_7$	28
2.3 Spin Ice with Quantum Fluctuation	33
2.3.1 Crystalline Electric Field Level Scheme	33

CONTENTS

2.3.2	Bulk Properties: Magnetic Susceptibility and Specific Heat . . .	38
2.3.3	Elastic and Inelastic Neutron Scattering	42
2.4	Random Transverse Fields on a Quantum Spin Ice	52
2.5	Conclusion	66
3	Continuum Excitation in NiGa₂S₄	68
3.1	Introduction	68
3.2	Experimental Techniques	71
3.3	Experimental Results	72
3.4	Conclusion	83
4	Disorder from Order among ANNNI Spin Chains in SrHo₂O₄	84
4.1	Introduction	84
4.2	1 Dimensional ANNNI Model	85
4.3	Experimental Results	90
4.3.1	Single Ion Magnetic Anisotropy	90
4.3.2	Neutron Scattering from the Short Range Ordered State . . .	92
4.3.3	Zig-Zag Spin Ladders and the ANNNI Model	94
4.3.4	Magnetic Long Range Order	98
4.3.5	Static magnetic moment size	104
4.4	Conclusion	110
5	Conclusion	111

CONTENTS

A Neutron Scattering	114
A.1 Basic Properties of Neutrons	114
A.2 Production and Detection of Neutrons	115
A.3 Neutron Scattering Cross-Section and Correlation Functions	115
B Vanadium Normalization of neutron scattering from $\text{Pr}_2\text{Zr}_2\text{O}_7$	118
B.1 Basic Idea	118
B.2 Elastic VS Inelastic	119
C $\text{Pr}_2\text{Zr}_2\text{O}_7$ Random Phase Approximation	121
Bibliography	126
Vita	148

List of Tables

2.1	Rietveld refinements results for $\text{Pr}_{2+x}\text{Zr}_{2-x}\text{O}_{7-x/2}$. ⁴	27
2.2	Experimental CEF parameters for $\text{Pr}_2\text{Zr}_2\text{O}_7$ in meV. ⁵	37
2.3	CEF spectrum and wave functions for $\text{Pr}_2\text{Zr}_2\text{O}_7$. ⁵	38

List of Figures

1.1	Long range orders in the square $J_1 - J_2$ Heisenberg model. (a) with dominant J_1 the ground state is a Néel state. (b) with dominant J_2 the ground state is instead a stripe state.	5
1.2	Geometrically frustrated lattices. (a) triangular lattice, (b) kagome lattice, (c) pyrochlore lattice.	6
1.3	(a)6 degenerate ground state configurations in one tetrahedron in spin ice. Red and black arrows correspond to “out” and “in” spins. Bottom 3 states are the time reversal partner of the top 3 states. (b)2-in 2-out ice rule in cubic water ice: two protons (blue spheres) are closer to the central oxygen (red spheres) while the other two are further away. ⁵ . .	8
1.4	Deconfined magnetic monopoles in spin ice. (a)Spin ice ground state with ice rule satisfied in all tetrahedra. (b)Flipping one spin from the ground state creates net magnetic charges(magnetic monopoles) on neighboring tetrahedra. (c)These pair of monopoles can be separated without any further energy cost by subsequent spin flips.	10
2.1	$U(1)$ quantum spin liquid exist in an extended parameter space around the classical spin ice. ⁶	17
2.2	Crystal structure of $\text{Pr}_2\text{Zr}_2\text{O}_7$. Yellow, green, and red spheres represent Pr, Zr, and O atoms respectively. Pr and Zr each form interpenetrating pyrochlore lattices.	19
2.3	Polycrystalline $\text{Pr}_2\text{Zr}_2\text{O}_7$ before(frame (a)) and after(frame (b)) sintering in Argon atmosphere. (c)A representative $\text{Pr}_2\text{Zr}_2\text{O}_7$ single crystal grown under 1 bar static high-purity argon atmosphere using an optical floating zone image furnace. ⁴	21
2.4	Lattice parameters of polycrystalline $\text{Pr}_{2+x}\text{Zr}_{2-x}\text{O}_{7-x/2}$ at different x shows an increase in lattice parameter as the Pr/Zr ratio increases. The solid line is a linear fit through the data points, which corresponds to $da/dx = 0.37 \text{ \AA}$. ⁴	22

LIST OF FIGURES

2.5	T -dependence of inverse magnetic susceptibility (a) and specific heat (b) of polycrystalline $\text{Pr}_{2+x}\text{Zr}_{2-x}\text{O}_{7-x/2}$ samples. Insets zoom in at low temperatures and demonstrate systematic changes in bulk properties as x varies. ⁴	24
2.6	Curie-Weiss fitting results of magnetic susceptibility show changes of effective moment size P_{eff} and Curie-Weiss temperature CW T as a function of x	25
2.7	Rietveld refinement of synchrotron X-ray data of $\text{Pr}_{2+x}\text{Zr}_{2-x}\text{O}_{7-x/2}$ for (a) $x = 0$, (b) $x = 0.02$, and (c) $x = +0.02$. (d) As an example of measurement sensitivity to Pr/Zr site mixing, the change in model intensity for the (311) pyrochlore-only reflection for various mixing ratios is compared to the observed data for $x = 0$. (e) The changes in the (311) pyrochlore reflection with composition is accurately modeled by the changes in Pr/Zr ratio, without any additional Pr/Zr mixing. (f) The ratio of mean square displacements ($\langle u_1^2 \rangle / \langle u_3^2 \rangle$) of Pr versus x , with a guide to the eye. ⁴	26
2.8	SEM back scattered micrographs of cross sections from the center (large pictures) and surface (smaller pictures on the top right) of $\text{Pr}_2\text{Zr}_2\text{O}_7$ single crystals grown at (a) 0 rpm, (b) 3 rpm, (c) 6 rpm and (d) 12 rpm. A spinodal decomposition is shown for the growth at 0 rpm, while application of the rotation of 3, 6 and 12 rpm produces a more uniform internal microstructure, with the highest rotation rates driving excess Pr to the edges producing inhomogeneity at the surface. ⁴	30
2.9	Lattice parameter of $\text{Pr}_2\text{Zr}_2\text{O}_7$ single crystals grown at different growth rates. Red dashed line shows the lattice parameter of stoichiometric polycrystalline $\text{Pr}_2\text{Zr}_2\text{O}_7$	31
2.10	Temperature dependence of inverse magnetic susceptibility (a) and specific heat (b) of single crystalline samples grown at different growth rates. Insets show closer look at low temperatures. A crystal grown under optimized conditions exhibits the same physical properties as the stoichiometric powder sample, demonstrating its high quality. ⁴	32
2.11	$E - Q$ slices measured on $\text{Pr}_2\text{Zr}_2\text{O}_7$ at 7.8 K with incident neutron energy of 40 meV(a) and 120 meV(b). Blue arrows indicate the flat modes that are inferred to be CEF transitions.	34
2.12	Combined neutron spectrum obtained with two different incident beam energies, $E_i = 40$ meV and 120 meV at $T = 7.8$ K. The blue dashed line denotes fitted backgrounds. The red solid line is the calculated best fit. Inset: Temperature dependence of the inverse magnetic susceptibility. The red solid line in the inset is the calculated best fit based on the same crystal field parameters (Table. 2.2 and Table. 2.3) as used to described the inelastic neutron scattering data. ⁵	36

LIST OF FIGURES

- 2.13 (a) Real part of the AC-susceptibility (χ'). Inset: Inverse DC-susceptibility from 10 to 2 K. (b) Imaginary part of the AC-susceptibility (χ''). Inset: Measurement frequency vs. inverse freezing temperature defined as the peak temperature for $\chi''(T)$. The solid line denotes a fit to the Arrhenius law, which yields an activation energy $\Delta_\chi = 1.6$ K.⁵ 40
- 2.14 (a) Magnetic and nuclear part of the specific heat C_{MN} for $\text{Pr}_2\text{Zr}_2\text{O}_7$ after subtracting lattice and CEF contributions in zero field (open blue circle). A refined estimate $C_M = C_{MN} - C_N$ (filled blue circle) was obtained by subtracting a scaled nuclear Schottky-like anomaly (solid blue line). C_M for $\text{Dy}_2\text{Ti}_2\text{O}_7$ ⁷ is also shown for comparison (filled green square). Inset: C_M versus $1/T$ on a semi-logarithmic scale. The solid line denotes a fit to an Arrhenius law between 2 to 0.2 K, which yields an activation energy of 0.72(1) K. (b) Magnetic entropy ΔS_M (filled blue circle) for $\text{Pr}_2\text{Zr}_2\text{O}_7$ calculated from C_M . Open green squares show ΔS_M for $\text{Dy}_2\text{Ti}_2\text{O}_7$.⁷ The dashed black lines denote the entropy for a two level system ($R \ln 2$) and the spin ice entropy defined as the difference between $R \ln 2$ and the Pauling entropy of $(1/2)(\ln(3/2)/\ln 2)R \ln 2 = 0.292R \ln 2$.⁵ 43
- 2.15 (a) Inelastic \mathbf{Q} -map with energy transfer of 0.25 meV obtained after subtracting the corresponding data at 15 K as background. The broad diffuse scattering pattern carries the symmetry of the crystal but cannot be associated with phonon scattering, which is concentrated around strong nuclear Bragg peaks at low energies. Instead we associate it with inelastic magnetic scattering. The fact that the scattering is wave vector dependent further links it to inter-site quantum spin dynamics. (b) Elastic \mathbf{Q} -map with pinch points at (002), (111), and $(\bar{1}\bar{1}1)$. By subtracting 22 K data from 0.1 K data to cancel elastic nuclear scattering processes at Bragg peaks, we obtain quasi-static spin correlations on the time scale of $\tau = \hbar/\delta E = 2$ ps. The black ellipses at (002) in \mathbf{a} and \mathbf{b} indicate the full width at half maximum instrumental resolution.⁵ 45
- 2.16 Temperature dependent elastic neutron scattering maps around the absent Bragg peak (002) measured with $E_f = 2.7$ meV. A map of intensity acquired at 15 K was used to subtract out nuclear scattering contributions. (a), (c), (e), and (g) show experimental data at 4.25 K, 1.5 K, 0.5 K, and 0.1 K, while (b), (d), (f), and (h) show the corresponding best fit based on Eq. 2.7. 47

LIST OF FIGURES

2.17	Temperature dependent inelastic neutron scattering spectra at $\mathbf{Q} = (003)$ after subtraction of data measured at 15 K. A correction to the monitor rate was applied to account for order contamination in the unfiltered incident beam. The fitting curve and the corresponding background resulting from subtraction of magnetic scattering at $T = 15$ K to derive Γ are shown by red solid and blue dashed curves, respectively. The solid black bar represents the instrumental energy resolution. . .	50
2.18	(a)Temperature dependence of the spin ice correlation length ξ_{ice} (left) and the relaxation rate Γ (right). The black solid line denotes $1/\xi_{\text{ice}} = 1/\xi_0 + A/\exp(\Delta_\chi/T)$ with the activation energy fixed at the value of $\Delta_\chi = 1.62(3)$ K. The red solid line shows $\Gamma(T) = \sqrt{(\Gamma_0)^2 + (Ck_B T)^2}$, where $C = 1.4(2)$. The black horizontal dashed line indicates the mean distance between 1% of the Pr sites, which according to synchrotron X-ray analysis are occupied by Zr. (b)Temperature dependent elastic magnetic neutron scattering cross section from $\text{Pr}_2\text{Zr}_2\text{O}_7$ inferred from fits in Fig. 2.16. These data represent the quasi-static total moment squared, averaged over the momentum space where the data were collected. The observed elastic scattering represents just 7(2)% of the elastic scattering cross section associated with a fully frozen state. ⁵ . .	51
2.19	Single crystalline $\text{Pr}_2\text{Zr}_2\text{O}_7$ assemblies used for neutron scattering measurements in (a) (HHL) plane and (b) $(HK0)$ plane respectively. . .	53
2.20	Momentum space averaged spectrum for $0.5 \text{ \AA}^{-1} \leq \mathbf{Q} \leq 2.2 \text{ \AA}^{-1}$ in the corresponding scattering plane. (a) Spectrum for $\mathbf{H} \parallel (001)$, $T = 1.4$ K (black circle) and $\mathbf{H} \parallel (1\bar{1}0)$, $T = 0.2$ K (red circle). $ \mathbf{H} = 2$ T in both measurements. Inset is a schematic representation of the relative orientation of the applied field and the spin directions. (b) Field dependent spectrum for $\mathbf{H} \parallel (001)$ at $T = 1.4$ K. The distribution of transverse field $\rho(\Delta)$ extracted from the spectrum was shown in the inset. The corresponding Zeeman gap energies are shown as dashed vertical lines, data points above which were used to calculate $\rho(\Delta)$. For 0 field, data points with $E \geq 0.1$ meV were used to avoid elastic line. (c) Temperature dependent spectrum for $\mathbf{H} \parallel (001)$, 4 T. A thermal distribution factor F_{th} were applied to the data.	56
2.21	Field dependent $\mathbf{Q} - E$ slice for $\mathbf{H} \parallel (001)$, $T = 1.4$ K. Data were integrated along $(0K0)$ for $1 \text{ (r.l.u.)} \leq K \leq 3 \text{ (r.l.u.)}$. (a),(b),and (c) shows corresponding data for $ \mathbf{H} = 4$ T, 2 T, and 0 T	57

LIST OF FIGURES

2.22	\mathbf{Q} -maps in (HLL) plane. Data were folded into the first quadrant for optimal statistics. (a) and (c) shows data measured with 7 Å incident neutron wavelength at 0.05 K, 0 T with energy integration of [0.1,0.3] meV and [0.3,0.8] meV respectively. (e) shows data with 5 Å incident neutron wavelength at 0.2 K, 3.5 T with energy integration of [0.1,0.5] meV. (b),(d), and (f) shows corresponding calculation of neutron cross-section within RPA.	59
2.23	Longitudinal elastic cuts for magnetic (200) and nuclear (220) peaks with $\mathbf{H} = 6 \text{ T} \parallel (001)$, $T = 1.5 \text{ K}$	62
3.1	Crystal structure of NiGa_2S_4 . (a) NiGa_2S_4 consists of a central layer of NiS_6 sandwiched between two layers of GaS_4 . (b) The diffraction data indicate magnetic Ni^{2+} ions form perfect triangular lattices. . . .	71
3.2	Assembly of 19 single crystalline NiGa_2S_4 ($\sim 1 \text{ g}$) co-aligned in ($HK0$) plane.	73
3.3	Neutron spectrum of NiGa_2S_4 measured at 2 K along different directions. (a) Spectrum originating from the critical wave vector \mathbf{q}_0 perpendicular to $\Gamma - K$ direction. (b) Spectrum along three high symmetry directions of the reciprocal lattice: $\Gamma - K$, $K - M$, and $M - \Gamma$. Black ellipses show representative instrumental resolutions. (c) Elastic scan along $\Gamma - K$ direction in frame (d). Solid line shows a Gaussian fit to the data. The vertical dashed line shows the commensurate position of $(1/6, 1/6, 0)$. (d) Elastic scattering map measured at 2 K. Measurement at 20 K were used to subtract out nuclear contributions. Dashed lines show Brillouin zone boundaries.	74
3.4	Neutron spectrum of NiGa_2S_4 at \mathbf{q}_0 , K, and M points obtained by constant \mathbf{q} cuts through data presented in Fig. 3.3(b). Black bars at $E = 3 \text{ meV}$ and $E = 8 \text{ meV}$ show the corresponding energy resolution.	75
3.5	Representative constant energy slices of NiGa_2S_4 measured at 2 K. Black circles at the K points show calculations of instrumental momentum space resolutions.	77
3.6	Thermal evolution of dynamical spin correlations in NiGa_2S_4 . (a) Constant energy slices measured with $E = 1.5 \text{ meV}$ at different temperatures. Intensity at 90 K were scaled by a factor of 2 for better visualization. (b) Fitting results of experimental data in frame (a) as described in the main text.	81
3.7	Temperature dependence of parameters C_0 and χ_0 as extracted from fitting shown in Fig. 3.6.	82

LIST OF FIGURES

4.1	(a) A linear spin chain with nearest neighbor interaction J_1 and next nearest neighbor interaction J_2 as described by the 1D ANNNI model. (b) Equivalently the 1D ANNNI model also describes a zig-zag spin ladder with inter-leg interaction J_1 and intra-leg interaction J_2	86
4.2	Contours of constant modulation q for 1D ANNNI model in $(k_B T/J_1, \kappa = -J_2/J_1)$ plane. The solid line is the disorder line below which $G(r)$ is a pure exponential function. ⁸	89
4.3	(a) Crystallographic unit cell of SrHo_2O_4 . Sr atoms were omitted for clarity. Red and Blue spheres show two distinct Ho sites, and the corresponding arrows show the Ising spin directions. (b) Magnetic lattice formed by Ho and a schematic representation of the spin structure determined by neutron diffraction. ⁹	91
4.4	(a) Magnetic susceptibility of SrHo_2O_4 along three axes measured under 200 Oe. Dashed lines show fits to J_1-J_2 Ising models. (b) Magnetic heat capacity over T versus T . (c) shows the entropy versus T . The dashed line shows the entropy of an Ising doublet. ⁹	93
4.5	CEF level schemes for Ho1 and Ho2 calculated with point charge approximation. Thick and thin lines represent doublets and singlets. Both sites are found to have a magnetic doublet ground state.	94
4.6	Magnetic susceptibility along three crystalline axes calculated based the point charge model CEF level scheme for (a)Ho1 and (b)Ho2. Ho1 is found to have an Ising doublet ground state along c while Ho2 has an Ising doublet along b	95
4.7	T -dependent elastic magnetic neutron scattering from the SRO of SrHo_2O_4 . (a)(c) show measurements in the $(HK0)$ plane while (b)(d) are from the $(0KL)$ plane. Measurements at 50 K were subtracted to eliminate nuclear scattering. (e) and (f) show J_1-J_2 model calculations at 1.4 K with exchange constants determined from Fig. 4.2(a). ⁹	96
4.8	Thermal evolution of inter-chain correlations for (a)red Ho1 chains along b , and blue Ho2 chains (b)along b and (c)along a	100
4.9	Inter-chain correlations for blue sites probed by neutrons. Filled and empty circles are from $H-$ and $K-$ scans at $(00\frac{1}{2})$ measured at 0.28 K. The solid lines show fits to the data. Insert shows sharp component of $H-$ scan in detail, the horizontal bar is the instrumental resolution. Data from different sample orientations are normalized by the peak count rate. ⁹	101

LIST OF FIGURES

4.10 Spin correlations versus T in SrHo_2O_4 probed by neutrons. (a)-(d) show results from L -scans at (030) (red) and $(00\frac{1}{2})$ (blue) that probe correlations along red and blue chains respectively. (a)(b) show integrated intensities. (c) shows the peak shift from $(00\frac{1}{2})$. The inset shows the peak shift along \mathbf{c}^* from $(0K\frac{1}{2})$. The dashed line shows the predicted shift based on the $J_1 - J_2$ model. (d) shows the inverse correlation length κ_c determined by half width at half maximum of resolution convoluted Lorentzian fits. (e) shows κ_b extracted from K -scans at $(00\frac{1}{2})$. Black dashed lines indicate T_N and T_S . Blue dashed lines in (c)(d) are ANNNI model calculations.⁹ 103

4.11 Schematic representation of the spin structure in SrHo_2O_4 . 4 Ho1 spins and 4 Ho2 spins in the unit cell are labeled by 1-4 respectively. 106

4.12 Magnetic moment size refinements. Filled circles are the experimental L -integrated intensities for peaks with integer L index in (a) and half odd integer L index in (b) that correspond to Ho1 and Ho2 sites respectively. Open circles show the fitting results as described in the text. All experimental peak intensities are plotted in ascending order. 107

C.1 (a) Conventional unit cell of Pyrochlore lattice. It can be considered as a FCC lattice of tetrahedra as shown in (b). One particular way of labeling spins is shown. 122

Chapter 1

Introduction

One of the hallmarks of contemporary condensed matter physics is the discovery and understanding of various exotic “emergent” phenomena such as superconductivity and superfluidity in systems with strongly correlated particles.^{10,11} Even though the electromagnetic interactions between the underlying particles are generally well understood, it is difficult and in some cases perhaps impossible to predict these emergent phenomena from first principle deduction due to the large number of interacting degrees of freedom involved. And yet it is possible to classify, probe, and understand the properties of the collective states of matter and their emergent quasi-particles.

A general organizing principle to describe a subset of these collective emergent state of matter is associated with the phenomenon of broken symmetry.¹² As an example, take the magnetic insulator which is the main focus of this thesis. Experimental realization of such systems are usually found in Mott insulators¹³ where due

CHAPTER 1. INTRODUCTION

to strong on-site Coulomb repulsion, electrons are well localized on distinct lattice sites. The low energy effective Hamiltonian that describes such interacting localized electrons can be formulated in terms of interacting spins.¹⁴ An example of this is shown in the following, the Heisenberg Hamiltonian

$$\mathcal{H} = - \sum_{i,j} J_{ij} \mathbf{S}_i \cdot \mathbf{S}_j \quad (1.1)$$

Here \mathbf{S} is the spin operator and J_{ij} is the exchange constant describing in this case an isotropic interaction between spins located at site i and j . This Hamiltonian is invariant under global spin rotation. The paramagnetic phase at high temperature ($T \gg J$) indeed obey this symmetry, where due to thermal fluctuation each spin is free to rotate and the thermal average is identical to 0, $\langle \mathbf{S} \rangle = 0$, as required by the rotational symmetry. At lower temperature ($T \sim J$) when the inter-spin interactions becomes more important the whole system might enter a long range order phase with $\langle \mathbf{S} \rangle \neq 0$, such as in the familiar ferromagnets where below the Curie temperature the spins have non-zero thermal average and all point in the same direction. This emergent long range ordered state spontaneously breaks the rotational symmetry of the spin Hamiltonian. An order parameter, $\langle \mathbf{S} \rangle$ in the case of a ferromagnet, can be introduced to describe the symmetry breaking. It is 0 in the symmetric phase but when it takes on a non-zero value the symmetry is broken. The nature of the broken symmetry has important implication for the low energy dynamics.¹²

CHAPTER 1. INTRODUCTION

In the case of continuous symmetry breaking as in the Heisenberg model, the low energy excitations are gapless bosonic Goldstone modes,¹⁵ which are called magnons in magnetic materials.

Symmetry breaking provides a powerful and unified recipe to describe and study magnetic long range orders and their excitations in various magnetic materials. There is however another more intriguing aspect of the problem: Does the ground state for an interacting spin Hamiltonian always break symmetries of the Hamiltonian? If not, what do the spin-spin correlations look like in the ground state and what are the corresponding low energy excitations? Is there an “order parameter”-like quantity that allows classification of such states? The answer to the first question, fortunately, is no, and in this thesis I will try to provide insight to the second question by probing magnetic materials that do not form conventional magnetic long range order using neutron scattering. Finally, there has been tremendous theoretical progress towards answering the third question and the data that I provide may eventually help to constrain such theories.^{16,17}

Such a non-symmetry-breaking ground state is called a spin liquid¹ in analogy to conventional liquids, where molecules are highly correlated in the absence of static long range order. To understand why a broken symmetry state is not always favored let us consider two $S = \frac{1}{2}$ spins subject to an isotropic antiferromagnetic exchange interaction: $\mathcal{H} = -JS_1 \cdot S_2$, $J < 0$. For a static Néel order state where one spin points up and the other points down ($|\uparrow\rangle|\downarrow\rangle$), each spin carries a bond energy of $\frac{1}{8}J$,

CHAPTER 1. INTRODUCTION

while for an isotropic valence bond state where the two spins form a total spin 0 singlet state ($\frac{1}{\sqrt{2}}(|\uparrow\rangle|\downarrow\rangle - |\downarrow\rangle|\uparrow\rangle)$), each spin carries a bond energy of $\frac{3}{8}J$. Thus in this case it is the non-symmetry-breaking valence bond state that has the lower energy. Though only two spins are considered here, it has been found that the ground state for 1-dimensional spin- $\frac{1}{2}$ chain is indeed a spin liquid,¹⁸ and more interestingly the elementary excitations are fractionalized spin- $\frac{1}{2}$ spinons¹⁹ that have been observed in materials such as KCuF_3 .²⁰

One also finds that the bond energy per spin in the Néel state goes down linearly as the number of neighboring sites increase, while it is invariant in the valence bond state. This suggests that a spin liquid is energetically less favorable in higher dimensions. This is certainly true for bipartite lattices such as the square lattice with only nearest neighbor interactions. However, the situation becomes less clear when competing interactions are introduced and when the geometry of the lattice becomes more complicated.

Firstly let us examine the effect of competing interactions. We use spin- $\frac{1}{2}$ square lattice $J_1 - J_2$ Heisenberg model as an example:

$$\mathcal{H} = - \sum_{\langle i,j \rangle} J_1 \mathbf{S}_i \cdot \mathbf{S}_j - \sum_{\langle\langle i,j \rangle\rangle} J_2 \mathbf{S}_i \cdot \mathbf{S}_j, \quad (1.2)$$

where $J_1, J_2 < 0$, $\langle i, j \rangle$ and $\langle\langle i, j \rangle\rangle$ denote nearest and next nearest neighbor. The nearest and next nearest neighbor interactions J_1 and J_2 are in competition be-

cause they favor different spin configurations. It is easy to see that the ground states in the limiting cases of $J_2/J_1 \ll 1$ and $J_2/J_1 \gg 1$ are Néel and stripe states respectively, as shown in Fig. 1.1. When $J_2/J_1 = 0.5$, this model is maximally frustrated

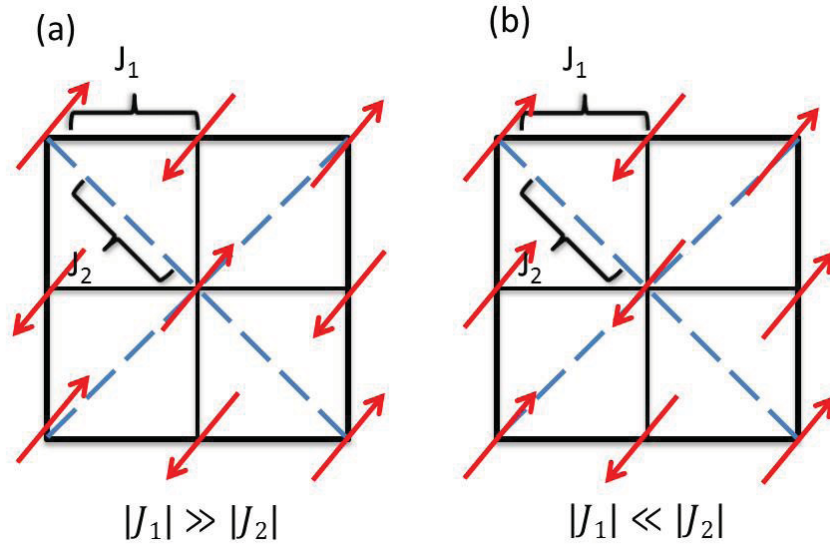


Figure 1.1: Long range orders in the square $J_1 - J_2$ Heisenberg model. (a) with dominant J_1 the ground state is a Néel state. (b) with dominant J_2 the ground state is instead a stripe state.

as the Néel and stripe states become energetically degenerate (in the classical sense) and the resultant strong quantum fluctuation might destroy the long range orders. A recent numerical study on cylinders of circumference $L_y = 3 - 14$ and lengths $L_x \geq 2L_y$ indicates that a topological quantum spin liquid state exists around this point with $0.41 \leq J_2/J_1 \leq 0.62$.²¹

The possible realization of quantum spin liquid in such a simple square $J_1 - J_2$ model provides optimism that such states might be discovered in real materials. However, it is difficult to experimentally tune the J_2/J_1 ratio in a particular material.

CHAPTER 1. INTRODUCTION

In this sense, the other route to realize a spin liquid, through geometrical frustration,²² has its advantage since it depends less on fine tuning of exchange constants.

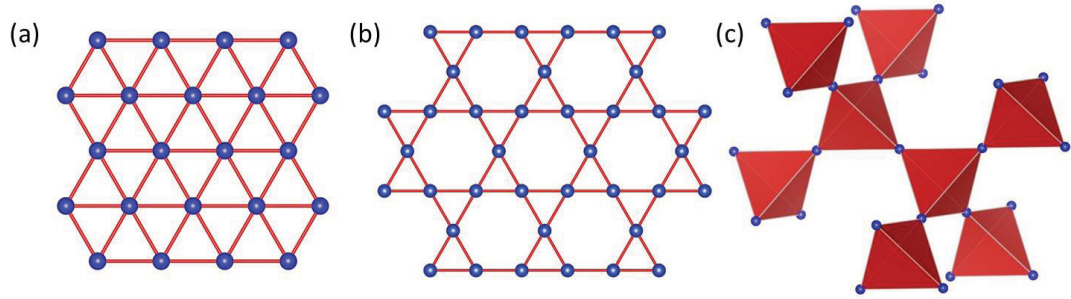


Figure 1.2: Geometrically frustrated lattices. (a) triangular lattice, (b) kagome lattice, (c) pyrochlore lattice.

Geometrical frustration generally arises in lattices with a triangular motif. Three representative lattices are shown in Fig. 1.2. These are the triangular lattice consisting of edge sharing triangles, the kagome lattice based on corner sharing triangles, and the pyrochlore lattice based on corner sharing tetrahedra. Such lattices are geometrically frustrated in the sense that the bond energies cannot be simultaneously minimized due to a geometrical constraint. As a result there could be a macroscopically large number of degenerate states at low energy which could enhance fluctuations and suppress long range orders.

To illustrate this, we consider a classical spin model on the pyrochlore lattice. On each corner of the tetrahedron resides an Ising spin, a classical vector that can either points towards or away from the tetrahedron center. Each Ising spin is ferromagnet-

CHAPTER 1. INTRODUCTION

ically coupled to its nearest neighbors:

$$\mathcal{H} = - \sum_{\langle i,j \rangle} J(\mathbf{e}_i \cdot \mathbf{e}_j) \sigma_i \sigma_j \quad (1.3)$$

Here \mathbf{e}_i is the unit vector representing the Ising spin direction, $\sigma = \pm 1$, and $J > 0$. To see how frustration arises, let us consider the bond energy within a single tetrahedron. With ferromagnetic nearest neighbor interaction $J > 0$, the bond energy between neighboring sites is lowest when one spin points into while the other points away from the center of the tetrahedron. This, however, cannot be satisfied simultaneously on all of the 6 bonds due to the geometry of the tetrahedron since two spins coupled to the same spin are also coupled to each other. The lowest energy Ising spin configuration on the tetrahedron consists of two spins pointing in and two spins pointing out. In this state 4 bonds out of 6 are satisfied. This local 2-in 2-out constraint on the ground state is equivalent to the constraints on proton locations that lead to proton disorder in cubic water ice (Fig. 1.3(b)). There each oxygen atom at the center of a tetrahedron has two closer and two more distant protons. This spin model is thus given the name of “spin ice”.²³

The 2-in 2-out ice rule does not specify a unique ground state. On just one tetrahedron it already gives rise to 6 fold degeneracy that corresponds to 6 ways of picking 2 out of 4 spins to point out (Fig. 1.3(a)). 3 of them are not related by time reversal symmetry ($\sigma \rightarrow -\sigma$) and are accidentally degenerate due to the particular

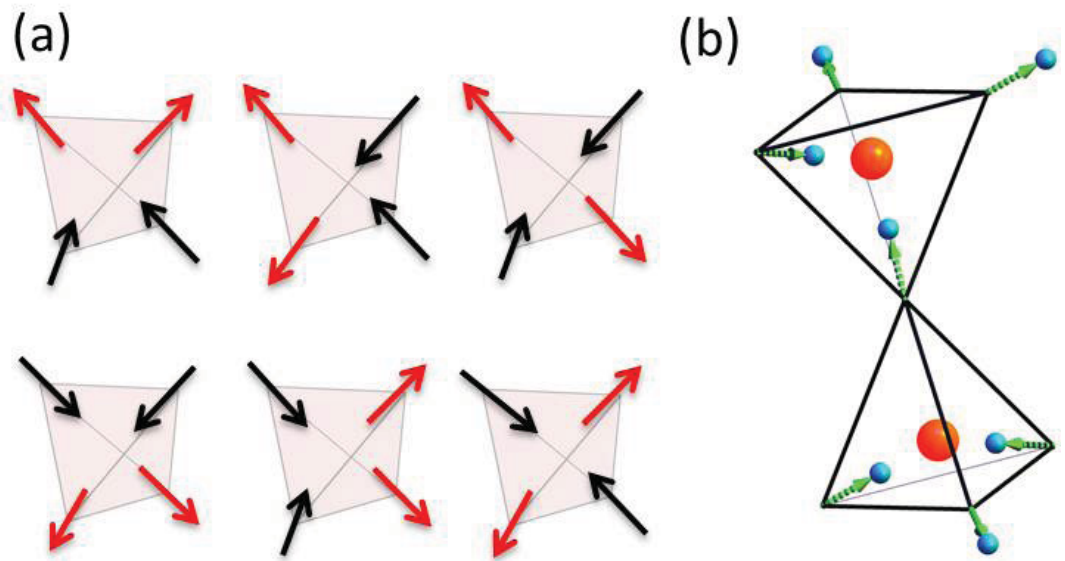


Figure 1.3: (a) 6 degenerate ground state configurations in one tetrahedron in spin ice. Red and black arrows correspond to “out” and “in” spins. Bottom 3 states are the time reversal partner of the top 3 states. (b) 2-in 2-out ice rule in cubic water ice: two protons (blue spheres) are closer to the central oxygen (red spheres) while the other two are further away.⁵

CHAPTER 1. INTRODUCTION

lattice geometry. On the extended pyrochlore lattice, the ground state degeneracy can be estimated in the following way: with N number of spins, there are 2^N total number of spin states. Since each spin is shared by 2 tetrahedra, the number of tetrahedra is $N/2$, each of which gives rise to a factor of $6/16$ due to the ice rule constraint. Thus the ground state degeneracy is $2^N(6/16)^{N/2} = (3/2)^{N/2}$.²⁴ Such macroscopic degeneracy gives rise to a residual zero point entropy that has been observed in water ice²⁵ as well as in materials that realize spin ice model.⁷

The spin correlations in the spin ice ground state, a classical spin liquid, illustrates the drastic difference between a spin liquid state and a high temperature paramagnetic state. By coarse graining the lattice variable σ_i into a spin field $\mathbf{P}(\mathbf{r})$ and noticing that the 2-in 2-out ice rule for σ_i is equivalent to a divergence-free condition for $\mathbf{P}(\mathbf{r})$: $\nabla \cdot \mathbf{P}(\mathbf{r}) = 0$, it can be shown that the two point spin correlation function in the spin ice ground state takes a dipolar form:²⁶

$$\langle \mathbf{P}_\mu(0) \mathbf{P}_\nu(\mathbf{r}) \rangle \sim \frac{1}{r^3} (\delta_{\mu\nu} - 3\hat{\mathbf{r}}_\mu \hat{\mathbf{r}}_\nu) \quad (1.4)$$

where $\hat{\mathbf{r}} \equiv \mathbf{r}/|\mathbf{r}|$. It is remarkable that the correlation function is algebraic which is often related to a critical point in a second order phase transition where the correlation length diverges.²⁷ By contrast, the spin correlations in the paramagnetic state take the form of an exponential decay $\langle \mathbf{P}(0) \mathbf{P}(\mathbf{r}) \rangle \sim \exp(-\frac{r}{\xi})$ with a finite correlation length ξ . This shows that although neither state has static order, the spin liquid is

CHAPTER 1. INTRODUCTION

in fact a highly correlated state.

More exotic are the elementary excitations from the spin ice ground state.²⁸ To see this consider each spin to be a pair of oppositely charged magnetic monopoles. This is in the same spirit that a electric dipole can be described in terms of a pair of positive and negative electric charges. Then the 2-in 2-out ground state constraint transforms into a charge neutral condition that each tetrahedron carries no net magnetic charge. Flipping a spin in the ground state cost a finite energy and creates net magnetic charges on the neighboring tetrahedra(Fig. 1.4(b)). This pair of magnetic monopoles, however, are not bonded together as in usual magnetic dipoles, since by flipping more spins they can be separated without any further energy cost(Fig. 1.4(c)). Thus these magnetic monopoles are deconfined and the elementary excitations in spin ice are individual monopoles. This is another example of fractionalized excitations that can be expected from a spin liquid.¹

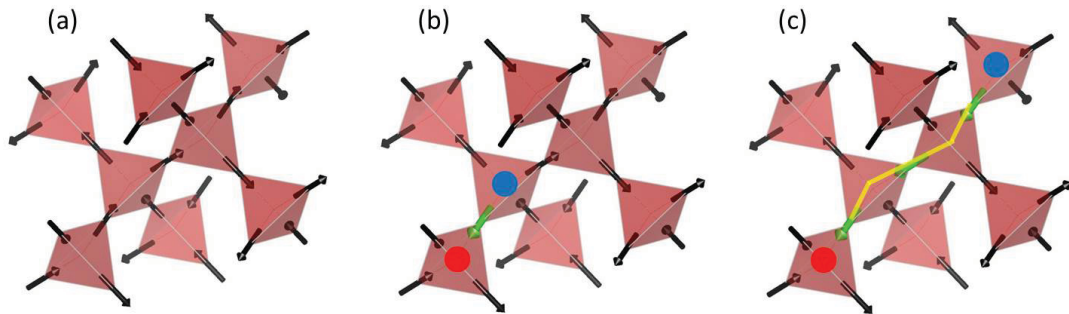


Figure 1.4: Deconfined magnetic monopoles in spin ice. (a) Spin ice ground state with ice rule satisfied in all tetrahedra. (b) Flipping one spin from the ground state creates net magnetic charges (magnetic monopoles) on neighboring tetrahedra. (c) These pair of monopoles can be separated without any further energy cost by subsequent spin flips.

CHAPTER 1. INTRODUCTION

The classical spin ice model demonstrates how a spin liquid state can arise due to geometrical frustration. It is actually a rare geometrically frustrated model whose ground state spin correlation and low energy excitations are well understood theoretically and have been experimentally observed in real materials.²³ Quantum spin models on frustrated lattices are generally less understood²² and experimental study of materials that host such models would not only give insight for a deeper theoretical understanding but also provide platforms for possible future applications that make use of the peculiar properties of spin liquids.

Tremendous progress has been made in the experimental search for spin liquids with several materials emerging as promising candidates.¹ Definitive evidence for a quantum spin liquid material however remains elusive. This is partly due to the fact that a spin liquid state is defined by what it is not: a ground state that does not break any symmetry¹ thus conclusive evidence requires a comprehensive experimental exclusion of any possible form of symmetry breaking. Another reason is that in real materials crystal defects come into play in various ways. For example $\text{ZnCu}_3(\text{OH})_6\text{Cl}_2$, a material that could host the spin- $\frac{1}{2}$ kagome Heisenberg model, has $\sim 15\%$ impurity spins between kagome layers²⁹ that could complicate experimental probing of low energy spin dynamics that is due to spins in the kagome layers. A recent experimental study of a pyrochlore lattice material $\text{Tb}_{2+x}\text{Ti}_{2-x}\text{O}_{7+y}$ showed that a minute change of stoichiometry with $x \sim 0.005$ can drive the material from a disordered to an ordered state.³⁰ This demonstrates that the properties of frustrated magnets can

CHAPTER 1. INTRODUCTION

be extremely sensitive to crystal defects so that potential model materials must be carefully characterized.

This thesis presents an experimental study of frustrated magnets that do not form conventional magnetic long range order. The aim is to investigate their magnetic ground state and the corresponding excitations under the influence of frustration, which arises from competing interaction and/or geometrical frustration, to explore how a spin liquid state could be realized in real materials and the roles played by perturbations to the model spin Hamiltonians. $\text{Pr}_2\text{Zr}_2\text{O}_7$, NiGa_2S_4 , and SrHo_2O_4 , whose magnetic lattices are the 3D pyrochlore lattice, the 2D triangular lattice, and the 1D zig-zig ladders respectively, were studied extensively through a combination of neutron scattering and bulk physical property characterizations. Each of these compounds forms an individual chapter in the thesis:

Chapter 2 describes the material synthesis and the experimental characterization of low temperature spin correlations for $\text{Pr}_2\text{Zr}_2\text{O}_7$. A strong correlation between physical properties and stoichiometry of $\text{Pr}_{2+x}\text{Zr}_{2-x}\text{O}_{7-x/2}$ was found and an optimal single crystal growth condition of stoichiometric $\text{Pr}_2\text{Zr}_2\text{O}_7$ was established. Despite apparent similarity to classical spin ice, $\text{Pr}_2\text{Zr}_2\text{O}_7$ was found to be dominated by quantum spin fluctuations at low temperature that originate from a combination of inter-spin interactions and peculiar single ion magnetic properties.

Chapter 3 focuses on the the low temperature magnetic excitation from the spin-1 triangular lattices in NiGa_2S_4 , where the spin correlation length remains anomalously

CHAPTER 1. INTRODUCTION

short down to temperatures much lower than the interaction energy scale. Our neutron scattering experiment shows an unconventional broad continuum of excitations that cannot be explained by conventional spin wave theory.

Chapter 4 presents an experimental realization of $J_1 - J_2$ Ising spin chains in SrHo_2O_4 . A “disorder by order” mechanism among these chains that ultimately prevents 3-dimensional long range order of the Ising spins was uncovered.

Most thermomagnetic measurements presented in this thesis were carried out on an in-house Quantum Design Physical Properties Measurement System equipped with a 14 T magnet and a dilution refrigerator. The neutron scattering experiments were performed at the NIST Center for Neutron Research and the Oak Ridge National Lab. A brief introduction of the neutron scattering technique and interpretation of the scattering data can be found in Appendix. A.

Although the search for quantum spin liquid remains open, this thesis highlights the various unexpected and interesting phenomena that occur near the spin liquid phase. This indicates that frustrated magnets will continue to be a fruitful research arena with great potential to expose novel forms of magnetism.

Chapter 2

Quantum Spin Ice $\text{Pr}_2\text{Zr}_2\text{O}_7$

2.1 Introduction

As was introduced in Chapter 1, classical Ising spins with ferromagnetic interactions on the pyrochlore lattice realize a spin analog of the disordered configuration of protons in cubic water ice, so called spin ice. The ground state of the model is a classical spin liquid that locally obeys the 2-in 2-out ice rule. This leads to dipolar spin-spin correlations and a macroscopic ground state degeneracy that results in residual entropy. The elementary excitations from spin ice can be described in terms of deconfined magnetic monopoles.²³

The classical spin ice model is realized in materials such as $\text{Ho}_2\text{Ti}_2\text{O}_7$ and $\text{Dy}_2\text{Ti}_2\text{O}_7$. Here due to crystalline electric field (CEF) effects,¹⁴ Ho^{3+} and Dy^{3+} have a magnetic doublet ground state with spins mainly along the local $\langle 111 \rangle$ directions of the tetrahe-

dra. The gap to the first excited CEF level is large ($\Delta \sim 300$ K), so at temperatures comparable or lower than the interaction energy scale (~ 1 K) the doublet can be regarded as a classical Ising spin. The ferromagnetic interactions, a key ingredient in the spin ice model, is provided by the dipole-dipole interactions between the large magnetic moments ($\sim 10 \mu_{\text{B}}$) of Ho^{3+} and Dy^{3+} .²³ The defining characteristics of spin ice including residual entropy, dipolar spin correlations, and magnetic monopole excitations have been observed experimentally in these materials.^{7,31,32}

In classical spin ice, spin dynamics is driven by thermal fluctuations or external magnetic fields and the motion of magnetic monopoles is diffusive. Also, since magnetic monopoles cost a finite energy determined by the exchange constant J , the system falls into a frozen state with negligible spin dynamics for $T \ll J$.

Spin ice becomes more interesting when dressed by quantum effects. By introducing quantum tunnelling processes between different ice states, the ground state can become a coherent superposition of the ice manifold with an emergent $U(1)$ gauge symmetry. This state is called a $U(1)$ quantum spin liquid.^{2,33} Correspondingly, fluctuations in the gauge fields generate gapless gauge bosons that are analogues to photons in conventional electromagnetism. The existence of these artificial photons can be indicated from features in the bulk measurements, such as saturation in DC magnetic susceptibility in the zero temperature limit and a large low temperature T^3 contribution to the heat capacity. The most direct indication however, would be through the dynamical structure factor which can be measured by inelastic neutron

scattering.³⁴

Quantum tunnelling among ice states can be enhanced by quantum mechanical exchange interactions.³⁵ A generic spin Hamiltonian on the pyrochlore lattice that captures the nearest neighbor exchange interactions between the Ising spins can be cast in the following form:⁶

$$\begin{aligned} \mathcal{H} = & - \sum_{\langle i,j \rangle} \{ J_{zz} S_i^z S_j^z - J_{\pm} (S_i^+ S_j^- + S_i^- S_j^+) + J_{\pm\pm} (\gamma_{ij} S_i^+ S_j^- + \gamma_{ij}^* S_i^- S_j^+) \} \\ & + J_{z\pm} [S_i^z (\zeta_{ij} S_j^+ + \zeta_{ij}^* S_j^-) + (\zeta_{ij} S_i^+ + \zeta_{ij}^* S_i^-) S_j^z]. \end{aligned} \quad (2.1)$$

Here S_i is a pseudo spin- $\frac{1}{2}$ operator that represents the Ising doublet. γ, ζ are phase factors that depend on the bond direction between S_i, S_j . In classical spin ice, the only non-zero interaction is J_{zz} that is provided by combination of crystal field and dipolar interactions. The additional transverse terms that arise from exchange interactions induce quantum dynamics within the ice manifold. Theoretical calculations show that around the classical spin ice a $U(1)$ quantum spin liquid phase exists in an extended parameter space (Fig. 2.1)⁶

The first step towards an experimental study of quantum spin ice is to identify pyrochlore materials with dominant exchange interactions. In $\text{Ho}_2\text{Ti}_2\text{O}_7$ and $\text{Dy}_2\text{Ti}_2\text{O}_7$ exchange interactions are much smaller than dipolar interaction as a result of large magnetic moment size of Ho^{3+} and Dy^{3+} . One way to overcome this is to use rare earth elements with much smaller moment sizes, such as Pr and Yb. Strong low

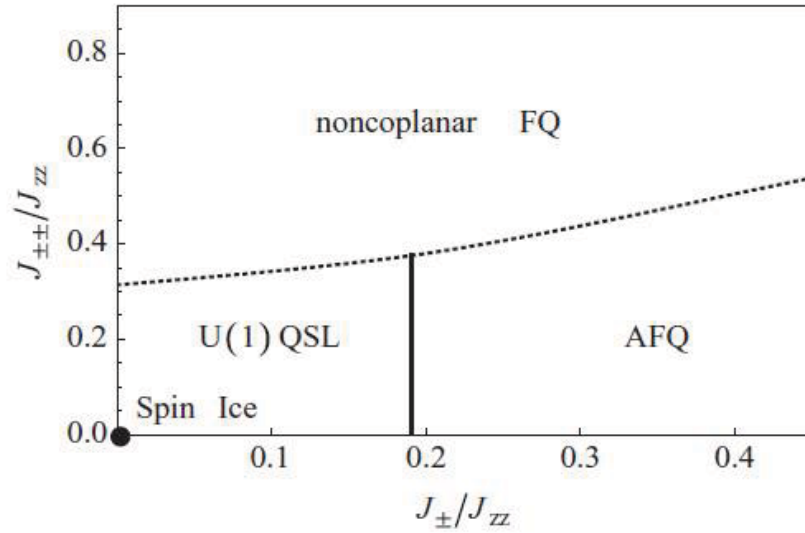


Figure 2.1: $U(1)$ quantum spin liquid exist in an extended parameter space around the classical spin ice.⁶

temperature spin fluctuations have been observed in $\text{Pr}_2\text{Sn}_2\text{O}_7$ ³⁶ and $\text{Yb}_2\text{Ti}_2\text{O}_7$,^{37,38} making them promising candidates.

Another Pr based candidate compound $\text{Pr}_2\text{Zr}_2\text{O}_7$ is studied comprehensively in this thesis.^{4,5} As has been seen in materials such as $\text{Tb}_2\text{Ti}_2\text{O}_7$ ³⁰ and $\text{Yb}_2\text{Ti}_2\text{O}_7$,³⁹ there can be strong correlations between physical properties and minute changes in stoichiometry, so to obtain meaningful results it is crucial to systematically establish this correlation and optimize the synthesis condition for $\text{Pr}_2\text{Zr}_2\text{O}_7$. In the following sections, I will first present the detail synthesis work that forms the foundation for the study of the physical characteristics of this materials in the later sections.

2.2 $\text{Pr}_2\text{Zr}_2\text{O}_7$ Sample Synthesis

$\text{Pr}_2\text{Zr}_2\text{O}_7$ crystallizes in space group $Fd\bar{3}m$ (Fig. 2.2). It is informative to write the chemical formula as $\text{Pr}_2\text{Zr}_2\text{O}_6\text{O}'$, which highlights the fact that there are two types of oxygen positions: O at $48f$ ($x, 1/8, 1/8$) and O' at $8b$ ($3/8, 3/8, 3/8$). Pr and Zr respectively occupy the $16d$ ($1/2, 1/2, 1/2$) and $16c$ ($0, 0, 0$) positions, and the pyrochlore structure is defined by just two parameters: the lattice constant and the positional parameter x for O. For rare earth zirconates with general formula $\text{Ln}_2\text{Zr}_2\text{O}_7$, it has been shown the pyrochlore structure is favored when the lanthanoid radius is larger than Gd, while smaller lanthanoids lead to a defect fluorite structure (space group $Fm\bar{3}m$) where Ln and Zr are disordered and O' is randomly distributed between $8b$ and $8a$ ($1/8, 1/8, 1/8$) sites.⁴⁰ Pr has a radius larger than Gd and thus is expected to form the pyrochlore structure, however site mixing between Pr and Zr and disorder in oxygen might still occur locally during synthesis requiring careful post-synthesis characterization. What is more, Pr was found to evaporate during floating zone synthesis of single crystal $\text{Pr}_2\text{Zr}_2\text{O}_7$,⁴¹ so the stoichiometry of floating zone grown $\text{Pr}_2\text{Zr}_2\text{O}_7$ is a key factor that needs to be monitored and optimized. To this end, we systematically synthesized and characterized polycrystalline $\text{Pr}_{2+x}\text{Zr}_{2-x}\text{O}_{7-x/2}$ with $-0.02 \leq x \leq 0.02$.

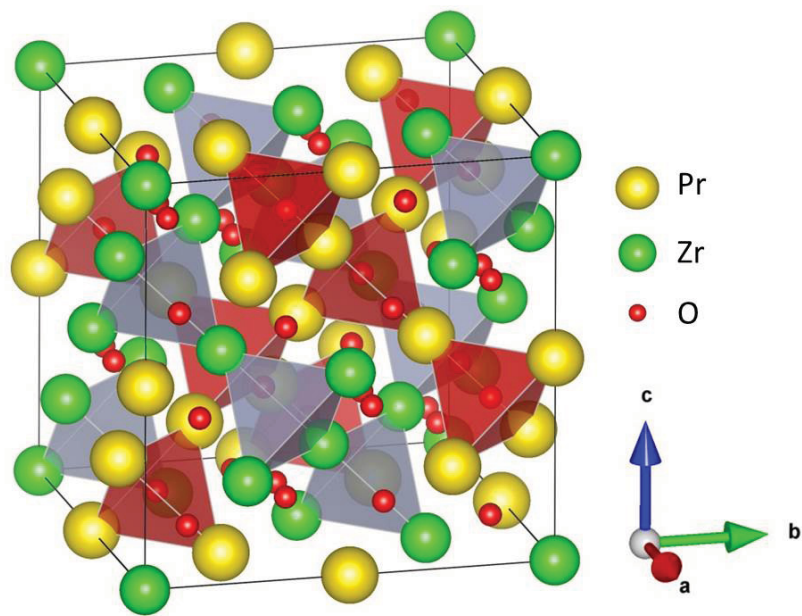
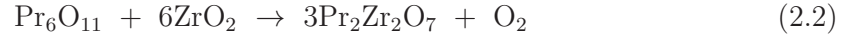


Figure 2.2: Crystal structure of $\text{Pr}_2\text{Zr}_2\text{O}_7$. Yellow, green, and red spheres represent Pr, Zr, and O atoms respectively. Pr and Zr each form interpenetrating pyrochlore lattices.

2.2.1 Polycrystalline $\text{Pr}_{2+x}\text{Zr}_{2-x}\text{O}_{7-x/2}$

Polycrystalline $\text{Pr}_{2+x}\text{Zr}_{2-x}\text{O}_{7-x/2}$ was prepared by heating the starting materials Pr_6O_{11} and ZrO_2 at temperatures of 1250°C , 1500°C , and 1550°C in air for 8 hr respectively with intermediate grinding:



x in $\text{Pr}_{2+x}\text{Zr}_{2-x}\text{O}_{7-x/2}$ was controlled by the corresponding Pr/Zr ratio in the starting materials. The powder was then sealed in a rubber tube, evacuated, and compacted into a rod (typically 5 mm in diameter and 80 mm long) using a hydraulic press under an isostatic pressure of 70 MPa. After removal from the rubber tube, the rods were sintered again at 1550°C for 10 hr in air. These sintered rods typically have a light brownish color (Fig. 2.3(a)). It is known that the color of Pr ions changes from dark black to green as its oxidation state changes from Pr^{4+} to Pr^{3+} .⁴² Thus the brownish color is an indication of extra oxygen inclusion that cause some Pr^{3+} , the expected oxidation state of Pr in $\text{Pr}_2\text{Zr}_2\text{O}_7$, to be converted to Pr^{4+} . This is not surprising since the sintering is carried out in air. Zr ions generally have oxidation state of Zr^{4+} unless under extreme condition, so the Zr oxidation state is not considered a variable in this material. To obtain the proper oxygen content, the rods were sintered once more in a four-mirror optical floating zone furnace (Crystal Systems Inc. FZ-T-4000-

CHAPTER 2. QUANTUM SPIN ICE $\text{Pr}_2\text{Zr}_2\text{O}_7$

H-VII-VPO-PC with 4×1 kW halogen lamps) using 80% of the lamp power in a 1 bar static high purity Argon atmosphere. After this extra sintering process, the color of the rods turned green, the expected color for Pr^{3+} (Fig. 2.3(b)).

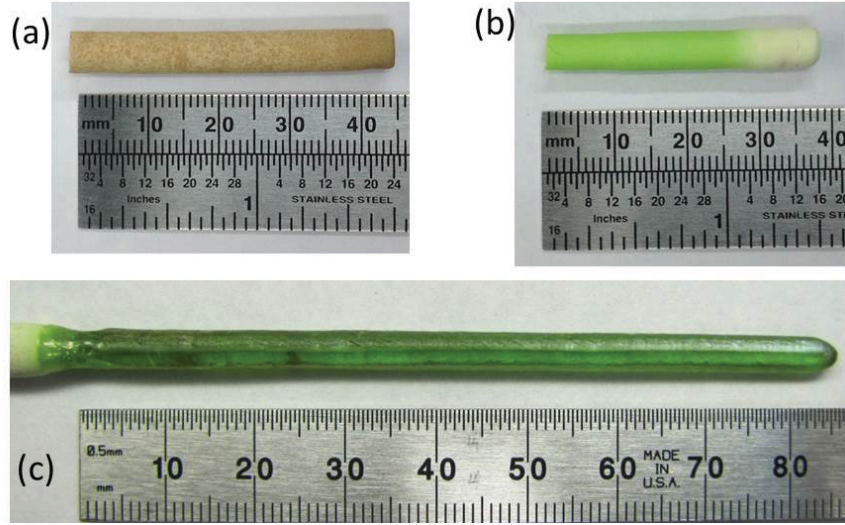


Figure 2.3: Polycrystalline $\text{Pr}_2\text{Zr}_2\text{O}_7$ before (frame (a)) and after (frame (b)) sintering in Argon atmosphere. (c) A representative $\text{Pr}_2\text{Zr}_2\text{O}_7$ single crystal grown under 1 bar static high-purity argon atmosphere using an optical floating zone image furnace.⁴

The first salient feature that changes systematically with x is the lattice parameter. This was probed by room temperature powder X-ray diffraction using an in-house Bruker D8 Focus X-ray diffractometer. Silicon was used as an internal normalization standard for lattice constant. The result is shown in Fig. 2.4, which reveals a quasi-linear relation between lattice constant and x , and that stoichiometric $\text{Pr}_2\text{Zr}_2\text{O}_7$ has a lattice constant of $a = 10.70254(4)$ Å.

In addition to the lattice parameter, bulk properties of $\text{Pr}_{2+x}\text{Zr}_{2-x}\text{O}_{7-x/2}$ including magnetic susceptibility and heat capacity show systematic correlation with x

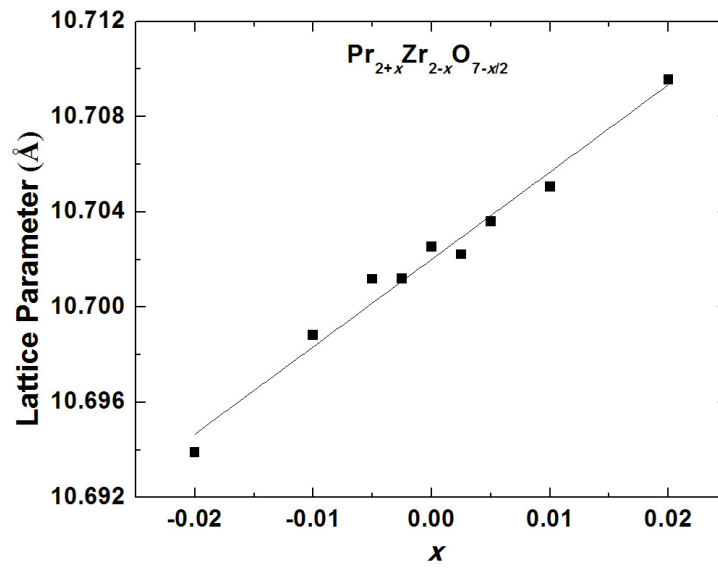


Figure 2.4: Lattice parameters of polycrystalline $\text{Pr}_{2+x}\text{Zr}_{2-x}\text{O}_{7-x/2}$ at different x shows an increase in lattice parameter as the Pr/Zr ratio increases. The solid line is a linear fit through the data points, which corresponds to $da/dx = 0.37 \text{ \AA}$.⁴

CHAPTER 2. QUANTUM SPIN ICE $\text{Pr}_2\text{Zr}_2\text{O}_7$

(Fig. 2.5). Temperature-dependent magnetization was measured under magnetic fields of $H = 0.1$ T between $T = 2$ and 150 K and 0.5 T for $T \geq 150$ K after zero field cooling. The temperature dependent heat capacity was measured above $T = 2$ K using the semiadiabatic relaxation technique. Both were measured using a Quantum Design Physical Property Measurement System (PPMS).

The inverse magnetic susceptibility (Fig. 2.5(a)) shows a systematic shift with x . To quantify the change, Curie-Weiss fittings were carried out for data points with $2 \text{ K} \leq T \leq 20 \text{ K}$. The upper limit in temperature was chosen to reduce influences from higher CEF levels (Fig. 2.6). The fitting results reveal both the Weiss temperature and the effective moment size increase with x . It is worth noting that the Weiss temperature changes by a factor of 5 for a minute change of x from -0.02 to 0.02 , illustrating the extreme sensitivity of the physical properties of $\text{Pr}_{2+x}\text{Zr}_{2-x}\text{O}_{7-x/2}$ to stoichiometry. The specific heat also changes monotonically with x , for example, C_P at $T \sim 10$ K changes by a factor of 2 over the range of x probed in this study.

These large changes in physical properties could indicate changes in crystal structure with x . To look for changes in the average crystal structure of $\text{Pr}_{2+x}\text{Zr}_{2-x}\text{O}_{7-x/2}$, high resolution synchrotron X-ray diffraction measurements were carried out on 11-BM at the Advanced Photon Source of Argonne National Laboratory. Surprisingly, the Rietveld refinements (Fig. 2.7, Table. 2.1) show that all samples retain the ideal pyrochlore structure, and apart from the expected inclusion of extra Pr on Zr sites for positive x and extra Zr on Pr sites for negative x , there is no additional site mixing

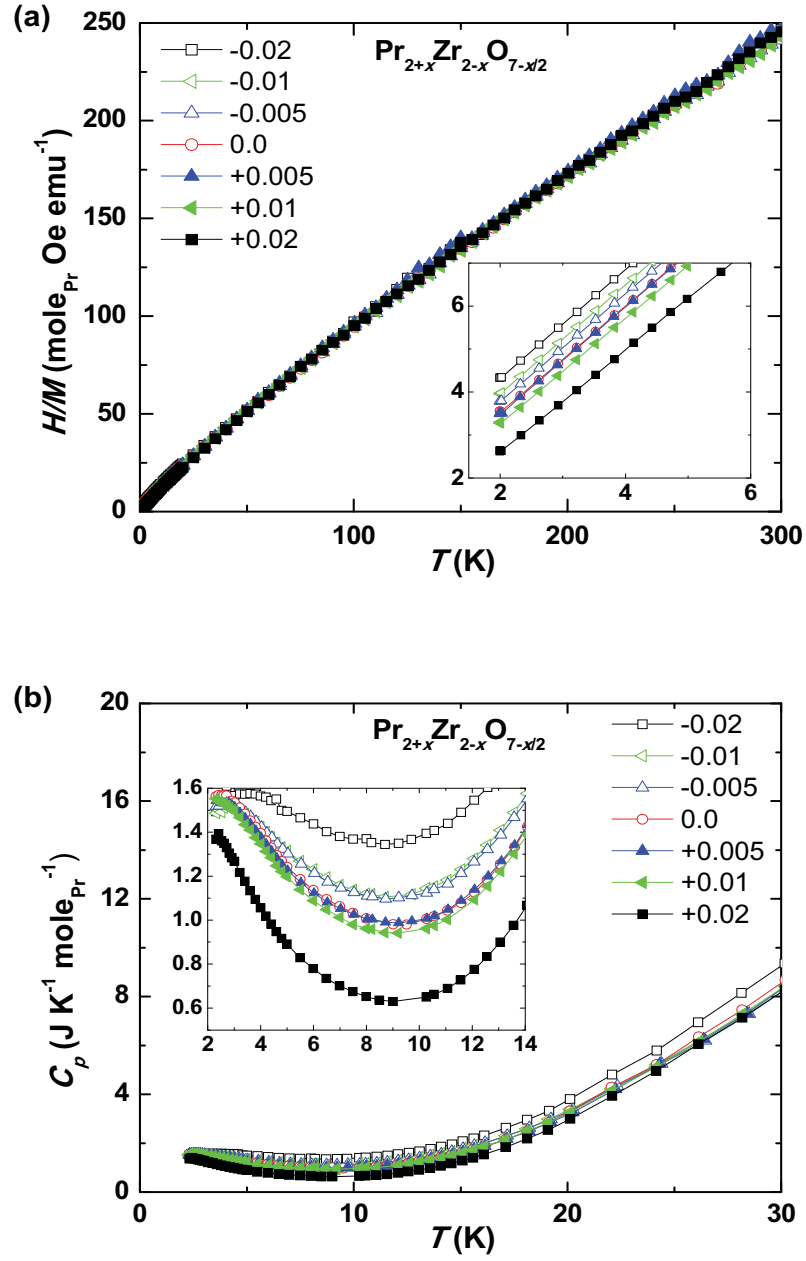


Figure 2.5: T – dependence of inverse magnetic susceptibility (a) and specific heat (b) of polycrystalline $\text{Pr}_{2+x}\text{Zr}_{2-x}\text{O}_{7-x/2}$ samples. Insets zoom in at low temperatures and demonstrate systematic changes in bulk properties as x varies.⁴

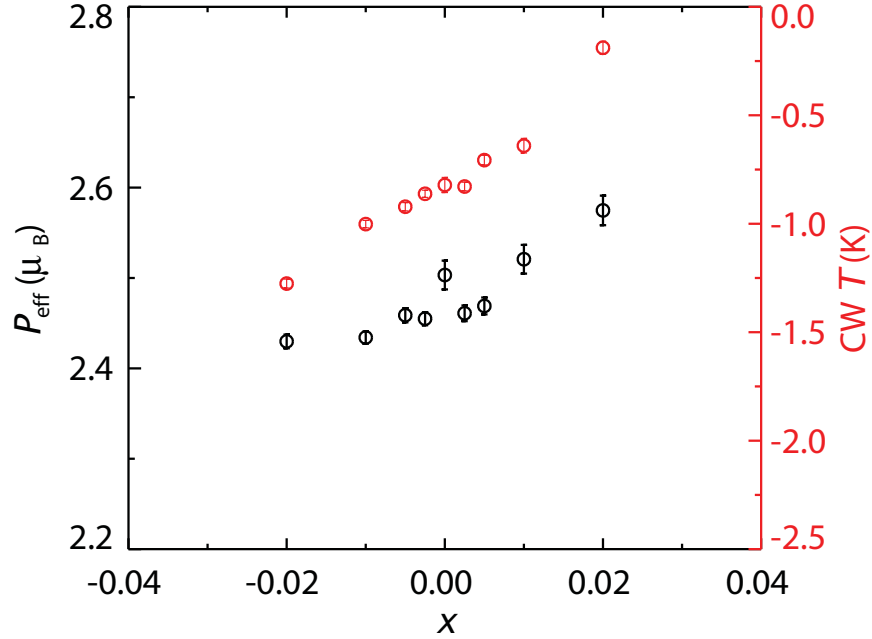


Figure 2.6: Curie-Weiss fitting results of magnetic susceptibility show changes of effective moment size P_{eff} and Curie-Weiss temperature $\text{CW } T$ as a function of x .

between Pr/Zr. Further test of possible oxygen vacancies on $48f$ and $8b$ sites or oxygen inclusion on the vacant $8a$ site showed no statistically significant improvement in fitting.

The change of Pr/Zr ratio in the range studied here thus does not seem to have a significant effect on the average crystal structure of $\text{Pr}_{2+x}\text{Zr}_{2-x}\text{O}_{7-x/2}$, thus the question arises as why the physical properties vary so drastically with x . A possible scenario comes from the observation that the X-ray data is best fit with anisotropic thermal parameters for Pr and the thermal ellipsoid of Pr takes a pancake-like shape with the short axis along the local $\langle 111 \rangle$ directions. This is reminiscent of the situation in $\text{Bi}_2\text{Ti}_2\text{O}_7$ and $\text{Bi}_2\text{Ru}_2\text{O}_7$ where the pancake-like thermal ellipsoid was found

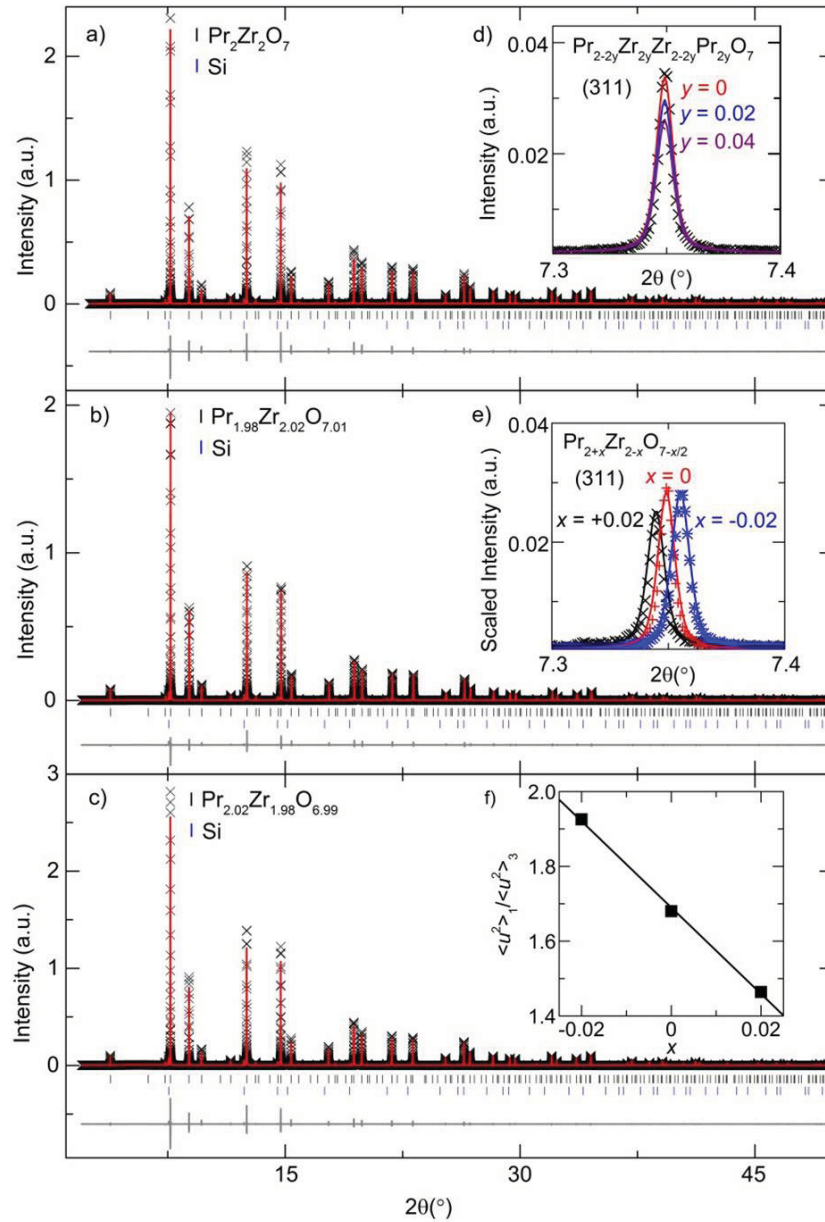


Figure 2.7: Rietveld refinement of synchrotron X-ray data of $\text{Pr}_{2+x}\text{Zr}_{2-x}\text{O}_{7-x/2}$ for (a) $x = 0$, (b) $x = 0.02$, and (c) $x = +0.02$. (d) As an example of measurement sensitivity to Pr/Zr site mixing, the change in model intensity for the (311) pyrochlore-only reflection for various mixing ratios is compared to the observed data for $x = 0$. (e) The changes in the (311) pyrochlore reflection with composition is accurately modeled by the changes in Pr/Zr ratio, without any additional Pr/Zr mixing. (f) The ratio of mean square displacements ($\langle u_1^2 \rangle / \langle u_3^2 \rangle$) of Pr versus x , with a guide to the eye.⁴

Table 2.1: Rietveld refinements results for $\text{Pr}_{2+x}\text{Zr}_{2-x}\text{O}_{7-x/2}$.⁴

Parameter	$\text{Pr}_{2.02}\text{Zr}_{1.98}\text{O}_{6.99}$	$\text{Pr}_2\text{Zr}_2\text{O}_7$	$\text{Pr}_{1.98}\text{Zr}_{2.02}\text{O}_{7.01}$
a (Å)	10.710322(3)	10.703798(3)	10.694711(3)
Cell Volume	1228.5918(6)	1226.3480(6)	1223.2272(6)
Pr			
occ*(Pr/Zr)	1.0/0	1.0/0	0.99/0.01
U_{eq} (Å ²)	0.0083	0.0078	0.0084
$U_{11} = U_{22} = U_{33}$ (Å ²)	0.00825(3)	0.00776(3)	0.00844(2)
$U_{12} = U_{23} = U_{13}$ (Å ²)	-0.00109(10)	-0.00121(9)	-0.00161(7)
Zr			
occ*(Pr/Zr)	0.99/0.01	1.0/0	1.0/0
U_{eq} (Å ²)	0.0044	0.0043	0.0054
$U_{11} = U_{22} = U_{33}$ (Å ²)	0.00440(4)	0.00428(4)	0.00559(3)
$U_{12} = U_{23} = U_{13}$ (Å ²)	0.00003(14)	0.00043(13)	0.00077(10)
x	0.33368(15)	0.33391(15)	0.33428(10)
O			
occ*	1.0	1.0	1.0
U_{iso} (Å ²)	0.0076(4)	0.0080(4)	0.0081(3)
O'			
occ*	1.0	1.0	1.0
U_{iso} (Å ²)	0.0113(10)	0.0085(9)	0.0069(6)
χ^2	4.071	6.802	3.285
R_{wp} (%)	12.08	12.01	8.69
R_{p} (%)	9.83	9.68	7.31
R_{F}^2 (%)	4.96	5.15	3.47

*occupancies were fixed at nominal values.

to be a result of incoherent Bi^{3+} off-centering due to the lone pair effect.⁴³ If Pr off-centering indeed occurs in $\text{Pr}_{2+x}\text{Zr}_{2-x}\text{O}_{7-x/2}$, one could expect the single ion magnetic properties of Pr^{3+} to be strongly correlated with the extent of off-centering through CEF effects and this would dramatically change the low temperature magnetic properties of $\text{Pr}_{2+x}\text{Zr}_{2-x}\text{O}_{7-x/2}$. In support of this, it is found that the ratio of the long axis to the short axis of the thermal ellipsoid ($\langle u_1^2 \rangle / \langle u_3^2 \rangle$), which quantifies the distortion, changes monotonically with x as shown in Fig. 2.7(f). The observation that the distortion is not minimal at the stoichiometric point suggests intrinsic Pr off-centering in $\text{Pr}_2\text{Zr}_2\text{O}_7$ that warrants further investigation.

2.2.2 Single Crystal Synthesis of $\text{Pr}_2\text{Zr}_2\text{O}_7$

Having established a phenomenological correlation between the stoichiometry of $\text{Pr}_2\text{Zr}_2\text{O}_7$ and physical properties including lattice parameter, magnetic susceptibility, and specific heat, we are in a position to pursue synthesis of high quality stoichiometric $\text{Pr}_2\text{Zr}_2\text{O}_7$ single crystals.

Growth atmosphere and pressure, rotation rate, and growth rate are three key parameters in floating zone synthesis of single crystals.⁴⁴ Oxygen atmosphere was found to enhance Pr evaporation during growth and the resultant crystals have black color due to partial conversion of Pr^{3+} to Pr^{4+} . Thus static 1 bar of high purity Argon atmosphere was instead used and the crystals grown under such condition have the correct green color (Fig. 2.3(c)).

CHAPTER 2. QUANTUM SPIN ICE $\text{Pr}_2\text{Zr}_2\text{O}_7$

To study the effect of rotation rate, floating zone growth of $\text{Pr}_2\text{Zr}_2\text{O}_7$ was carried out at fixed growth rate of 4 mm/hr at different rotation rates of 0, 3, 6, and 12 rpm. Back-scattered scanning electron microscope (SEM) was used to study the microstructure of such grown crystals, as shown in Fig. 2.8. For the crystal grown at 0 rpm (Fig. 2.8(a)), there is an indication of spinodal decomposition where two kinds of micro-size domains were formed. These can be qualitatively described as Pr-rich phase (white region) and Zr-rich phase (dark region) since heavier Pr backscatters more strongly than Zr. Application of rotation reduces the domain formation and produces significantly more uniform microstructure, as shown in Fig. 2.8(b,c,d). A more careful look at the microstructure near the surface of the crystals shows cumulation of Pr-rich phase at the surface for fast rotation of 12 rpm, thus a rotation rate between 3 rpm to 6 rpm is considered optimal.

Growth rate is another important parameter that needs optimization. In this case, growth at rates from 1 mm/hr to 20 mm/hr were carried out. It was found that the lattice parameter of the grown crystals increase monotonically as the growth rate increases and saturates near that of stoichiometric polycrystalline $\text{Pr}_2\text{Zr}_2\text{O}_7$ (Fig. 2.9). This is consistent with the fact that Pr evaporates during growth so that slower growth leads to more Pr deficiency, which results in a smaller Pr/Zr ratio and a smaller lattice parameter as established in the powder study (Fig. 2.4). Correspondingly the growth rate dependent physical properties (Fig. 2.10) follow the same trend as in the powder study where the Pr/Zr ratio was tuned (Fig. 2.5). Crystals grown at high growth

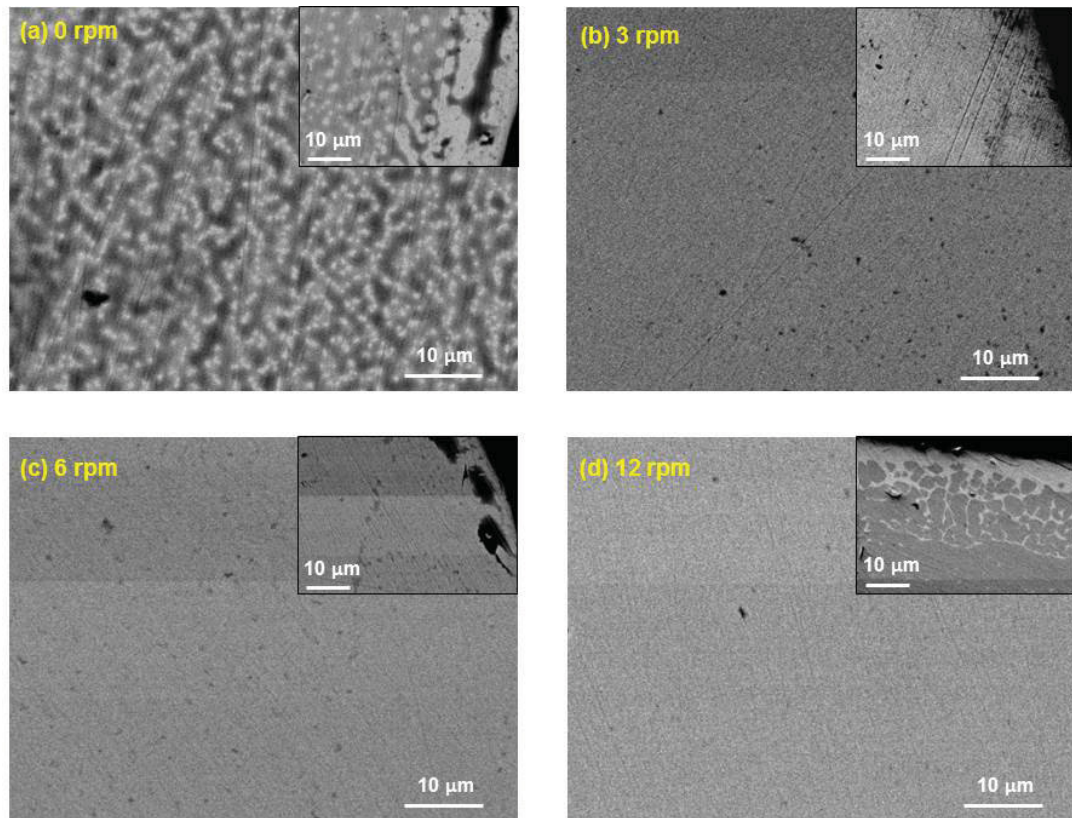


Figure 2.8: SEM back scattered micrographs of cross sections from the center (large pictures) and surface (smaller pictures on the top right) of $\text{Pr}_2\text{Zr}_2\text{O}_7$ single crystals grown at (a) 0 rpm, (b) 3 rpm, (c) 6 rpm and (d) 12 rpm. A spinodal decomposition is shown for the growth at 0 rpm, while application of the rotation of 3, 6 and 12 rpm produces a more uniform internal microstructure, with the highest rotation rates driving excess Pr to the edges producing inhomogeneity at the surface.⁴

CHAPTER 2. QUANTUM SPIN ICE $\text{Pr}_2\text{Zr}_2\text{O}_7$

rate, however, tend to develop cracks during growth due to more rapid temperature change, thus an intermediate growth rate of 10 mm/hr was chosen to grow crack-free crystals. In order to compensate for Pr loss during growth, an extra 1% Pr was introduced in the starting feed rods.

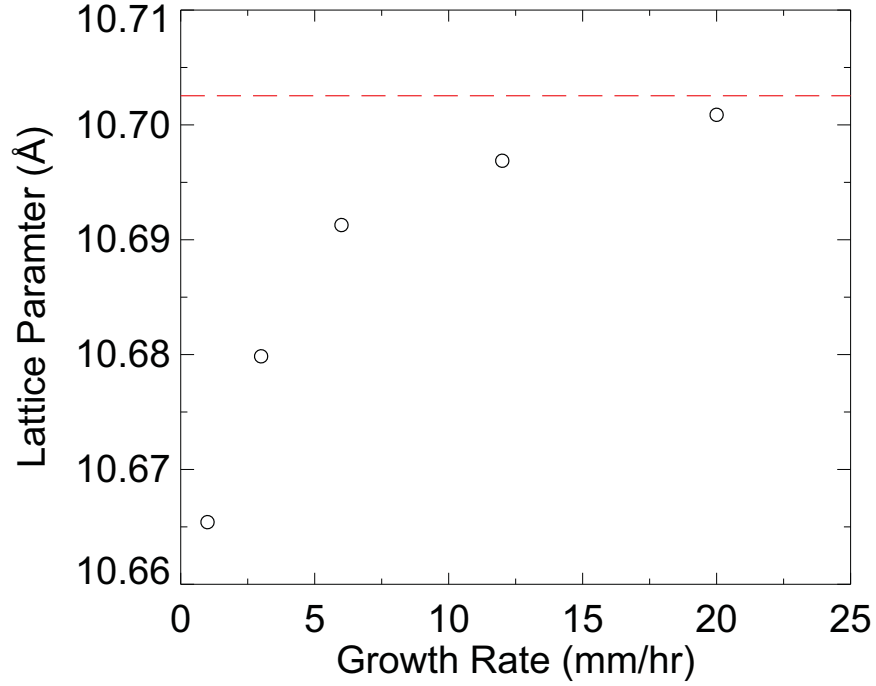


Figure 2.9: Lattice parameter of $\text{Pr}_2\text{Zr}_2\text{O}_7$ single crystals grown at different growth rates. Red dashed line shows the lattice parameter of stoichiometric polycrystalline $\text{Pr}_2\text{Zr}_2\text{O}_7$.

Thus the optimal floating zone growth condition for $\text{Pr}_2\text{Zr}_2\text{O}_7$ was established as:

- Prepare starting feed rods with $\sim 1\%$ extra Pr.
- Use growth rate of 10 mm/hr in combination with rotation rate of 6 rpm.
- Use 1 bar of static high purity Argon gas during growth.

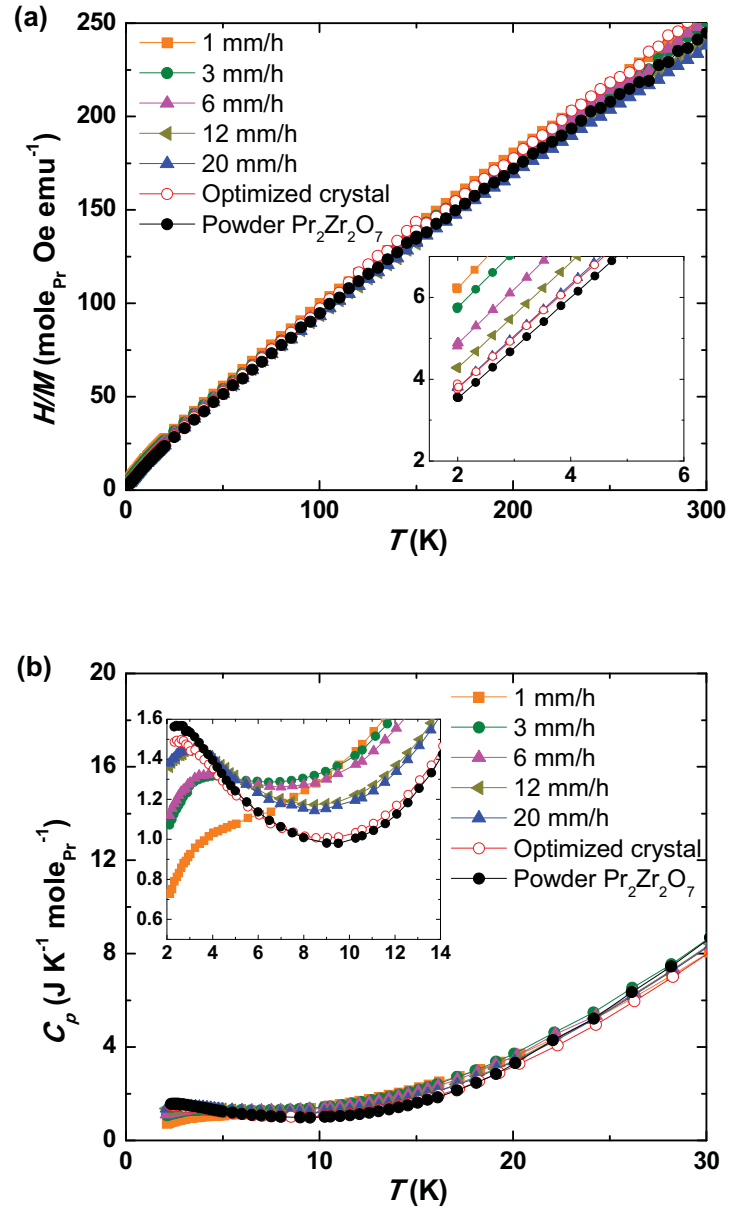


Figure 2.10: Temperature dependence of inverse magnetic susceptibility (a) and specific heat (b) of single crystalline samples grown at different growth rates. Insets show closer look at low temperatures. A crystal grown under optimized conditions exhibits the same physical properties as the stoichiometric powder sample, demonstrating its high quality.⁴

A typical crystal grown under such optimal condition has a lattice parameter of $10.70227(5)$ Å, indistinguishable from the stoichiometric powder sample. And its magnetic susceptibility and heat capacity also show close resemblance to that of the stoichiometric powder (Fig. 2.10), which further confirms the high quality of the crystal.

2.3 Spin Ice with Quantum Fluctuation

The successful synthesis of high quality single crystal $\text{Pr}_2\text{Zr}_2\text{O}_7$ lays the foundation for a detailed study of low temperature correlated magnetism of this material, which will be described in the following two sections.

2.3.1 Crystalline Electric Field Level Scheme

The single ion magnetic properties of Pr^{3+} are the starting point for understanding the low temperature magnetism of $\text{Pr}_2\text{Zr}_2\text{O}_7$. Bulk magnetization measurements along high symmetry axes revealed anisotropic magnetic moments that have easy axes along local $\langle 111 \rangle$ direction,⁴⁵ as in the classical spin ice materials $\text{Ho}_2\text{Ti}_2\text{O}_7$ and $\text{Dy}_2\text{Ti}_2\text{O}_7$. For a direct probe of the CEF level scheme and wavefunctions we turn to inelastic neutron scattering.

The experiment was performed on the ARCS spectrometer at SNS, ORNL⁴⁶ on single crystalline $\text{Pr}_2\text{Zr}_2\text{O}_7$. Measurements were conducted at 7.8 K and 150 K with

fixed incident neutron energies of 40 meV and 120 meV. For momentum space averaging, the sample was rotated back and forth around the vertical $[111]$ direction during the measurements. CEF analysis focused on the data collected at 7.8 K.

CEF transitions being local excitations show up as flat modes in the Energy-Momentum ($E - Q$) intensity maps. From the experimental data, 5 CEF transitions were identified, as shown in Fig. 2.11. These are at energy transfers near 9.5 meV, 57.1 meV, 81.9 meV, 93.2 meV, and 108.7 meV. Two extra flat levels at around 66.5 meV and 71.7 meV were identified as vibrational excitations because the inelastic scattering intensity was found to grow with increasing $|Q|$ while the intensity of magnetic excitations should decrease with $|Q|$ due to the magnetic form factor.⁴⁷

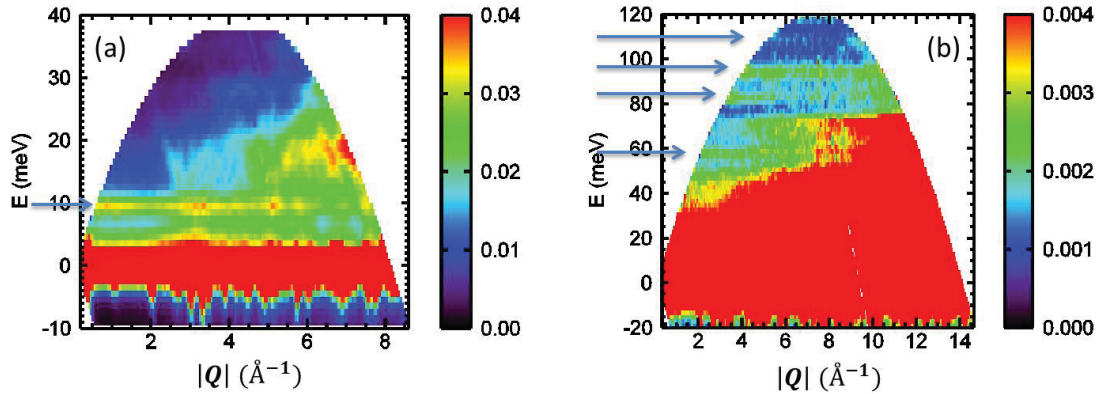


Figure 2.11: $E - Q$ slices measured on $\text{Pr}_2\text{Zr}_2\text{O}_7$ at 7.8 K with incident neutron energy of 40 meV(a) and 120 meV(b). Blue arrows indicate the flat modes that are inferred to be CEF transitions.

The two data sets with E_i of 40 meV and 120 meV were combined by matching energy integrated incoherent nuclear scattering intensities. To reduce the effects from phonon scattering, only data with scattering angles less than 24° for $E_i = 40$ meV and

CHAPTER 2. QUANTUM SPIN ICE $\text{Pr}_2\text{Zr}_2\text{O}_7$

less than 30° for $E_i = 120$ meV were used. The spectra are shown in Fig. 2.12. CEF peak positions and intensities were extracted by fitting the data to Gaussians with polynomial backgrounds: the peak around 9.5 meV was fitted with one Gaussian and a second order polynomial background. The peaks between 50 meV and 120 meV were fitted with six Gaussians and a third order polynomial. The full width at half maximum (FWHM) for peaks near 57.1 meV, 81.9 meV, 93.2 meV, and 108.7 meV were constrained to follow $\text{FWHM}(E) = \sqrt{(2\hbar\gamma)^2 + \text{FWHM}_C(E)^2}$, where $\text{FWHM}_C(E)$ is the calculated FWHM for ARCS at energy transfer E . The best fit value of $\hbar\gamma$ was 2.2 ± 0.1 meV and can be associated with a level independent bandwidth resulting from dispersion, a magneto-elastic decay rate, or a static disorder distribution. The CEF peak positions and energy integrated intensities thus obtained were subsequently used in the least squares fitting procedure described below.

The CEF Hamiltonian for Pr^{3+} in D_{3d} symmetry in $\text{Pr}_2\text{Zr}_2\text{O}_7$ takes the form of⁴⁸

$$\mathcal{H}_{\text{CEF}} = B_2^0 O_2^0 + B_4^0 O_4^0 + B_4^3 O_4^3 + B_6^0 O_6^0 + B_6^3 O_6^3 + B_6^6 O_6^6. \quad (2.3)$$

Here O_n^m are Stevens Operator Equivalents.⁴⁹ CEF levels and eigenvectors were obtained through numerical diagonalization, and the transition matrix elements between eigenvector $|i\rangle$ and $|j\rangle$ were calculated using $T_{ij} = \sum_\alpha |\langle i | J^\alpha | j \rangle|^2$, where J^α is the total angular momentum operator and $\alpha = x, y, z$. A simultaneous fit of the neutron spectrum as represented by the peak positions and integrated intensities and the tem-

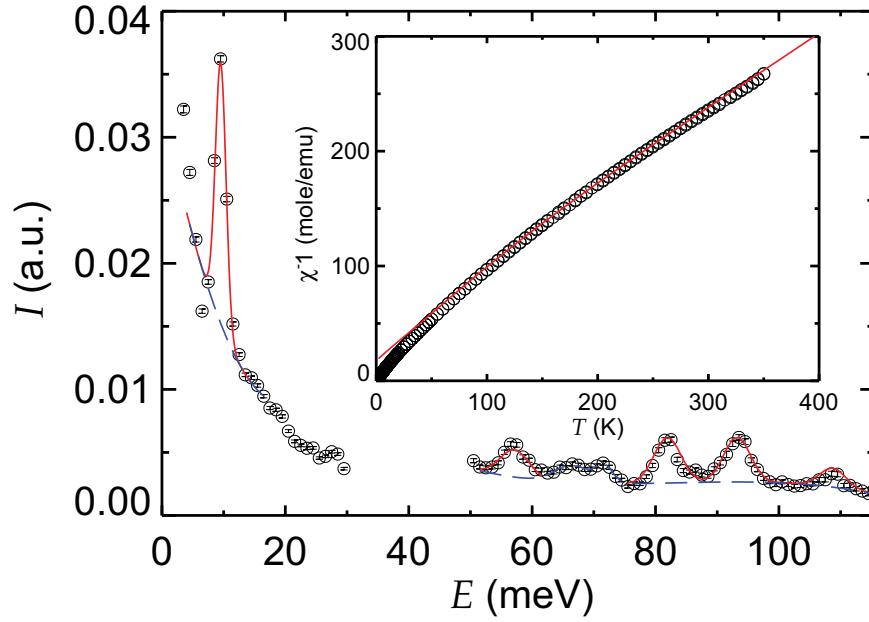


Figure 2.12: Combined neutron spectrum obtained with two different incident beam energies, $E_i = 40$ meV and 120 meV at $T = 7.8$ K. The blue dashed line denotes fitted backgrounds. The red solid line is the calculated best fit. Inset: Temperature dependence of the inverse magnetic susceptibility. The red solid line in the inset is the calculated best fit based on the same crystal field parameters (Table. 2.2 and Table. 2.3) as used to describe the inelastic neutron scattering data.⁵

perature dependent magnetic susceptibility ($50 \text{ K} \leq T \leq 350 \text{ K}$, $\mathbf{H} \parallel (111)$) was used to determine the CEF parameters B_n^m . The magnetic susceptibility was assumed to take the form of $\chi = \chi_0/(1 + \lambda\chi_0)$, where χ_0 is the single ion susceptibility calculated using the Van Vleck formalism:⁵⁰

$$\chi_0 = \sum_{i,j,E_i=E_j} \frac{|\langle i|\mathbf{m} \cdot \mathbf{e}_H|j\rangle|^2}{k_B T} \rho_i + \sum_{i,j,E_i \neq E_j} \frac{|\langle i|\mathbf{m} \cdot \mathbf{e}_H|j\rangle|^2}{E_j - E_i} (\rho_i - \rho_j). \quad (2.4)$$

Here \mathbf{m} is the magnetic moment operator, \mathbf{e}_H is the direction of the applied field, $\rho_i = e^{-\beta E_i}/Z$ with Z the partition function, and i, j run over all the crystal field eigenstates. χ_0 was averaged over four inequivalent Pr^{3+} sites. The best fit interaction parameter, λ was found to be 14.6 ± 0.3 mole-Pr/emu. The CEF level scheme and transition matrix elements were then used to fit the experimental intensity data, allowing an overall intensity scale and the FWHM for each peak to vary. The corresponding fitting result is shown in Fig. 2.12. A summary of the CEF scheme thus obtained is shown in Table. 2.2 and Table. 2.3.

Table 2.2: Experimental CEF parameters for $\text{Pr}_2\text{Zr}_2\text{O}_7$ in meV.⁵

B_0^2	B_0^4	B_3^4	B_0^6	B_3^6	B_6^6
-0.928	-0.0362	0.295	0.000664	-0.00228	0.00435

It was found that the CEF ground state is a magnetic doublet that is separated from the first excited state by ~ 9 meV. Thus at low temperatures ($k_B T \ll 9$ meV) only the ground state doublet need be considered. The ground state doublet wavefunctions mainly consist of $|\pm 4\rangle$ states, giving rise to the strong $\langle 111 \rangle$ anisotropy

Table 2.3: CEF spectrum and wave functions for $\text{Pr}_2\text{Zr}_2\text{O}_7$.⁵

E (meV)	$ -4\rangle$	$ -3\rangle$	$ -2\rangle$	$ -1\rangle$	$ 0\rangle$	$ 1\rangle$	$ 2\rangle$	$ 3\rangle$	$ 4\rangle$
0	0	0	-0.094	0	0	-0.252	0	0	0.963
0	0.963	0	0	0.252	0	0	-0.094	0	0
9.53	0	-0.271	0	0	-0.924	0	0	0.271	0
57.15	0.008	0	-0.115	-0.028	0	-0.958	0.003	0	-0.262
57.15	-0.262	0	-0.003	0.958	0	-0.028	-0.115	0	-0.008
81.92	0	-0.653	0	0	0.383	0	0	0.653	0
93.21	0	0.707	0	0	0	0	0	0.707	0
108.73	0.060	0	0.147	0.134	0	-0.020	0.978	0	0.009
108.73	-0.009	0	0.978	-0.020	0	-0.134	-0.147	0	0.060

observed in magnetization measurements.⁴⁵ While the non-negligible inclusion of $|\pm 2\rangle$ and $|\pm 1\rangle$ enhances transverse fluctuations that are negligible in $\text{Ho}_2\text{Ti}_2\text{O}_7$ and $\text{Dy}_2\text{Ti}_2\text{O}_7$.⁵¹

2.3.2 Bulk Properties: Magnetic Susceptibility and Specific Heat

To go from single ion magnetic properties to collective magnetism, I will start with the thermomagnetic characterizations of $\text{Pr}_2\text{Zr}_2\text{O}_7$. The DC magnetization above 2 K was measured using a commercial SQUID magnetometer at a field of 1000 Oe. The temperature dependence of the AC susceptibility with an excitation field of 0.3 Oe below 5 K was measured down to 20 mK in a dilution refrigerator through a mutual inductance method. For both measurements, the field was applied along the [111] direction. The AC susceptibility data sets were scaled to data collected at 1000 Oe

for temperatures above 2 K. For all data, a demagnetization correction was made with a demagnetization factor $N = 0.2$. The specific heat was measured using a PPMS dilution refrigerator down to 0.07 K and a thin platelet single crystal with [111] surface normal.

No sharp transition was found in the magnetic susceptibility down to 20 mK, as shown in Fig. 2.13. This indicates the absence of magnetic long range order, which is a necessary condition for a spin liquid ground state. Instead, a frequency dependent response was observed, with peak positions $T_0(f)$ in the imaginary part of AC susceptibility χ'' that shift to lower temperatures for decreasing frequencies. The measurement frequency versus $1/T_0(f)$ follows the Arrhenius law $f = f_0 \exp(-\Delta_\chi/T_0(f))$ with an activation energy of $\Delta_\chi = 1.62(3)$ K. This spin freezing phenomenon seems similar to that in the classical spin ice $\text{Dy}_2\text{Ti}_2\text{O}_7$,⁵² however, the limiting frequency $f_0 \sim 1$ MHz from the Arrhenius law fitting is three orders of magnitude larger than for $\text{Dy}_2\text{Ti}_2\text{O}_7$, and the low temperature limit in χ' approaches half of the peak value in $\text{Pr}_2\text{Zr}_2\text{O}_7$ while it is vanishing in $\text{Dy}_2\text{Ti}_2\text{O}_7$. All these point to a more dynamical ground state in $\text{Pr}_2\text{Zr}_2\text{O}_7$.

Specific heat measurements provide further supporting evidence, in the absence of any sharp anomaly (Fig. 2.14). There are several contributors to the specific heat that correspond to different degrees of freedom and energy scales. At high temperature, lattice vibrations and higher CEF levels are the main players, and upon cooling lower energy fluctuations due to collective correlations between the CEF ground state

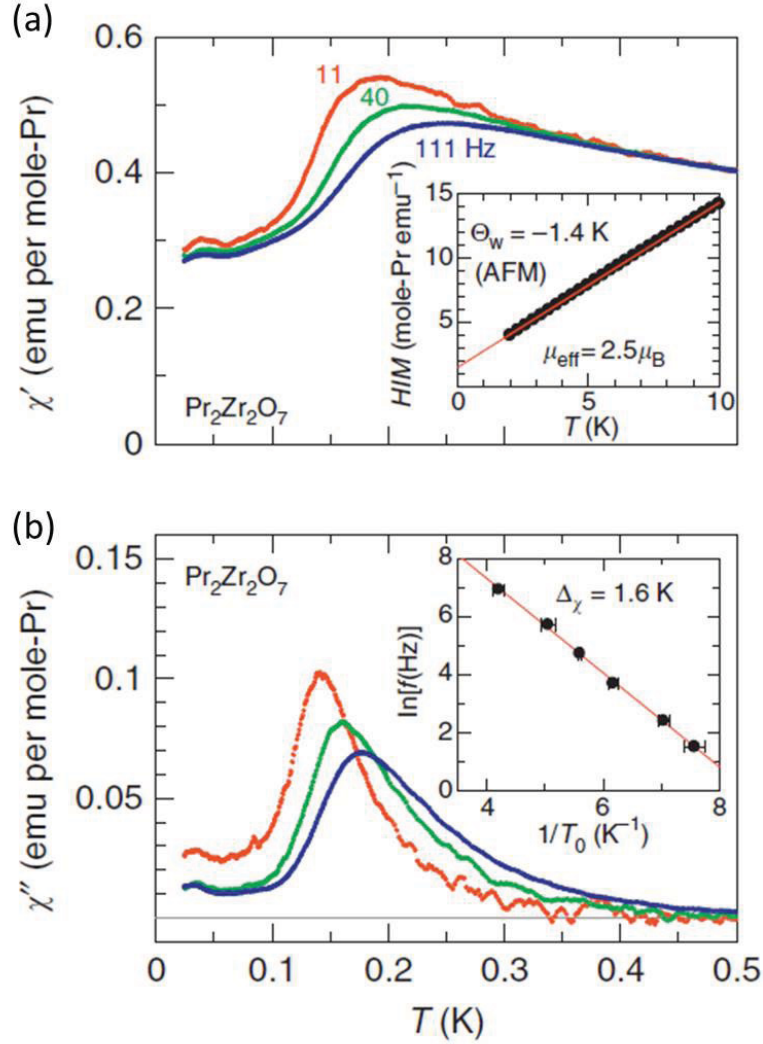


Figure 2.13: (a) Real part of the AC-susceptibility (χ'). Inset: Inverse DC-susceptibility from 10 to 2 K. (b) Imaginary part of the AC-susceptibility (χ''). Inset: Measurement frequency vs. inverse freezing temperature defined as the peak temperature for $\chi''(T)$. The solid line denotes a fit to the Arrhenius law, which yields an activation energy $\Delta_\chi = 1.6$ K.⁵

CHAPTER 2. QUANTUM SPIN ICE $\text{Pr}_2\text{Zr}_2\text{O}_7$

doublets become dominant. At even lower temperature nuclear spins will come into play. The lattice contribution was estimated from measurements on the non-magnetic analog $\text{La}_2\text{Zr}_2\text{O}_7$ and the contribution from higher CEF levels was calculated from the CEF level scheme determined from neutron CEF measurements. The low temperature magnetic and nuclear part of the specific heat (C_{MN}) was obtained after subtracting these two contributions from the experimental data. C_{MN} shows a broad peak at ~ 3 K that indicates development of spin correlation, and an upturn for $T \leq 0.3$ K. The degenerate nuclear spin levels ($I = 5/2$) of Pr (^{141}Pr , 100% natural abundance) can be split through hyperfine coupling with the electronic magnetic moments and this gives rise to a peak in the specific heat at low temperature called a nuclear Schottky anomaly⁵³ of the following form

$$C_{\text{Sch}} = Nk_B \frac{\alpha^2}{4I^2} \left[\frac{1}{\sinh^2(\alpha/2I)} - \frac{(2I+1)^2}{\sinh^2((2I+1)\alpha/2I)} \right]. \quad (2.5)$$

$$\alpha = A_{\text{hf}}(\mu_{\text{hyp}}^{(\text{Pr})}/g_J)I/k_B T. \quad (2.6)$$

Here, N and k_B are Avogadro's number and the Boltzmann constant, $I = 5/2$, and $A_{\text{hf}} = 0.052 \text{ K}^5$ are the nuclear spin and hyperfine coupling constant for ^{141}Pr . $g_J = 4/5$ and $\mu_{\text{hyp}}^{(\text{Pr})}$ are Lande's g -factor and the static Pr^{3+} magnetic dipole moment, which determines the hyperfine field.

Assume $\mu_{\text{hyp}}^{(\text{Pr})}$ to be the effective moment size ($\mu_{\text{eff}} = 2.5\mu_B$) of Pr^{3+} deduced from Curie-Weiss fitting of DC susceptibility (Inset in Fig. 2.13(a)), the calculated

C_{Sch} produced a specific heat peak that is much larger than the experimental low temperature upturn. To account for the experimental data, a modified expression for the nuclear hyperfine specific heat is instead used: $C_{\text{N}} = f \times C_{\text{Sch}}$ (Solid blue curve in Fig. 2.14(a)). Here, $f = 0.37$ is a dimension-less reduction factor representing the fraction of Pr sites with a dipole moment $\mu_{\text{hyp}}^{(\text{Pr})} = 0.82\mu_{\text{B}}$. The fact that $f < 1$ and $\mu_{\text{hyp}}^{(\text{Pr})} < 2.5 \mu_{\text{B}}$ may reflect low energy electronic spin fluctuations⁵⁵ and/or inhomogeneity associated with impurities.

Assigning in this way the low T upturn to nuclear spins, the electronic entropy obtained by integrating $C_{\text{M}}/T = (C_{\text{MN}} - C_{\text{N}})/T$ up to 20 K is $\Delta S_{\text{M}} = 0.75R \ln 2$, which is close to the value of $R \ln 2 - R/2 \ln(3/2) = 0.71R \ln 2$ for classical ice⁷ (Fig. 2.14(b)). The inferred zero-field magnetic component C_{M} shows activated T -dependence between 2 K and 0.2 K (Inset in Fig. 2.14(a)). The corresponding activation energy is $\Delta_{\text{C}} = 0.72(1)$ K, which is approximately half of that associated with AC-susceptibility data $\Delta_{\chi} = 1.62(3)$ K. Note that since there is no *a priori* reason to exclude the possibility that the low T upturn might also contain electronic contribution, the interpretation of specific data presented here is not unique.

2.3.3 Elastic and Inelastic Neutron Scattering

For a more direct view of the low energy spin dynamics in $\text{Pr}_2\text{Zr}_2\text{O}_7$, neutron scattering measurements were carried out on the Multi Axis Crystal Spectrometer (MACS)⁵⁶ at NIST Center for Neutron Research. One $\text{Pr}_2\text{Zr}_2\text{O}_7$ crystal (40 mm \times

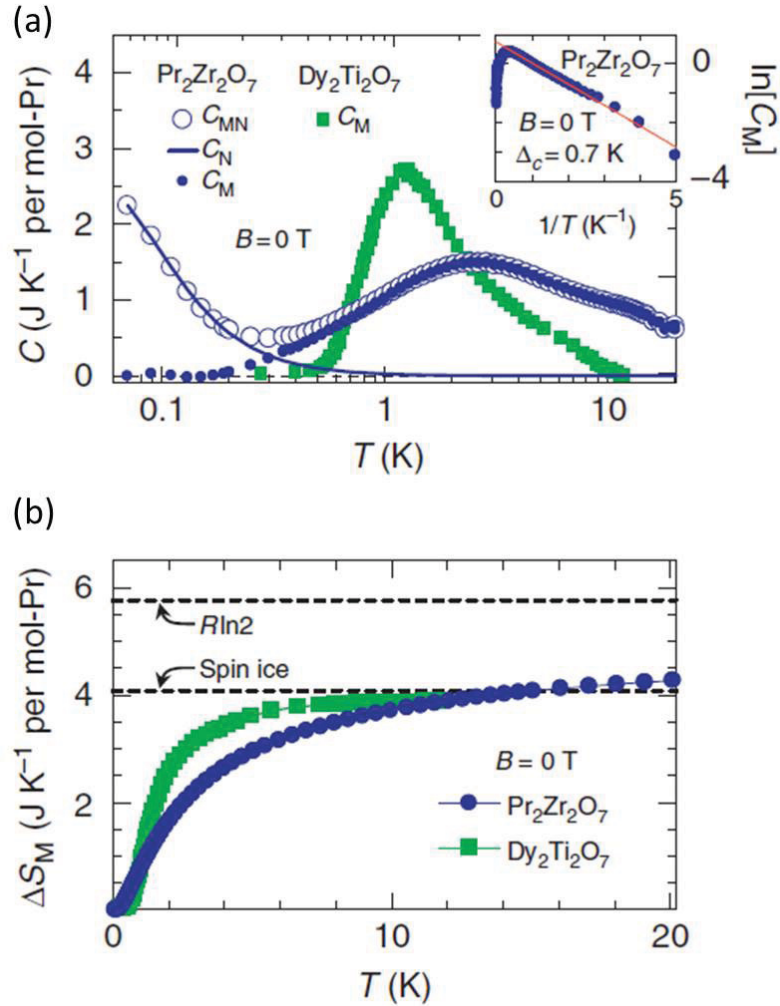


Figure 2.14: (a) Magnetic and nuclear part of the specific heat C_{MN} for $\text{Pr}_2\text{Zr}_2\text{O}_7$ after subtracting lattice and CEF contributions in zero field (open blue circle). A refined estimate $C_M = C_{MN} - C_N$ (filled blue circle) was obtained by subtracting a scaled nuclear Schottky-like anomaly (solid blue line). C_M for $\text{Dy}_2\text{Ti}_2\text{O}_7$ ⁷ is also shown for comparison (filled green square). Inset: C_M versus $1/T$ on a semi-logarithmic scale. The solid line denotes a fit to an Arrhenius law between 2 to 0.2 K, which yields an activation energy of 0.72(1) K. (b) Magnetic entropy ΔS_M (filled blue circle) for $\text{Pr}_2\text{Zr}_2\text{O}_7$ calculated from C_M . Open green squares show ΔS_M for $\text{Dy}_2\text{Ti}_2\text{O}_7$ ⁷. The dashed black lines denote the entropy for a two level system ($R \ln 2$) and the spin ice entropy defined as the difference between $R \ln 2$ and the Pauling entropy of $(1/2)(\ln(3/2)/\ln 2)R \ln 2 = 0.292R \ln 2$.⁵

CHAPTER 2. QUANTUM SPIN ICE $\text{Pr}_2\text{Zr}_2\text{O}_7$

20 mm² cylindrical single crystal) was mounted on an oxygen free copper holder and aligned in the (HHL) plane. The measured neutron scattering data were normalized to absolute unit by comparing to scattering from a known quantity of Vanadium, and the details of this normalization procedure can be found in Appendix B.

Nominal elastic scattering measured at 0.1 K with final neutron energy $E_f = 5$ meV is shown in Fig. 2.15(b). High temperature measurement at 22 K was used to subtract nuclear scattering contribution. The energy resolution for this configuration is $\delta E = 0.38$ meV, thus the elastic scattering should be considered to probe quasi-static spin correlations on the time scale of $\tau = \hbar/\delta E = 2$ ps. The observed broad intensity modulation in \mathbf{Q} -space is characteristic of a short-range correlated state. There are, however, sharp features at (002), (111), and ($\bar{1}\bar{1}1$) where the intensity modulation resembles a bow-tie like shape. These are called “pinch points” that arise from the local 2-in 2-out ice rule.²⁶ This is a direct evidence that at 0.1 K over a time scale of ~ 2 ps the spins in $\text{Pr}_2\text{Zr}_2\text{O}_7$ are correlated in a similar fashion as in classical spin ice.

The transverse width of the pinch points is a measure of the density of Pr tetrahedra that violate the ice rule,²⁶ whence the monopole density. To determine this density we used a high resolution configuration ($E_f = 2.7$ meV, $\delta E = 0.12$ meV) to measure the pattern of elastic neutron scattering for temperatures below 15 K within the (HHL) plane near the $\mathbf{Q} = (002)$ pinch point (Fig. 2.16). The pinch point width ξ was extracted by fitting the following phenomenological model of scattering to the

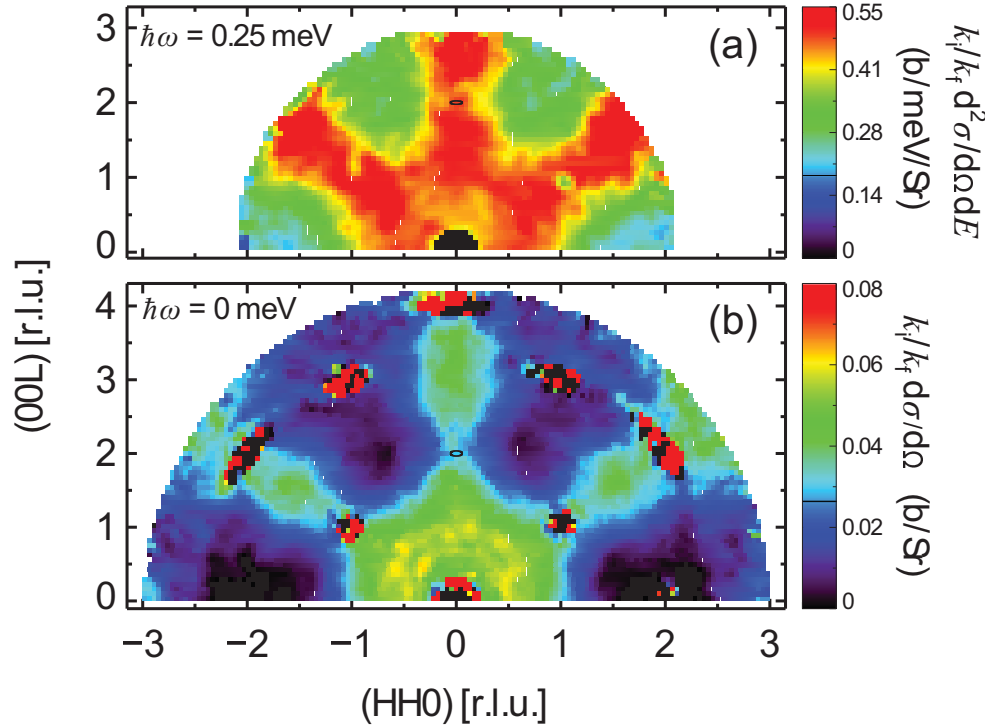


Figure 2.15: (a) Inelastic \mathbf{Q} -map with energy transfer of 0.25 meV obtained after subtracting the corresponding data at 15 K as background. The broad diffuse scattering pattern carries the symmetry of the crystal but cannot be associated with phonon scattering, which is concentrated around strong nuclear Bragg peaks at low energies. Instead we associate it with inelastic magnetic scattering. The fact that the scattering is wave vector dependent further links it to inter-site quantum spin dynamics. (b) Elastic \mathbf{Q} -map with pinch points at (002) , (111) , and $(\bar{1}\bar{1}1)$. By subtracting 22 K data from 0.1 K data to cancel elastic nuclear scattering processes at Bragg peaks, we obtain quasi-static spin correlations on the time scale of $\tau = \hbar/\delta E = 2$ ps. The black ellipses at (002) in **a** and **b** indicate the full width at half maximum instrumental resolution.⁵

two-dimensional intensity maps:

$$S(\mathbf{q}) = S(0) \frac{(\mathbf{c} \cdot (\mathbf{q} - 2\mathbf{c}))^2 + \xi^{-2}}{(\mathbf{q} - 2\mathbf{c})^2 + \xi^{-2}}. \quad (2.7)$$

where $\mathbf{c} \equiv \frac{2\pi}{a} \mathbf{e}_c$ is the reciprocal lattice unit vector along the c direction.

Both the quasi-static ($\tau > \hbar/\delta E = 5.5$ ps) total moment $S(0)$, and the spin ice correlation length ξ increase on cooling (Fig. 2.18). The low T limit, ξ_0 , indicates a quasi-static monopole density of 1.2%. This can be compared to the $\sim 1\%$ concentration of Zr on Pr sites determined by single crystal synchrotron X-ray diffraction on this sample.⁵ The fitting function, $1/\xi = 1/\xi_0 + A/\exp(\Delta_\chi/T)$, (black solid line, Fig. 2.18(a)) describes the data well with the activation energy fixed at the value of $\Delta_\chi = 1.6$ K extracted from AC- $\chi(T)$ data. Furthermore, momentum-space-averaged elastic neutron cross-section (Fig. 2.18(b)) shows that the observed elastic scattering at 0.1 K represents just 7(2)% of the total scattering expected from the CEF ground state doublet, pointing to a predominantly dynamic magnetic ground state in $\text{Pr}_2\text{Zr}_2\text{O}_7$.

Fig. 2.15(a) shows the inelastic neutron scattering intensity map measured at 0.1 K with energy transfer of 0.25 meV ($E_f = 2.7$ meV). The existence of low energy inelastic neutron scattering at low temperature provides strong contrast with classical spin ice materials where no inelastic neutron scattering is expected at similar temperatures. As energy transfer $\hbar\omega \gg k_B T$, these excitations are of a quantum - as opposed to a

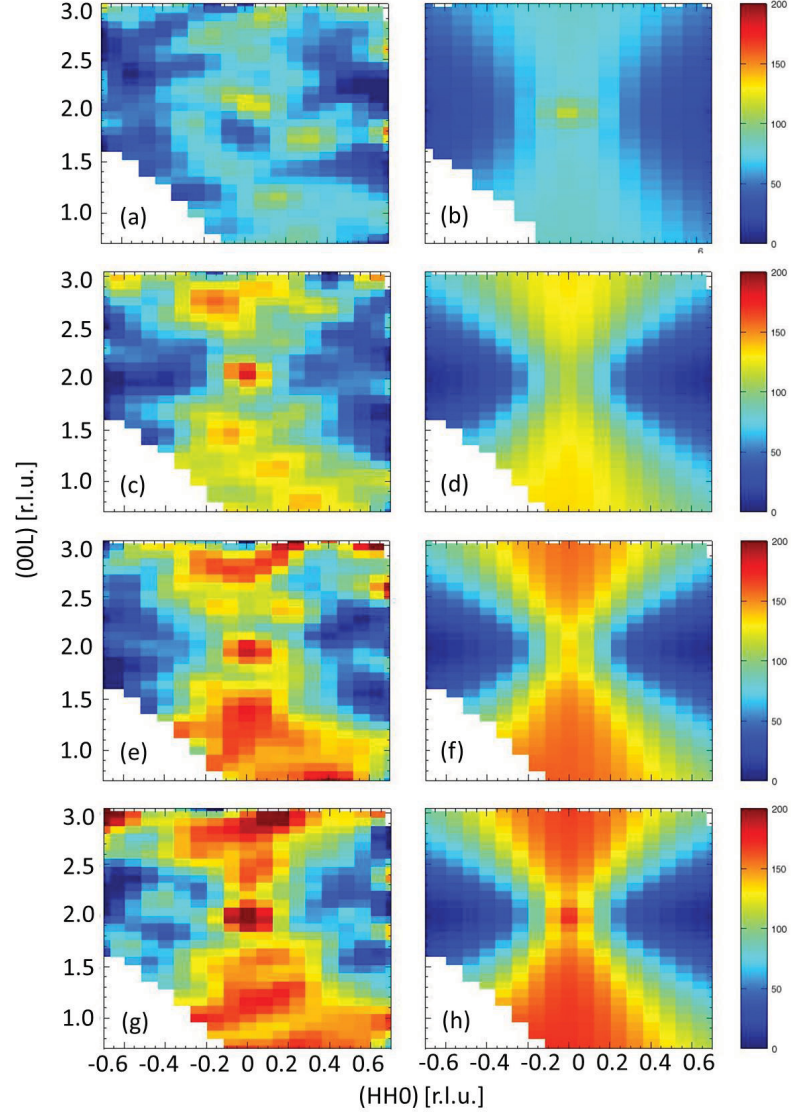


Figure 2.16: Temperature dependent elastic neutron scattering maps around the absent Bragg peak (002) measured with $E_f = 2.7$ meV. A map of intensity acquired at 15 K was used to subtract out nuclear scattering contributions. (a), (c), (e), and (g) show experimental data at 4.25 K, 1.5 K, 0.5 K, and 0.1 K, while (b), (d), (f), and (h) show the corresponding best fit based on Eq. 2.7.

thermal - nature. The overall shape of the intensity modulation in momentum space is similar to the elastic intensity map, but the pinch points have vanished. Since pinch are associated with spin configurations that satisfy the ice rule, this suggests the excited states are different from the ground state with the appearance of ice-rule breaking tetrahedra, namely the creation of magnetic monopoles through a quantum process.

To characterize in detail the excitation spectrum, energy scans at temperatures between 0.1 K and 15 K were carried out at $\mathbf{Q} = (003)$ (Fig. 2.17). No energy gap is observed in the low temperature spectrum which sets an upper limit of $\Delta E = 0.2$ meV on any excitation gap. The spectrum takes the form of a continuum that broadens upon warming. The 15 K data were used to subtract the temperature independent scattering contribution from lower temperature measurements. Assuming the magnetic response can be approximated by a single pole response function, $\chi = \chi_0\Gamma/(\Gamma - i\omega)$, for all T , the function describing the difference between low T and 15 K data takes the following form

$$I(T, \omega) = (1 + n(T, \omega)) \frac{\chi_0(T)\Gamma(T)\omega}{\Gamma(T)^2 + \omega^2} - (1 + n(15 \text{ K}, \omega)) \frac{\chi_0(15 \text{ K})\Gamma(15 \text{ K})\omega}{\Gamma(15 \text{ K})^2 + \omega^2}. \quad (2.8)$$

Here $n(T, \omega) = 1/(e^{\beta\hbar\omega} - 1)$ and $\beta = 1/k_{\text{B}}T$. Because there was no filter in the incident beam, all monitor normalized data were corrected by an energy dependent factor to account for the contribution to the monitor count rate from $\lambda/2$ neutrons.

CHAPTER 2. QUANTUM SPIN ICE $\text{Pr}_2\text{Zr}_2\text{O}_7$

After subtracting the 15 K data the difference data sets were simultaneously fitted to Eq. (2.8) convoluted with energy resolution function and with common parameters for the 15 K response function. Data points where $|\hbar\omega| \leq 0.1$ meV were excluded from this analysis because they are affected by proximity to the elastic line and cannot be described by Eq. 2.8. In this fashion we extracted a temperature dependent relaxation rate, $\Gamma(T)$, as shown by the red solid symbols in Fig. 2.18(a). The red solid line shows $\Gamma(T) = \sqrt{(\Gamma_0)^2 + (Ck_B T)^2}$, where $C = 1.4(2)$. The crossover to linearity and thus ω/T scaling is evidence of a regime for $T > J_{ff}$ where T is the only relevant energy scale. In the low T limit, $\Gamma \sim 0.17$ meV is similar to the spin flip energy $2J_{ff} = \Delta_\chi \sim 1.6$ K inferred from AC- $\chi(T)$.

The combination of thermomagnetic measurements and neutron scattering data leads to several compelling characteristics of low temperature magnetism in $\text{Pr}_2\text{Zr}_2\text{O}_7$:

- Strong quantum fluctuations: At $T = 0.1$ K, more than 90% of the magnetic scattering cross section is inelastic, the attempt frequency associated with the activated AC susceptibility is three orders of magnitude larger than for classical spin ice, and the nuclear Schottky anomaly is suppressed below that for a classical frozen state both in terms of moment density *and* magnitude.
- Weak static correlations: Exponentially activated specific heat and AC susceptibility data, elastic magnetic neutron scattering, and the nuclear Schottky anomaly consistently indicate some spin-freezing.

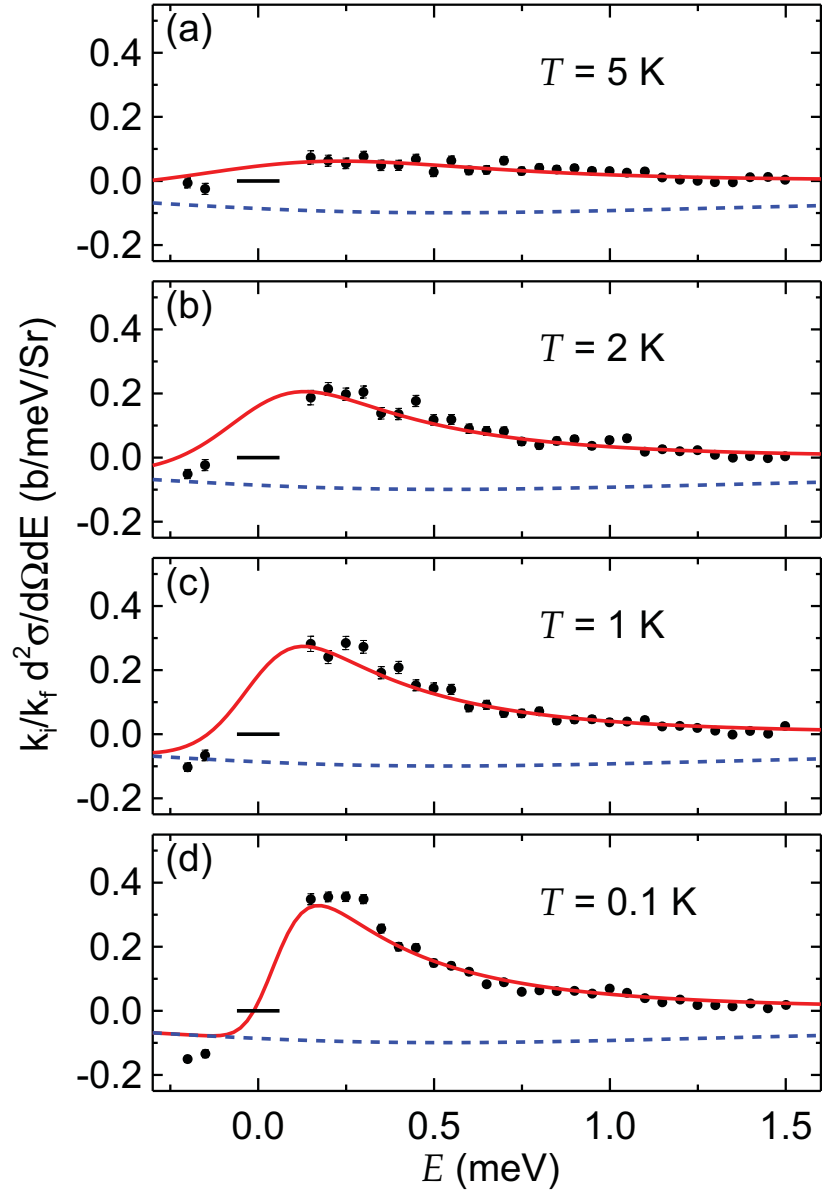


Figure 2.17: Temperature dependent inelastic neutron scattering spectra at $Q = (003)$ after subtraction of data measured at 15 K. A correction to the monitor rate was applied to account for order contamination in the unfiltered incident beam. The fitting curve and the corresponding background resulting from subtraction of magnetic scattering at $T = 15$ K to derive Γ are shown by red solid and blue dashed curves, respectively. The solid black bar represents the instrumental energy resolution.

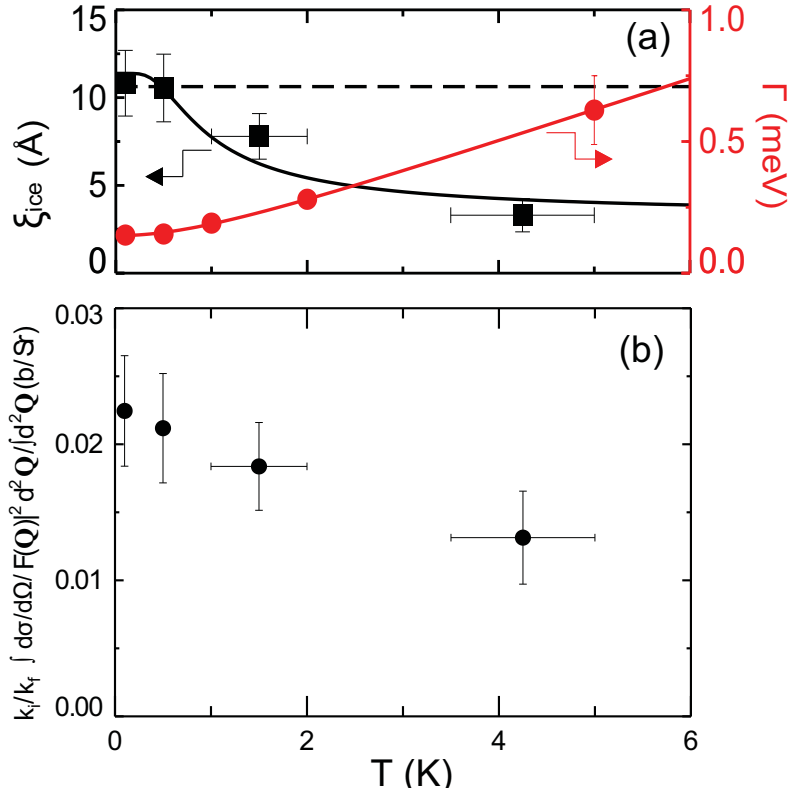


Figure 2.18: (a) Temperature dependence of the spin ice correlation length ξ_{ice} (left) and the relaxation rate Γ (right). The black solid line denotes $1/\xi_{\text{ice}} = 1/\xi_0 + A/\exp(\Delta_\chi/T)$ with the activation energy fixed at the value of $\Delta_\chi = 1.62(3)$ K. The red solid line shows $\Gamma(T) = \sqrt{(\Gamma_0)^2 + (Ck_B T)^2}$, where $C = 1.4(2)$. The black horizontal dashed line indicates the mean distance between 1% of the Pr sites, which according to synchrotron X-ray analysis are occupied by Zr. (b) Temperature dependent elastic magnetic neutron scattering cross section from $\text{Pr}_2\text{Zr}_2\text{O}_7$ inferred from fits in Fig. 2.16. These data represent the quasi-static total moment squared, averaged over the momentum space where the data were collected. The observed elastic scattering represents just 7(2)% of the elastic scattering cross section associated with a fully frozen state.⁵

- Spin-ice-like correlations at long times: The wave vector dependence of the lowest energy scattering detected features pinch points, the width of which is consistent with the inferred chemical defect density.

All of these observations make $\text{Pr}_2\text{Zr}_2\text{O}_7$ an unique material that is spin-ice-like but with strong quantum fluctuations. A better understanding of the excitation spectrum could provide further insight and constraint regarding the magnetic ground state in $\text{Pr}_2\text{Zr}_2\text{O}_7$ and this is the subject of the next section.

2.4 Random Transverse Fields on a Quantum Spin Ice

In this section, through systematic inelastic neutron scattering measurements in extensive temperature-magnetic field ($T-H$) phase space, the nature of the excitation spectrum of $\text{Pr}_2\text{Zr}_2\text{O}_7$ is explored, revealing an intricate interplay between spin and lattice degrees of freedom in this non-Kramers spin system.

Single crystalline $\text{Pr}_2\text{Zr}_2\text{O}_7$ samples were prepared by floating zone growth technique under optimized conditions as discussed in Sec. 2.2. 5 and 3 single crystals were co-aligned for measurements in the (HLL) and $(HK0)$ plane respectively, with total mass of 9.5 g and 8.8 g (Fig. 2.19). Neutron scattering measurements were carried out on the Disk Chopper Time-of-Flight Spectrometer (DCS)⁵⁷ at NIST Center for Neu-

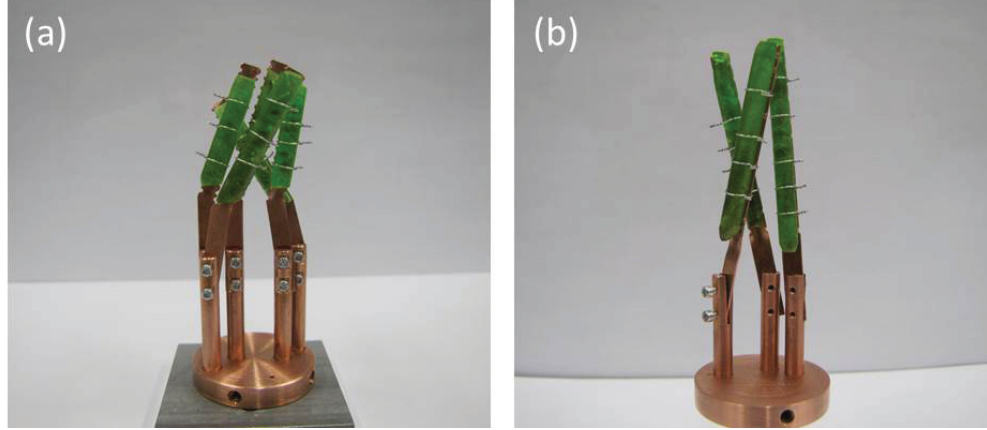


Figure 2.19: Single crystalline $\text{Pr}_2\text{Zr}_2\text{O}_7$ assemblies used for neutron scattering measurements in (a) (HHL) plane and (b) $(HK0)$ plane respectively.

tron Research. Unless otherwise noted data were collected with 5 \AA incident neutron wavelength. Experimental data were converted to absolute unit by normalization with respect to nuclear Bragg peak (220) .

Momentum space averaged data provide an overview of the excitation spectrum of $\text{Pr}_2\text{Zr}_2\text{O}_7$ and are shown in Fig. 2.20. At $T = 1.4 \text{ K}$ and $\mathbf{H} = 0 \text{ T}$, the spectrum takes the form of a broad peak that extends to at least 2 meV , consistent with previous measurements on MACS (Fig. 2.17). This spectrum is rather broad considering the energy gap Δ_{AC} extracted from AC magnetic susceptibility measurement is only 1.6 K (Fig. 2.13). To understand why we examine temperature and magnetic field dependence.

The field dependence of the spectrum provides the first insight. Strong $\langle 111 \rangle$ Ising anisotropy of the spins predicts that for $\mathbf{H} \parallel (1\bar{1}0)$, spins are partitioned into two sets of chains with different field projections along the easy axes, while for $\mathbf{H} \parallel (001)$,

the angle from easy (111) type directions to the field axis are identical. As shown in Fig. 2.20(a), spectrum measured under these two field directions show 2 and 1 components respectively, revealing that these excitations are influenced by the field component along the easy axis and are of magnetic origin. The spectra measured for different magnetic field strengths along (001) (Fig. 2.20(b)) show that the field dependence is in fact rather nontrivial. For normal magnetic materials the application of a magnetic field shifts the inelastic neutron scattering intensities to higher energies, however in $\text{Pr}_2\text{Zr}_2\text{O}_7$ there is only a loss of spectral weight at lower energies while the spectral weight at higher energies stays almost invariant.

The unusual thermal evolution of the spectrum is a defining character of the underlying excitations. Fig. 2.20(c) shows the spectrum measured with $\mathbf{H} = 4 \text{ T}$ \parallel (001) at temperatures from 1.1 K up to 200 K. The \mathbf{Q} -average inelastic neutron scattering intensity was multiplied by a thermal factor $F_{th}(T, \hbar\omega)$

$$\begin{aligned} F_{th}(T, \hbar\omega) &= \left(\frac{e^{\beta\hbar\omega/2}}{e^{\beta\hbar\omega/2} + e^{-\beta\hbar\omega/2} + Z'} \right)^{-1} \\ &= (1 + e^{-\beta\hbar\omega} + e^{-\beta\hbar\omega/2} Z') \end{aligned} \quad (2.9)$$

where $\beta = 1/k_{\text{B}}T$, $Z' = \sum_{E'} e^{-\beta E'}$ with E' running through all CEF levels above the ground state doublet as determined in Sec. 2.3. If the excitations correspond to transitions between CEF ground state doublet levels that are, for some reason, split by an energy gap of $\hbar\omega$, the normalized spectrum at different temperatures should fall

on a single curve.⁵⁸ This is found to hold true for measurements with $|\hbar\omega| \geq 0.9$ meV. This suggests that a quenched and perhaps inhomogeneous distribution of doublet splitting is responsible for the higher energy part of the spectrum.

A closer look at the spectrum with momentum space resolution provides essential information regarding spin-spin correlations. This was done by making 2D cuts through the 3D $\mathbf{Q} - E$ data set. Fig. 2.21 shows a series of such cuts along the $(H20)$ direction for various magnetic fields along (001) direction. A broad spectrum is observed throughout \mathbf{Q} space that moves up in energy with increasing field. No discernible dispersion is observed. This contrasts with $\text{Yb}_2\text{Ti}_2\text{O}_7$, another quantum spin ice candidate material, where sharp spin wave modes emerge under field.³⁷ The main wave vector dependent aspect of the data is intensity modulation at the lower edge with a maximum around (020) . This modulation is more than what is expected from magnetic form factor in the \mathbf{Q} range probed, so it is inferred to be due to inter-site spin correlations. The modulation diminishes at higher energies, consistent with Fig. 2.20(c) where the high energy part of the spectrum is associated with splitting of the CEF ground state doublet, a local excitation that carries no modulation in \mathbf{Q} space.

More information regarding spatial spin correlations is extracted through constant energy slices through the data. Fig. 2.22 shows such slices covering the (HHL) plane, with data folded into first quadrant for better statistics. Figs. 2.22(a)(c) show measurements at $\mathbf{H} = 0$ T. While no modulation is observed at high ener-

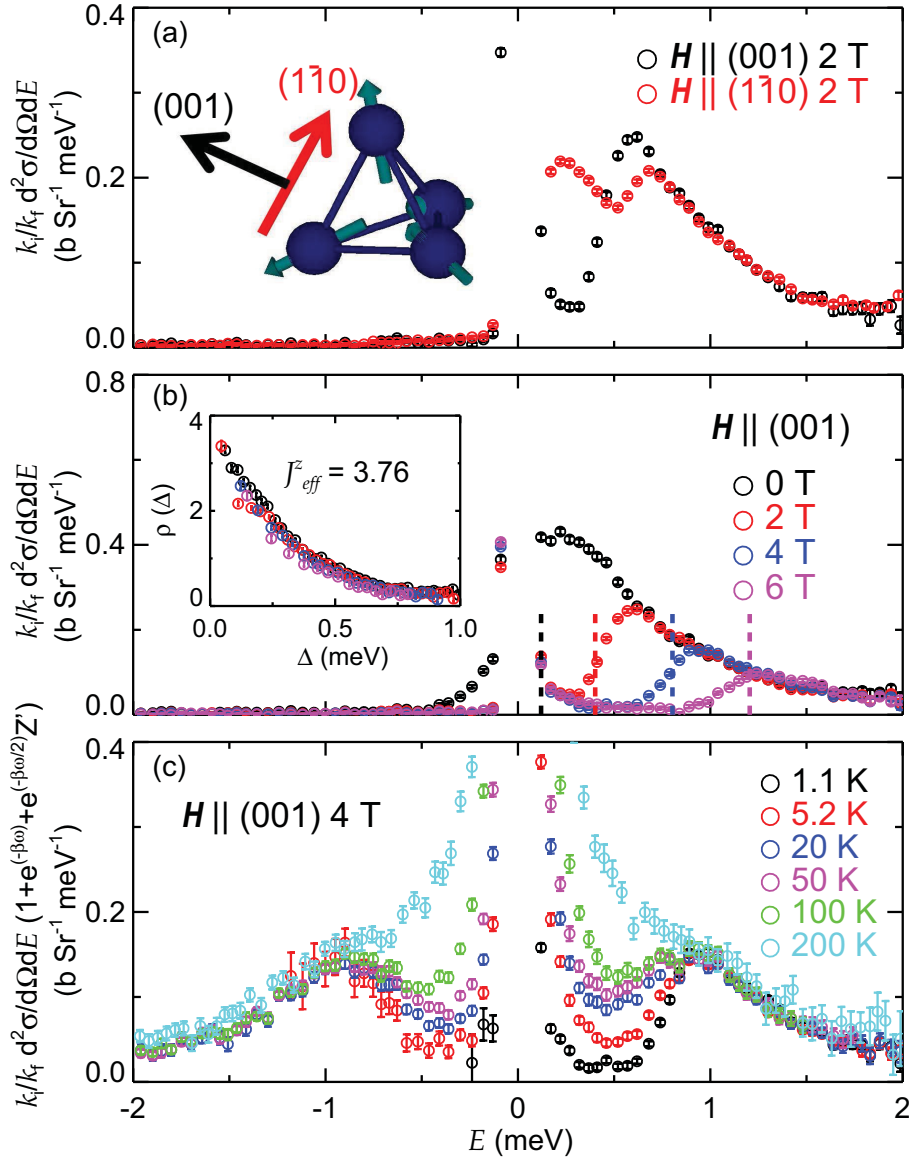


Figure 2.20: Momentum space averaged spectrum for $0.5 \text{ \AA}^{-1} \leq |\mathbf{Q}| \leq 2.2 \text{ \AA}^{-1}$ in the corresponding scattering plane. (a) Spectrum for $\mathbf{H} \parallel (001)$, $T = 1.4$ K (black circle) and $\mathbf{H} \parallel (1\bar{1}0)$, $T = 0.2$ K (red circle). $|\mathbf{H}| = 2$ T in both measurements. Inset is a schematic representation of the relative orientation of the applied field and the spin directions. (b) Field dependent spectrum for $\mathbf{H} \parallel (001)$ at $T = 1.4$ K. The distribution of transverse field $\rho(\Delta)$ extracted from the spectrum was shown in the inset. The corresponding Zeeman gap energies are shown as dashed vertical lines, data points above which were used to calculate $\rho(\Delta)$. For 0 field, data points with $E \geq 0.1$ meV were used to avoid elastic line. (c) Temperature dependent spectrum for $\mathbf{H} \parallel (001)$, 4 T. A thermal distribution factor F_{th} were applied to the data.

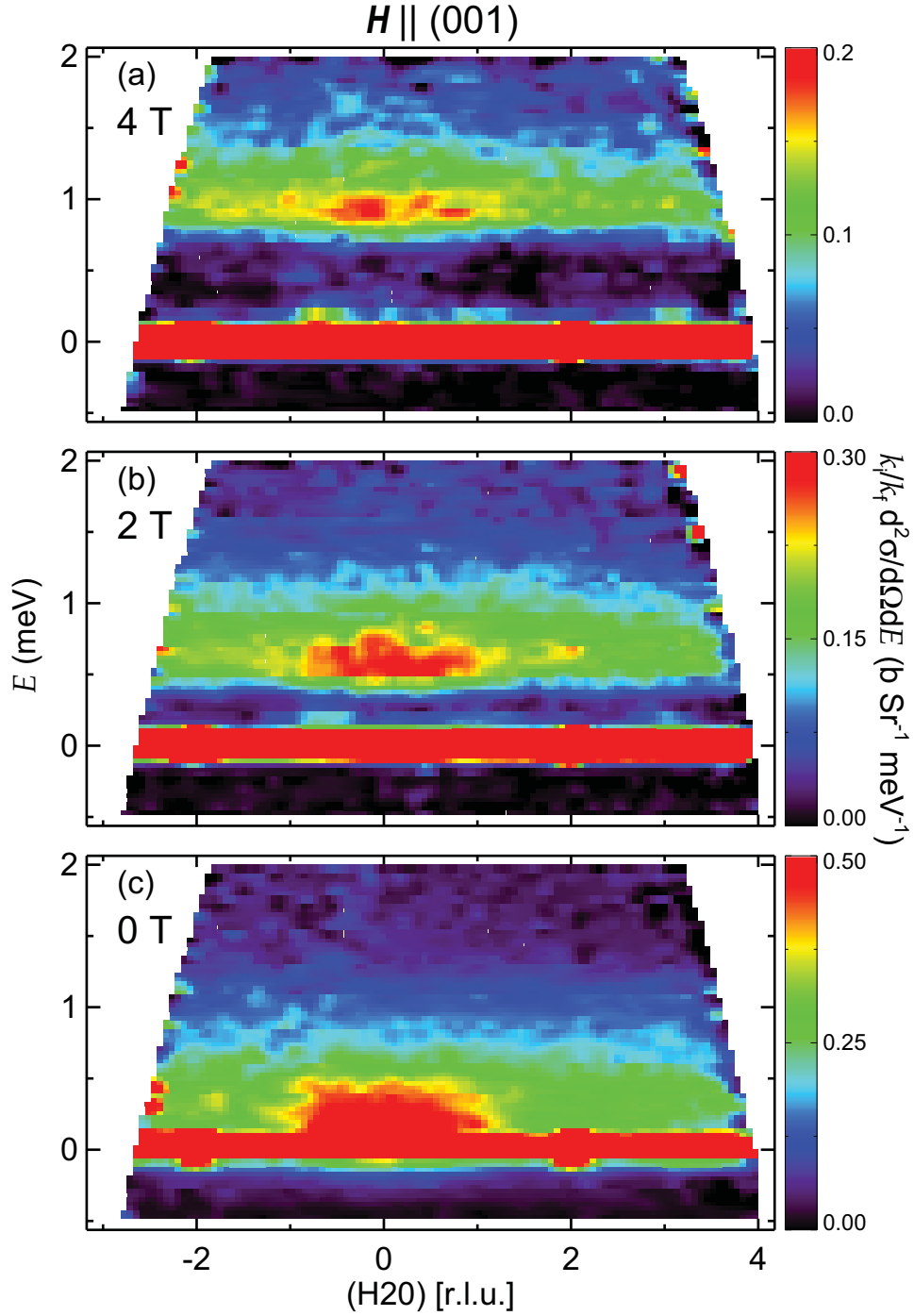


Figure 2.21: Field dependent $Q - E$ slice for $H \parallel (001)$, $T = 1.4$ K. Data were integrated along $(0K0)$ for $1 \text{ (r.l.u.)} \leq K \leq 3 \text{ (r.l.u.)}$. (a),(b),and (c) shows corresponding data for $|H| = 4 \text{ T}$, 2 T , and 0 T

gies (Fig. 2.22(a)), a star-fish-like intensity modulation (Fig. 2.22(c)) is observed at low energies that is consistent with previous measurements on MACS (Fig. 2.15(a)). By applying a magnetic field along the $(1\bar{1}0)$ direction, the low energy modulation evolves into a single rod along $(00L)$ that is characteristic of low dimensional correlations (Fig. 2.22(e)). As previously mentioned, a magnetic field along this direction segregates the pyrochlore lattice into two sets of disentangled chains. Correspondingly this low energy scattering can be associated with Pr chains extending along the (110) direction. For those spins the magnetic field lies perpendicular to the easy axis. In Fig. 2.22(c), the intensity maxima at (111) , (112) , (113) , and (222) are instrumental spurions that result from leakage of strong elastic scattering intensity, which has contribution from both nuclear scattering and field induced magnetic scattering, into the inelastic channel.

To sum up the experimental observation so far: (1) the high energy part of the spectrum is consistent with scattering from split doublets, the distribution of which is temperature independent up to 200 K. This is supported by the temperature dependence of the spectrum (Fig. 2.20(c)) and the lack of \mathbf{Q} dependence which is characteristic of scattering from local excitations that do not involve inter-site interactions. (2) Inter-site correlations are however, apparent for the the low energy part of the spectrum which is modulated in \mathbf{Q} space.

To understand the data I will start with the description of the single ion part of the problem. Since the relevant energy range is well below the first excited CEF

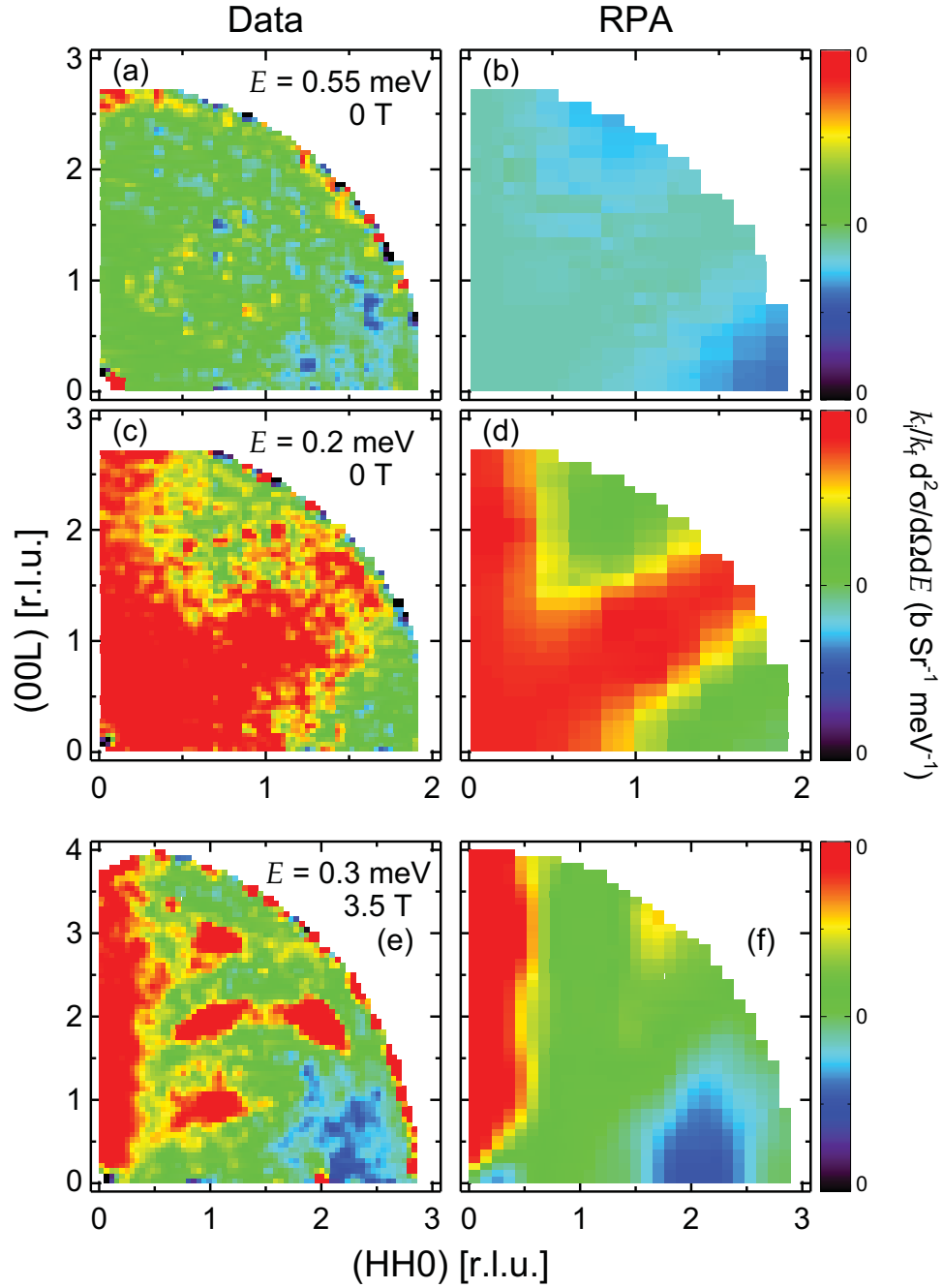


Figure 2.22: Q -maps in (HHL) plane. Data were folded into the first quadrant for optimal statistics. (a) and (c) shows data measured with 7 \AA incident neutron wavelength at 0.05 K , 0 T with energy integration of $[0.1, 0.3] \text{ meV}$ and $[0.3, 0.8] \text{ meV}$ respectively. (e) shows data with 5 \AA incident neutron wavelength at 0.2 K , 3.5 T with energy integration of $[0.1, 0.5] \text{ meV}$. (b), (d), and (f) shows corresponding calculation of neutron cross-section within RPA.

CHAPTER 2. QUANTUM SPIN ICE $\text{PR}_2\text{ZR}_2\text{O}_7$

level (~ 10 meV), it is a good approximation to work in the sub Hilbert space of the ground state doublet. In this subspace, the total spin operator in the local frame takes the form of $J_x = 0, J_y = 0, J_z = J_{eff}^z \sigma_z$, with z the local $\langle 111 \rangle$ direction. Here σ_i are the Pauli matrices and J_{eff}^z is the effective spin size of the ground state doublet. Any splitting of this doublet can be effectively described in terms of a transverse field Δ . Thus without loss of generality the single ion part of the spin Hamiltonian can be written as

$$\mathcal{H}_{\text{SI}} = -g\mathbf{H} \cdot \mathbf{e}_z J_{eff}^z \sigma_z + \Delta \sigma_x \quad (2.10)$$

Here g is the Landé g -factor, \mathbf{e}_z is the unit vector along the local easy axis. The first term describes the Zeeman coupling and the second term accounts for the “intrinsic” splitting of the doublet. I fix $J_{eff}^z = \langle J_z \rangle = 3.76$ to the value determined from the ground state doublet wavefunction as deduced from the neutron CEF study presented in Sec. 2.3. This should be considered as a sample averaged value. The distribution of energy gaps between the split doublets will be described in terms of $\rho(\Delta)$, the distribution of transverse field Δ . For a certain distribution $\rho(\Delta)$ the corresponding inelastic neutron scattering cross section can be calculated by

$$I(E) = \mathcal{C} \cdot (\gamma r_0)^2 (g/2)^2 |\langle \phi_1 | J_z | \phi_2 \rangle|^2 \rho(\Delta) \frac{E}{\Delta \cdot F_{th}(T, E)} \quad (2.11)$$

CHAPTER 2. QUANTUM SPIN ICE $\text{Pr}_2\text{Zr}_2\text{O}_7$

Here γ is the gyromagnetic ratio of neutron and r_0 is the classical electron radius, $|\phi_1\rangle, |\phi_2\rangle$ are the two eigenstates of \mathcal{H}_{SI} , $E = 2\sqrt{(g\mathbf{H} \cdot J_{eff}^z \mathbf{e}_z)^2 + \Delta^2}$ is the energy splitting of the doublet, \mathcal{C} is a numerical constant that contains information including the average of the magnetic form factor and polarization factor. Thus through Eq. (2.11) $\rho(\Delta)$ can be extracted from the measured spectrum, up to a numerical constant. Eq. (2.11) also predicts the way the spectrum should change as a function of magnetic field, thus if the proposed \mathcal{H}_{SI} is a good approximation of the real material then $\rho(\Delta)$ extracted from data measured at different fields should be consistent. This extraction of $\rho(\Delta)$ was carried out for the field dependent spectra in Fig. 2.20(b). \mathcal{C} in Eq. 2.11 was determined such that $\rho(\Delta)$ obtained from the 0 field spectrum is normalized to unity, i.e., $\int \rho(\Delta)d\Delta = 1$. As shown in the inset to Fig. 2.20(b), $\rho(\Delta)$ extracted from data acquired at different fields all fall onto a single curve. This lends strong support to \mathcal{H}_{SI} as a description of the low energy magnetism of $\text{Pr}_2\text{Zr}_2\text{O}_7$. For the zero field spectrum only data points with $\hbar\omega \geq 0.1$ meV were used to avoid influences from the elastic line. For finite fields, data points with $\hbar\omega$ larger than the Zeeman gap ($2g\mathbf{H} \cdot J_{eff}^z \mathbf{e}_z$) were used to extract $\rho(\Delta)$. The success of a single ion description and the associated continuous distribution function $\rho(\Delta)$ indicates that for Pr in $\text{Pr}_2\text{Zr}_2\text{O}_7$ there is a broad range of random transverse fields on the CEF ground state doublet extending at least up to 2 meV.

Elastic scattering measurements provide further information regarding the inhomogeneity of spins in $\text{Pr}_2\text{Zr}_2\text{O}_7$. For $\mathbf{H} \parallel (001)$ all spins have the same field pro-

jection, thus homogeneous spins should be uniformly magnetized and produce sharp magnetic Bragg diffraction. In contrast, a broader line shape is expected for inhomogeneous spins due to inhomogeneous magnetization. Fig. 2.23(b) shows a comparison between the line shape of (220) nuclear Bragg peak and that of the (200) magnetic Bragg peak. There is indeed an additional tail to the magnetic peak shape. Note that slight misalignment of \mathbf{H} from (001) will not induce the long tail in the homogenous case since as long as each unit cell is uniformly magnetized, the (200) magnetic peak should be sharp like a nuclear Bragg peak.

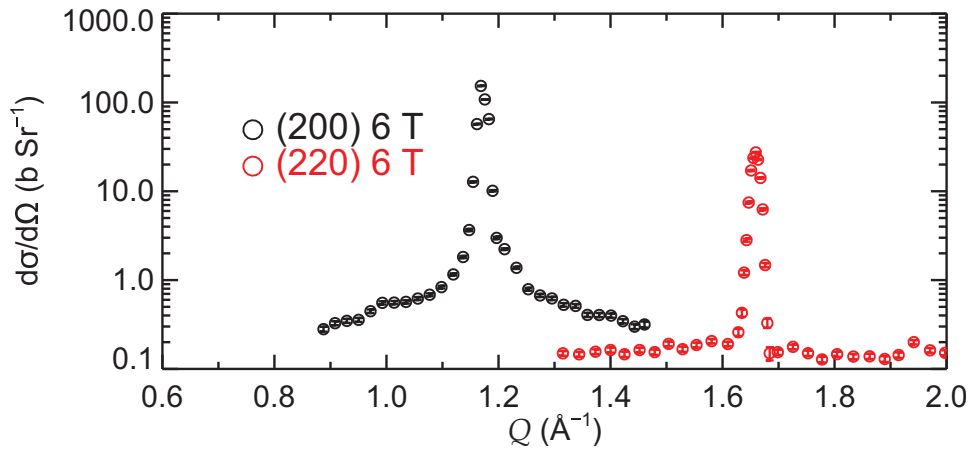


Figure 2.23: Longitudinal elastic cuts for magnetic (200) and nuclear (220) peaks with $\mathbf{H} = 6 \text{ T} \parallel (001)$, $T = 1.5 \text{ K}$.

The Ising model with inhomogeneous transverse field (\mathcal{H}_{SI}) provides a good description of the high energy part of the inelastic spectrum. As for the lower energy part of the spectrum where inter-site interactions are important, I consider the minimal interacting Hamiltonian relevant to this material with only Spin Ice interactions

(J_{zz} in Eq. 2.2):

$$\mathcal{H}_{\text{IT}} = -J \sum_{\langle i,j \rangle} J_{iz} J_{jz} (\mathbf{e}_{iz} \cdot \mathbf{e}_{jz}) + \sum_i \mathcal{H}_{\text{SI}} \quad (2.12)$$

Here $\langle i, j \rangle$ runs over distinct nearest neighbors. If Δ_{AC} is regarded as the energy cost for creating a single monopole, J can be estimated to be $J = 0.016$ meV. We treat the interaction on the level of Random Phase Approximation (RPA),⁵⁹ where the RPA susceptibility $\chi(ij, \omega)$ is solved self consistently through

$$\chi(ij, \omega) = \chi_i^0(\omega) (\delta_{ij} + \sum_{j'} J(ij') \chi(j'j, \omega)) \quad (2.13)$$

Here $\chi^0(\omega)$ is the single ion susceptibility due to non-interacting part of the Hamiltonian and $J(ij)$ is the exchange constant between the spins at site i and j . The detail implementation of the RPA calculation is described in Appendix. C.

The inhomogeneity in \mathcal{H}_{SI} makes it difficult to carry out the standard RPA calculation, where χ_i^0 has the periodicity of the lattice. To a first approximation, I first calculated the RPA susceptibility $\chi(\omega, \Delta)$ assuming all spins have homogeneous transverse field Δ , then approximated the final susceptibility as a weighted average $\rho(\Delta)$, $\chi(\omega) = \int \rho(\Delta) \chi(\omega, \Delta) d\Delta$. The $\rho(\Delta)$ as calculated from the 0 T data in Fig. 2.20(b) was used in this averaging procedure. Such an approach is expected to work well for small Δ where $\rho(\Delta)$ is large, while for large Δ it is expected to overestimate correlations since in reality a spin with large Δ is unlikely to find its neighbors to have

CHAPTER 2. QUANTUM SPIN ICE $\text{Pr}_2\text{Zr}_2\text{O}_7$

similar Δ . The neutron cross section is related the imaginary part of the susceptibility through Fluctuation Dissipation theorem:⁴⁷

$$\frac{d^2\sigma}{d\Omega dE}(\mathbf{Q}, \omega) \sim S(\mathbf{Q}, \omega) \sim \frac{1}{1 - e^{-\beta\hbar\omega}} \chi''(\mathbf{Q}, \omega) \quad (2.14)$$

Here $S(\mathbf{Q}, \omega)$ is the correlation function that is measured by neutron scattering. All the RPA results were scaled by a single factor to compare to the experimental data. Fig. 2.22 (b),(d), and (f) show the RPA calculations are in excellent agreement with the corresponding experimental results.

\mathcal{H}_{IT} has been shown to provide a good description of the excitation spectrum in $\text{Pr}_2\text{Zr}_2\text{O}_7$. A natural question at this point is what might be the physical origin of the doublet splitting. Being a non-Kramers ion with an even number of electrons, the CEF ground state doublet of Pr^{3+} is not protected by time reversal symmetry, but instead by the local D_{3d} point group symmetry. Thus the split doublet suggests lowering of the local symmetry at the Pr site. Single crystal X-ray diffraction from high quality $\text{Pr}_2\text{Zr}_2\text{O}_7$ at 110 K shows no sign of a structural distortion from the ideal pyrochlore structure, placing strict limits on any cooperative Jahn-Teller distortion.⁶⁰ The deviation from pyrochlore symmetry is thus expected to occur locally and in a manner that breaks translational symmetry. Recall that the structural study on polycrystalline $\text{Pr}_{2+x}\text{Zr}_{2-x}\text{O}_{7-x/2}$ in Sec. 2.2 suggests Pr off-centering even in the stoichiometric sample, thus this distortion is likely to be intrinsic to this material.

CHAPTER 2. QUANTUM SPIN ICE $\text{Pr}_2\text{Zr}_2\text{O}_7$

The distortion can be static or dynamic. In the dynamic scenario Pr ions interact with the lattice environment through magneto-elastic effect. Each Pr site is still equivalent but exhibit a spectrum of splitting reflecting the phonon density of state. The observation that the doublet splitting is stable up to 200 K (Fig. 2.20(c)) and the existence of inhomogeneous magnetization indicated by the tails of the field induced Bragg like scattering (Fig. 2.23) suggests that the local distortion is in fact quenched.

This quenched transverse field is expected to have crucial influence on the low temperature magnetism. On the single ion level, sites with $\Delta \gg \max\{T, J_{ff}(J_{eff}^z)^2\}$ will be essentially non-magnetic and act as dilution to the magnetic pyrochlore lattice. In addition, a distribution of splitting implies inhomogeneous exchange interactions J since exchange is sensitive to the Pr-O configurations that determine the exchange pathways. Thus $\text{Pr}_2\text{Zr}_2\text{O}_7$ might be expected to be in or close to a spin glass ground state as a result of frustration and site/bond disorder. Frequency dependent AC susceptibility shows indications of glassiness for $T \leq \sim 0.3$ K (Fig. 2.13). However, low temperature magnetic specific heat C_M shows activated behavior instead of the characteristic T -linear dependence for a spin glass⁶¹ (Fig. 2.14). Strong low temperature spin fluctuations as seen by inelastic neutron scattering are also inconsistent with a conventional spin glass ground state.

2.5 Conclusion

Our comprehensive study of $\text{Pr}_2\text{Zr}_2\text{O}_7$ reveals a rather unique and complicated low temperature magnetic state. On one hand, over long time scales spins are correlated with each other according to ice rule as in the classical spin ice. On the other hand, these spins remain highly dynamical down to temperatures much lower than the interaction energy scale. There are two distinct contributions to the low temperature quantum spin dynamics: a high energy part that corresponds to splitting of the CEF ground state doublet and a low energy part that is influenced by inter-site correlations. The persistence of correlated quantum spin dynamics down to low temperatures makes $\text{Pr}_2\text{Zr}_2\text{O}_7$ of interest in the pursuit of a quantum spin liquid ground state. However, the existence of inhomogeneous doublet splitting raises the question of whether a coherent quantum ground state can occur in a seemingly inhomogeneous spin system.

One way to check whether $\text{Pr}_2\text{Zr}_2\text{O}_7$ can realize a quantum spin liquid ground state is to tune the doublet splitting through solid state chemistry. X-ray diffraction results (Fig. 2.7(f)) show that the anisotropy of the thermal ellipsoid of Pr^{3+} , a parameter that might be related to the degree of Pr^{3+} off centering, decreases as the Pr/Zr ratio increases. This means that by tuning the Pr/Zr ratio one can effectively modify the degree of doublet splitting. Thus it might be possible to get close to a homogeneous limit with minimal doublet splitting by adding more Pr, if the pyrochlore structure remains stable at the required doping level.

CHAPTER 2. QUANTUM SPIN ICE $\text{Pr}_2\text{Zr}_2\text{O}_7$

Further study in these directions will not only deepen our understanding of $\text{Pr}_2\text{Zr}_2\text{O}_7$ as a candidate material to realize quantum spin ice, but may elucidate the peculiar properties of non-Kramers frustrated spin systems where lattice degrees of freedom inevitably are closely linked to magnetism.

Chapter 3

Continuum Excitation in NiGa_2S_4

3.1 Introduction

The triangular lattice antiferromagnet is a structurally simple realization of geometrical frustration. While frustration and quantum fluctuations have the potential to suppress ordering, it has been established that the nearest neighbor spin- $\frac{1}{2}$ triangular lattice antiferromagnet enters a long range order ground state with 120° spiral structure at the absolute zero temperature.⁶² This tendency to magnetic long range order has been demonstrated in various materials that host triangular lattice antiferromagnets⁶³⁻⁷³ with finite temperature transitions into magnetic long range order. Several triangular lattice based materials however have been discovered that elude long range order.⁷⁴⁻⁷⁷ Apart from weaker interlayer interactions, interactions beyond the usual bilinear Heisenberg exchange interactions are believed to play important

roles in suppressing conventional three-sublattice ordering. For example in the spin liquid candidate triangular lattice compound κ -(BEDT-TTF)₂Cu₂(CN)₃,⁷⁴ it was suggested that charge fluctuations due to proximity to a metal insulator transition is key to the putative spin liquid ground state.

NiGa₂S₄⁷⁶ is another triangular lattice material that remains magnetically disordered at low temperatures. In this compound, Ni²⁺ ions form layers of apparently un-distorted spin-1 triangular lattices that are attached through van der Waals dipolar interactions. Consequently the magnetic inter-layer interactions are expected to be extremely weak (Fig. 3.1). DC magnetic susceptibility measurements yield a Curie-Weiss temperature $\theta_{\text{CW}} = -80(2)$ K indicating antiferromagnetic interactions with an average strength of $\tilde{J} = |3\theta_{\text{CW}}|/z/S(S+1) = 1.72(4)$ meV where an average coordination number of $z = 6$ was employed. A bifurcation between field cooled and zero field cooled susceptibility at $T^* = 8.5$ K suggests some form of low temperature spin freezing. The temperature dependence of the magnetic specific heat has no sharp anomaly down to 0.35 K but instead two broad peaks near $|\theta_{\text{CW}}|$ and T^* . The low temperature specific heat for $T < T^*$ varies as T^2 which is consistent with linearly dispersive excitations in 2-dimensions. Local magnetic susceptibility probes such as NMR and μ SR reveal critical slowing down of spin dynamics at T^* . Spin fluctuations on the MHz frequency scale however remain down to 2 K.⁷⁸⁻⁸⁰ Magnetic neutron scattering uncovered development of an incommensurate short range ordered state below T^* with a correlation length of only 6.9(8) lattice sites at 2 K.^{76,81} The

CHAPTER 3. CONTINUUM EXCITATION IN NiGa₂S₄

characteristic ordering wave vector \mathbf{q}_0 was found to be incommensurate and close to $(1/6, 1/6, 0)$, which together with photoemission spectroscopy⁸² and first principle calculation⁸³ suggested the dominant exchange interaction is antiferromagnetic between third nearest neighbors, J_3 . Weak ferromagnetic interactions, J_1 , between nearest neighbors may account for the incommensurate shift to lower \mathbf{Q} than $(1/6, 1/6, 0)$.

The $J_1 - J_3$ triangular lattice Heisenberg model, however, has been shown to develop a first order phase transition at a finite temperature where 3-fold rotation symmetry is spontaneously broken.⁸⁴ This seems to be at odds with the experimental observations for NiGa₂S₄. It was also suggested that in addition to J_1 and J_3 , a nearest neighbor biquadratic interaction of the form $-K \sum_{\langle i,j \rangle} (\mathbf{S}_i \mathbf{S}_j)^2$ might be relevant in this material and gives rise to nematic spin-correlations.⁸⁵⁻⁸⁹ In particular, it was proposed that the double peak structure in specific heat could be due to proximity to a quantum critical point that separates a spiral and a nematic ground state in the $J_1 - J_3 - K$ model. The absence of the first order transition might be related to nonmagnetic defects such as putative sulfur vacancies that might act as random fields on the C_3 bond order parameter.⁸⁹ Whether nematic correlations are significant in this material needs further investigation. One indication of nematic correlations is the rather short spin-correlation length, which would seem to require an implausibly high impurity density for a model with bilinear spin-spin interactions only.

The microscopic mechanism that induces spin disorder in NiGa₂S₄ remains unclear at this point. Probing the excitations from the exotic low temperature state might

provide useful information to resolve the mystery. In this chapter, a comprehensive study of magnetic excitations in NiGa₂S₄ by inelastic neutron scattering will be reported. A broad yet dispersive spectrum was observed, with an overall bandwidth similar to $|\theta_{CW}|$.

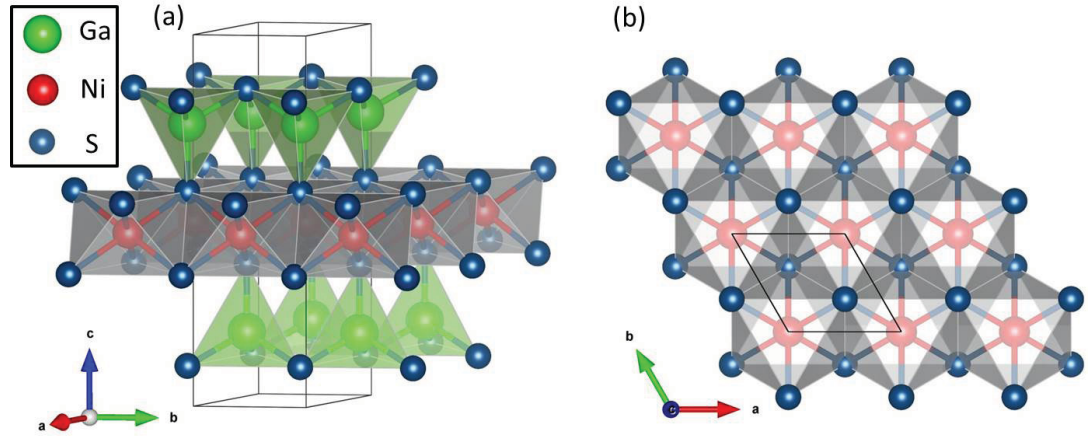


Figure 3.1: Crystal structure of NiGa₂S₄. (a) NiGa₂S₄ consists of a central layer of NiS₆ sandwiched between two layers of GaS₄. (b) The diffraction data indicate magnetic Ni²⁺ ions form perfect triangular lattices.

3.2 Experimental Techniques

19 single crystals of NiGa₂S₄ with total mass ~ 1 g were co-aligned (with mosaic $\sim 1.5^\circ$) in the $(HK0)$ plane for the measurement (Fig. 3.2). The experiment was carried out on the MACS instrument⁵⁶ at the NIST Center for Neutron Research. A final neutron energy of $E_f = 3.6$ meV (with energy resolution at the elastic line $\delta E = 0.20$ meV⁵⁶) was used for measurements with energy transfer $\hbar\omega \leq 4.5$ meV,

while $E_f = 5$ meV ($\delta E = 0.39$ meV⁵⁶) was employed for measurement with $\hbar\omega \geq 4.5$ meV. Comparison of the scattering intensity at $E = 4.5$ meV measured under both configurations showed that the neutron count rate with $E_f = 5$ meV is 2.0(1) as large as that with $E_f = 3.6$ meV, thus a factor of 0.5 was applied to neutron scattering intensities measured with $E_f = 5$ meV. To subtract out the contributions in scattering from the aluminum sample holder and the cryostat, an aluminum sample with similar mass to the sample holder as well as the empty cryostat were measured separately at all experimental settings for background subtraction. Thus the data presented below is mainly due to scattering from NiGa₂S₄. Since there was no filter in the incident beam, monitor normalized data were corrected by an energy dependent factor to correct for the contribution to the monitor count rate from $\lambda/2$ neutrons. Considering from the 6-fold symmetry of NiGa₂S₄, constant energy slices collected for an 180 degree range of sample rotation were folded into a sextant for better statistics.

3.3 Experimental Results

The development of short range magnetic order was probed by elastic scattering maps measured at 2 K which show the appearance of magnetic superlattice peaks (Fig. 3.3(d)). High temperature measurements at 20 K were used to subtract out nuclear contributions. A cut along the $\Gamma - K$ direction through the peak shows the detailed line shape in Fig. 3.3(c). The peak is well described by a Gaussian

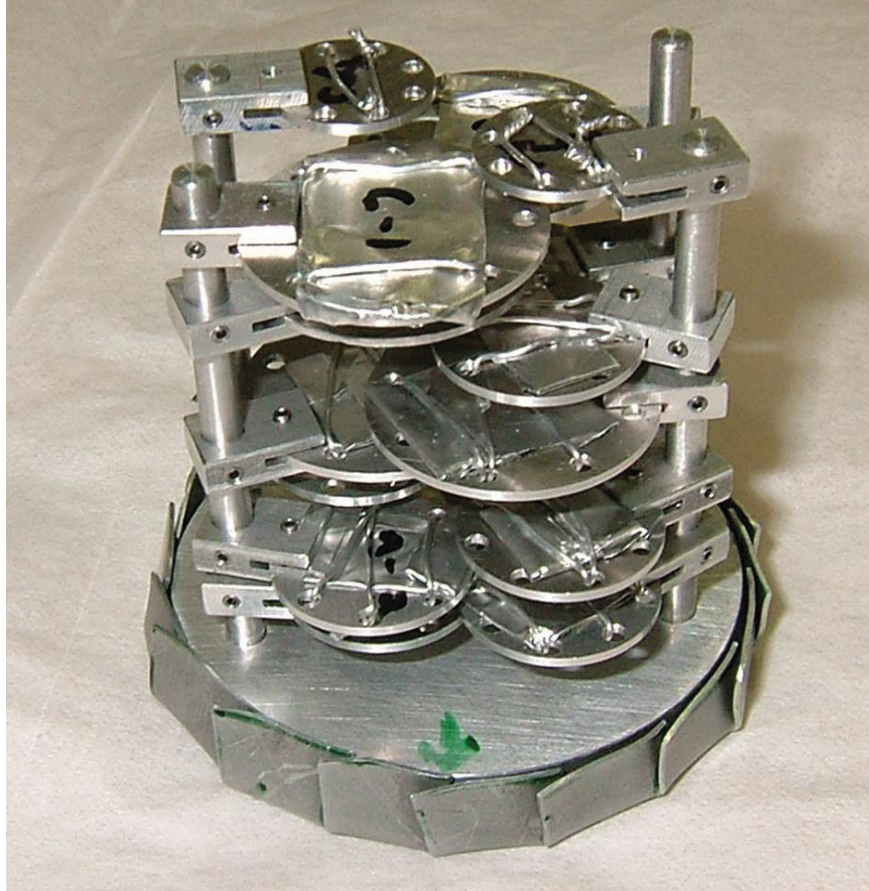


Figure 3.2: Assembly of 19 single crystalline NiGa_2S_4 (~ 1 g) co-aligned in $(HK0)$ plane.

CHAPTER 3. CONTINUUM EXCITATION IN NiGa₂S₄

centered at an incommensurate position of $\mathbf{q}_0 = (0.155(1), 0.155(1), 0)$, consistent with previous neutron measurements on this material.^{76,81} The correlation length derived from the data is $2/\text{FWHM}$ where FWHM is the full width at half maximum of the peak, and yielded a rather short correlation length of $\xi = 17.2(2)$ Å, which is not inconsistent with $\xi = 26(3)$ Å determined from previous measurements on this material.⁸¹ The difference could be due to the relatively coarser energy resolution in the current experiment.

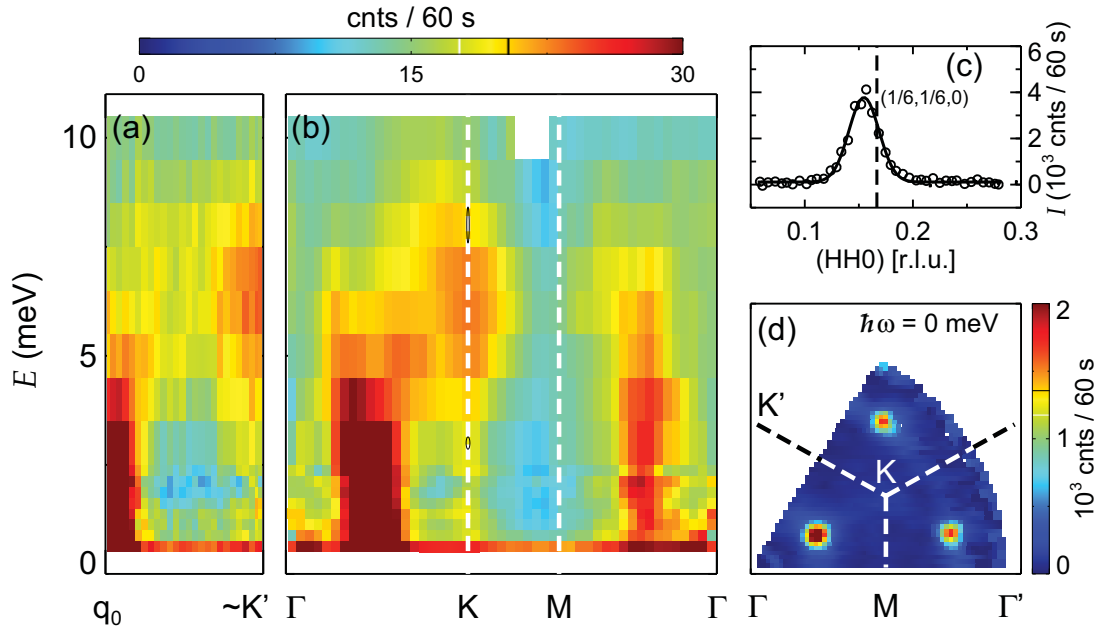


Figure 3.3: Neutron spectrum of NiGa₂S₄ measured at 2 K along different directions. (a) Spectrum originating from the critical wave vector \mathbf{q}_0 perpendicular to $\Gamma - K$ direction. (b) Spectrum along three high symmetry directions of the reciprocal lattice: $\Gamma - K$, $K - M$, and $M - \Gamma$. Black ellipses show representative instrumental resolutions. (c) Elastic scan along $\Gamma - K$ direction in frame (d). Solid line shows a Gaussian fit to the data. The vertical dashed line shows the commensurate position of $(1/6, 1/6, 0)$. (d) Elastic scattering map measured at 2 K. Measurement at 20 K were used to subtract out nuclear contributions. Dashed lines show Brillouin zone boundaries.

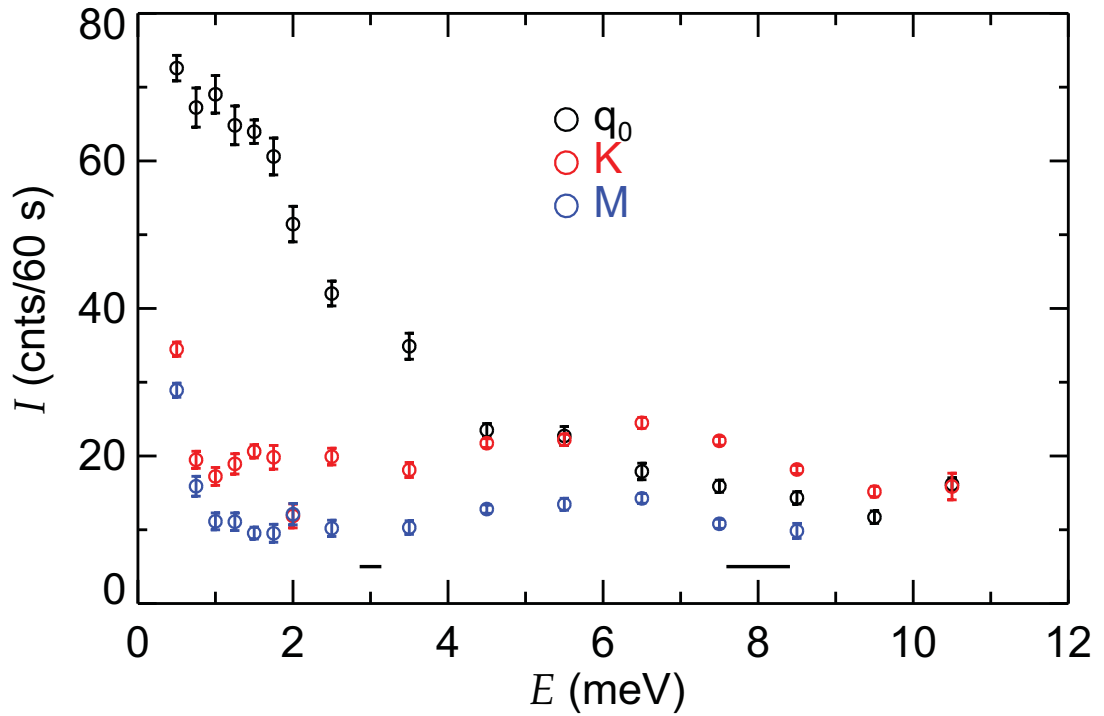


Figure 3.4: Neutron spectrum of NiGa₂S₄ at q_0 , K, and M points obtained by constant q cuts through data presented in Fig. 3.3(b). Black bars at $E = 3$ meV and $E = 8$ meV show the corresponding energy resolution.

CHAPTER 3. CONTINUUM EXCITATION IN NiGa₂S₄

The spectrum of magnetic scattering from NiGa₂S₄ was obtained by measuring constant energy slices at 2 K with energy transfer $\hbar\omega$ from 0.5 meV to 10.5 meV in steps of 0.25 meV for $\hbar\omega < 2.5$ meV and 1 meV at higher energy transfer. Representative slices are shown in Fig. 3.5. At low energies, the inelastic scattering intensity maps take the form of broad peaks centered around equivalent \mathbf{q}_0 positions. A broad and weak intensity maximum is also visible at the K point. With increasing energy transfer, $\hbar\omega$, the relative intensity ratio between K and \mathbf{q}_0 increases, and becomes similar for $\hbar\omega \sim 4.5$ meV. This is consistent with a dominant third neighbor interaction J_3 . In fact, if only J_3 was present the unit cell quadruples and $(1/6, 1/6, 0)$, which is close to \mathbf{q}_0 , and K are equivalent locations in the Brillouin zone. At even higher energy transfer, the intensity at K actually becomes dominant over that at \mathbf{q}_0 , and the top of the band is reached there for $\hbar\omega \sim 10$ meV.

A slice through the three dimensional data set that contains the energy axis and select directions in momentum space, rather than producing sharp dispersion relations as expected for conventional spin wave excitations, produces ridges that are broad in both E and \mathbf{q} (Fig. 3.3(a) and (b)). Fig. 3.3(b) shows the spectrum along three high symmetry directions of the Brillouin zone. A strong intensity ridge stems from \mathbf{q}_0 , and disperses along the $\Gamma - K$ direction. Softening is apparent at the K point, but consistent with the presence of nearest neighbor interaction J_1 the gap does not close as it does at \mathbf{q}_0 . The M point is a quiet position with minimal magnetic scattering intensity. Along the $M - \Gamma$ direction, there is another intensity ridge near the position

where \mathbf{q}_0 is closest to the $M - \Gamma$ axis. An energy-momentum slice through the data starting from \mathbf{q}_0 and extending along the direction perpendicular to $\Gamma - K$ is shown in Fig. 3.3(a).

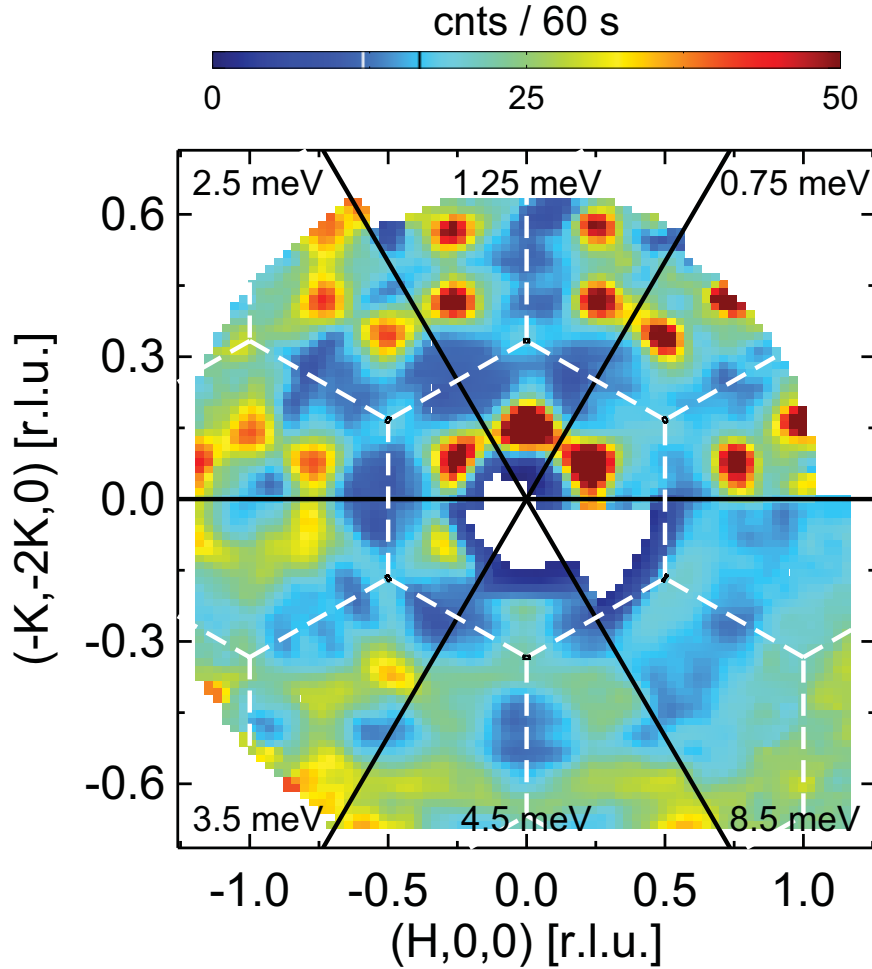


Figure 3.5: Representative constant energy slices of NiGa₂S₄ measured at 2 K. Black circles at the K points show calculations of instrumental momentum space resolutions.

The thermal evolution of the magnetic excitations provides another essential piece of information to understand the nature of magnetism in NiGa₂S₄. This was probed

CHAPTER 3. CONTINUUM EXCITATION IN NIGAs₂S₄

by measuring temperature dependent constant $\hbar\omega = 1.5$ meV slices between 1.5 K and 130 K. Considering that the Curie Weiss temperature $|\theta_{\text{CW}}| \sim 80$ K sets the temperature scale below which significant spin correlations are expected to develop, it was assumed that the inelastic scattering intensity measured at 130 K is dominated by phonon scattering. Since the temperature dependence of the one-phonon scattering at different temperatures is governed by the Bose population factor,⁴⁷ the measurement at 130 K can then be used to subtract the phonon scattering contribution from the lower temperature measurements as follows:

$$\tilde{I}(T) = I(T) - \frac{1 - e^{-\hbar\omega_0/(k_{\text{B}}T_0)}}{1 - e^{-\hbar\omega_0/(k_{\text{B}}T)}} I(T_0). \quad (3.1)$$

Here $I(T)$ and $\tilde{I}(T)$ are intensities before and after phonon subtraction at temperature T , respectively, and $\hbar\omega_0 = 1.5$ meV, $T_0 = 130$ K, and k_{B} is the Boltzmann constant. The resultant maps of $\tilde{I}(T)$ are shown in Fig. 3.6(a). The broad intensity peaks at \mathbf{q}_0 sharpens upon cooling which provides evidence for the development of correlated spin dynamics. The short range dynamical correlation persists up to at least $|\theta_{\text{CW}}|$ as manifested by a still relatively well defined peak at \mathbf{q}_0 for temperature as high as 90 K.

To quantify temperature dependent dynamic correlations, the slices in Fig. 3.6(a) were fit to a phenomenological scattering function based on a result from the random

phase approximation (RPA).⁵⁹

$$\tilde{I}(T) = \frac{1}{1 - e^{-E_0/(k_B T)}} \frac{C_0}{1 - \chi_0 J(\mathbf{q})} F(|\mathbf{q}|)^2. \quad (3.2)$$

Here $J(\mathbf{q}) = J_1 \sum_{\langle 0j \rangle} e^{-\mathbf{q} \cdot (\mathbf{r}_j - \mathbf{r}_0)} + J_3 \sum_{\langle\langle 0j \rangle\rangle} e^{-\mathbf{q} \cdot (\mathbf{r}_j - \mathbf{r}_0)}$ is the lattice Fourier transform of exchange constants. $\langle \rangle$ and $\langle\langle \rangle\rangle$ represent restricted summation over nearest neighbors and third nearest neighbors. We used $J_3 = -2.8$ meV and $J_1 = -0.35J_3$ which were previously determined based on the Curie-Weiss constant and the critical wave vector.⁸¹ $F(|\mathbf{q}|)$ is the magnetic form factor for Ni²⁺. The best fits are shown in Fig. 3.6(b). It is apparent from Fig. 3.6 that Eq. 3.2 captures the salient features of the experimental data: a strong peak around \mathbf{q}_0 and a weak response around the K point. The parameters extracted from the fit C_0 and χ_0 , are shown as a function of temperature in Fig. 3.7. Both C_0 and χ_0 increase monotonically with decreasing temperatures. If we take the RPA analogy a bit further and assume an isotropic Curie response at the single ion level, χ_0 is expected to follow a $1/T$ dependence. The experimental χ_0 has a rather weak T -dependence in the temperature range probed and appears to saturate to a finite value at low temperatures. This could be considered as a reflection of the strong correlations from frustration that cannot be captured in a RPA description. The non-diverging nature of χ_0 as $T \rightarrow 0$ could also be associated with the easy plane magnetic anisotropy, which is present in this

CHAPTER 3. CONTINUUM EXCITATION IN NiGa₂S₄

material.⁷⁷

I shall now discuss possible origins of the observed broad spectrum of excitations that are observed. One possibility is that the finite correlation length of the underlying magnetic order implies that \mathbf{q} is no longer a good quantum number for excited states so a continuous spectrum is observed for fixed momentum transfer. In this scenario, the long wave length low energy spin wave modes with the highest group velocity near \mathbf{q}_0 are most severely broadened and could be expected to produce a ridge of intensities centered around \mathbf{q}_0 as seen in the experiment. From the 0 K limit of the magnetic specific heat and its T^2 dependence below T^* , it was suggested that the low energy excitations ($\hbar\omega < k_B T^*$) in NiGa₂S₄ are linearly dispersive modes that have a coherence length of at least 500 lattice sites.³ To account for these inferred coherent modes, it was proposed that they could be the Halperin-Saslow hydrodynamic modes in the background of the short range ordered frozen moments.⁹⁰ It seems that the frozen short range order scenario is able to account for both the broad intensity ridges observed in inelastic neutron scattering and the low temperature heat capacity. However, in this scenario the spin wave modes near the zone boundary, where the group velocity vanishes, are not expected to be broadened by the finite correlation length in the ground state, which is at odds with the experimental observation. Detailed comparison between the experimental neutron spectrum with calculations such as the spin wave spectrum from a short range order state could help to clarify this situation.

Another more exotic scenario is that the continuum neutron spectrum is due to

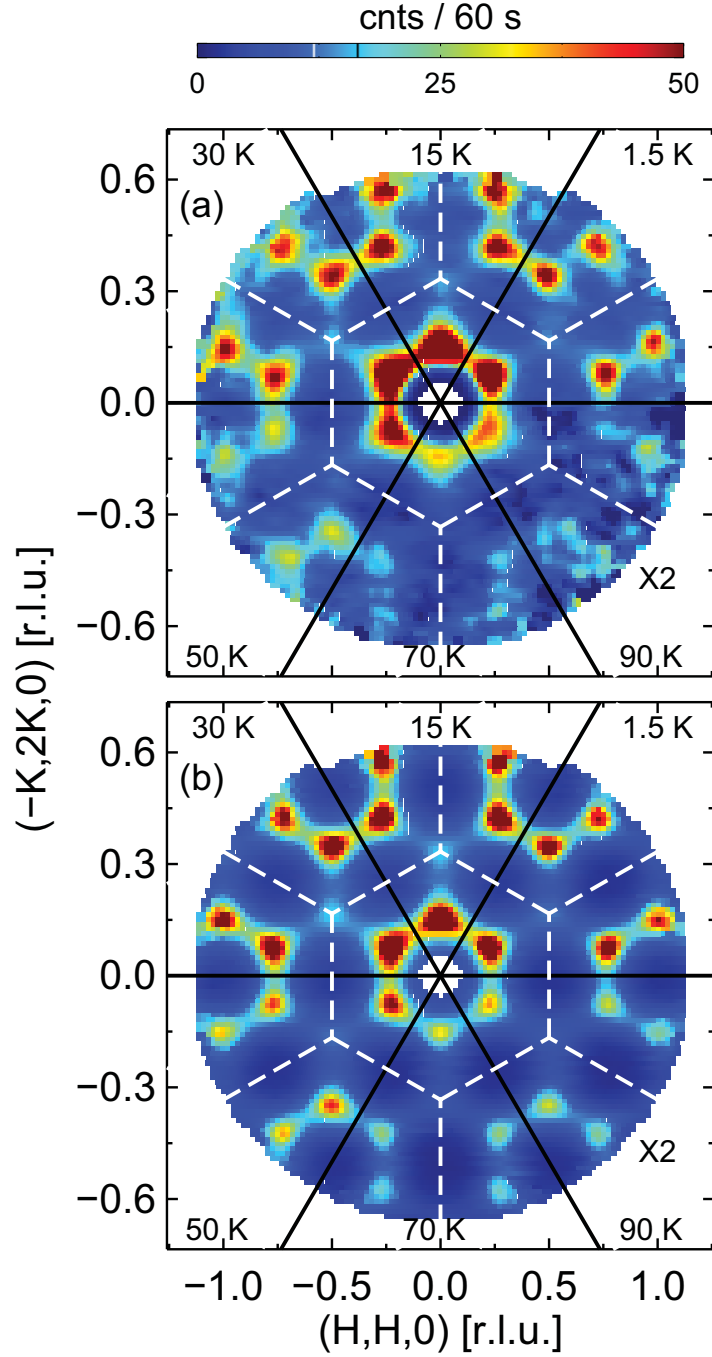


Figure 3.6: Thermal evolution of dynamical spin correlations in NiGa₂S₄. (a) Constant energy slices measured with $E = 1.5 \text{ meV}$ at different temperatures. Intensity at 90 K were scaled by a factor of 2 for better visualization. (b) Fitting results of experimental data in frame (a) as described in the main text.

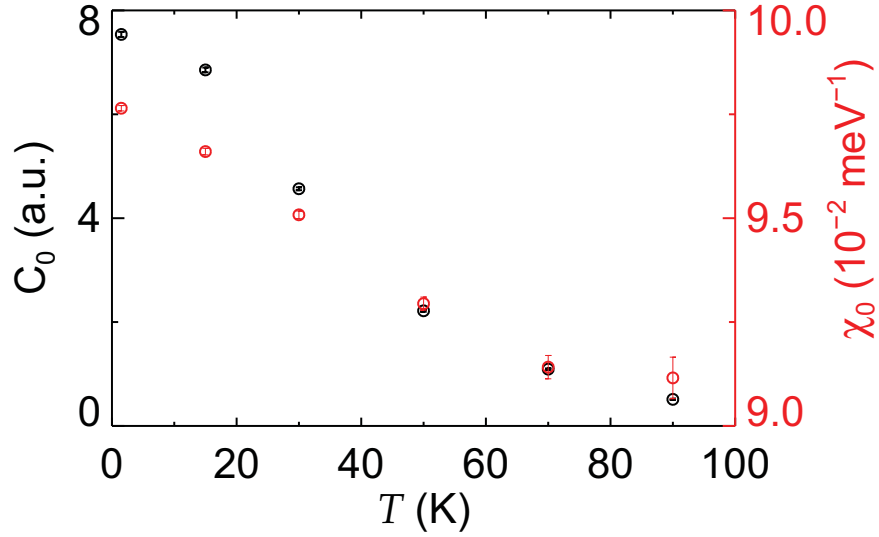


Figure 3.7: Temperature dependence of parameters C_0 and χ_0 as extracted from fitting shown in Fig. 3.6.

multi-particle scattering. The coherent modes seen in the specific heat could then be some kind of exotic quasiparticles that can not be singly excited by neutrons, such as excitations from a nematic ground state⁹¹ or a spin-1/2 spinon in a quantum spin liquid. However, if the scattering involves only a small number of quasiparticles, there should be a sharp lower bound to the continuum, as for the 2 spinon continuum in the 1D antiferromagnetic spin-1/2 chain.^{92,93} As shown in Fig. 3.4, the energy spectrum for NiGa₂S₄ is rather broad with no sharp edges. It was recently proposed in the case of spin-1/2 kagome lattice antiferromagnet that the lower bound of the 2 spinon continuum could be dramatically blurred due to couplings between spinons and flat bands of topological vison excitations, which act as momentum sinks.⁹⁴ Whether a similar mechanism is relevant to NiGa₂S₄ calls for further theoretical studies.

3.4 Conclusion

In conclusion, we have carried out comprehensive measurements of magnetic excitations in NiGa₂S₄ by inelastic neutron scattering. The neutron spectrum was found to be broad in \mathbf{q} and E throughout the Brillouin zone and bounded in energy by ~ 10 meV. The temperature dependence of dynamic correlations as reflected by the \mathbf{Q} -dependence of inelastic scattering measured at $E = 1.5$ meV can be semi-quantitatively described by expressions associated with the Random Phase Approximation, and showed dynamical correlations persist up to temperatures of at least $|\theta_{CW}|$. These results provide a crucial piece of information to test any theoretical proposal to explain the magnetically disorder ground state in this crystalline triangular lattice spin-1 antiferromagnet.

Chapter 4

Disorder from Order among

ANNNI Spin Chains in SrHo_2O_4

4.1 Introduction

An interesting byproduct of the intense pursuit of materials that can host spin-liquids has been the discovery of nominally pure crystalline solids with frozen short range correlated magnetism.^{3,95-98} In some cases quenched disorder simply alters the ground state and defines a short spin correlation length, but for materials such as two dimensional NiGa_2S_4 studied in the previous chapter where the spin correlation length is much shorter than a plausible impurity spacing such explanations seem untenable. In this chapter, we propose spin disorder in frustrated low dimensional magnets can result from a complex thermalization process in the absence of quenched disorder.

CHAPTER 4. DISORDER FROM ORDER AMONG ANNNI SPIN CHAINS IN SrHo_2O_4

Comprising two types of Ising spin chains with nearest neighbor (J_1) and next nearest neighbor (J_2) interactions (ANNNI models⁸) organized on a honeycomb-like lattice, SrHo_2O_4 will be shown to provide a striking example.⁹⁹⁻¹⁰⁴ We show the chains straddle the $J_2/J_1 = 1/2$ critical point so that “red” chains have a ground state that doubles the unit cell ($\uparrow\downarrow\uparrow\downarrow$) while the ground state for “blue” chains is ($\uparrow\uparrow\downarrow\downarrow$). While red chains develop 3D LRO, blue chains in the very same crystal cease further equilibration towards their more complex ground state when the red spins saturate in an ordered state.

Before going into the experimental results, I will first introduce the 1D ANNNI model which forms the foundation for understanding the low temperature magnetism in SrHo_2O_4 .

4.2 1 Dimensional ANNNI Model

1D ANNNI model is one of the simplest models that host modulated spin correlations.⁸ The Hamiltonian takes the form of

$$\mathcal{H}_{\text{ANNNI}} = - \sum_i (J_1 S_i S_{i+1} + J_2 S_i S_{i+2}) \quad (4.1)$$

where $S = \pm 1$. It describes a linear chain of Ising spins with nearest neighbor interaction J_1 and next nearest neighbor interaction J_2 . This linear chain is also identical to a zig-zag ladder with inter-leg interaction J_1 and intra-leg interaction J_2 ,

CHAPTER 4. DISORDER FROM ORDER AMONG ANNNI SPIN CHAINS IN SrHO_2O_4

as shown in Fig. 4.1. This mapping between a linear chain and a zig-zag ladder will be important in SrHO_2O_4 .

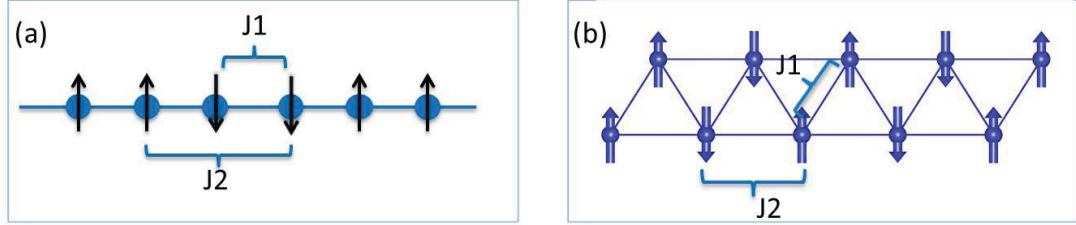


Figure 4.1: (a) A linear spin chain with nearest neighbor interaction J_1 and next nearest neighbor interaction J_2 as described by the 1D ANNNI model. (b) Equivalently the 1D ANNNI model also describes a zig-zag spin ladder with inter-leg interaction J_1 and intra-leg interaction J_2 .

Only the Ferromagnetic $J_1 > 0$ case needs to be considered since the corresponding results for the antiferromagnetic $J_1 < 0$ case can readily be obtained by redefining the spin direction on every other site: $S'_{2i+1} = -S_{2i+1}$. When $J_2 < 0$, $J_1/2$ compete as they favor different spin configurations. It is easy to see that there are two different ground states depending on the ratio of J_2/J_1 :¹⁰⁵ a ferromagnetic state ($\uparrow\uparrow\uparrow$) for $J_2/J_1 > -1/2$, while a double Néel state ($\uparrow\uparrow\downarrow\downarrow$) is the ground state for $J_2/J_1 < -1/2$. Magnetic long range order can be obtained only at the absolute zero temperature since $\mathcal{H}_{\text{ANNNI}}$ belongs to the 1D Ising universality.

By introducing a new variable $\sigma_i = S_i S_{i+1}$,¹⁰⁶ $\mathcal{H}_{\text{ANNNI}}$ can be mapped to the familiar Ising model in a magnetic field:

$$\mathcal{H}'_{\text{ANNNI}} = - \sum_i (J_1 \sigma_i + J_2 \sigma_i \sigma_{i+1}) \quad (4.2)$$

CHAPTER 4. DISORDER FROM ORDER AMONG ANNNI SPIN CHAINS IN SRHO_2O_4

Thus the finite temperature properties of $\mathcal{H}_{\text{ANNNI}}$ can be calculated analytically by transfer matrix technique through $\mathcal{H}'_{\text{ANNNI}}$. The eigenvalues of the relevant transfer matrices are:⁸

$$\lambda_{1/2} = e^{\kappa_2} \cosh \kappa_1 \pm (e^{2\kappa_2} \sinh^2 \kappa_1 + e^{-2\kappa_2})^{1/2} \quad (4.3)$$

$$\tilde{\lambda}_{1/2} = e^{\kappa_2} \sinh \kappa_1 \pm (e^{2\kappa_2} \cosh^2 \kappa_1 - e^{-2\kappa_2})^{1/2} \quad (4.4)$$

where $\kappa_{1/2} = J_{1/2}/k_{\text{B}}T$. The two point spin correlation function $G(r)$, which describes many aspects of the magnetic state, can be calculated as follows:

$$G(r) = \begin{cases} a \exp[-r \ln(\lambda_1/\tilde{\lambda}_1)] + (1-a) \exp[-r \ln(\lambda_1/\tilde{\lambda}_2)] & , \text{ for } \tilde{\lambda}_1 \neq \tilde{\lambda}_2 \\ \exp[-r \ln(\lambda_1/\tilde{\lambda})](1 + br/\tilde{\lambda}) & , \text{ for } \tilde{\lambda}_1 = \tilde{\lambda}_2 = \tilde{\lambda} \end{cases} \quad (4.5)$$

where

$$a = 1/2 \{1 + e^{2\kappa_2} \sinh \kappa_1 \cosh \kappa_1 [(e^{2\kappa_2} \sinh^2 \kappa_1 + e^{-2\kappa_2}) \times (e^{2\kappa_2} \cosh^2 \kappa_1 - e^{-2\kappa_2})]^{-1/2}\} \quad (4.6)$$

$$b = e^{2\kappa_2} \sinh \kappa_1 \cosh \kappa_1 (e^{2\kappa_2} \sinh^2 \kappa_1 + e^{-2\kappa_2})^{-1/2} \quad (4.7)$$

CHAPTER 4. DISORDER FROM ORDER AMONG ANNNI SPIN CHAINS IN SRHO_2O_4

When $\cosh \kappa_1 > e^{-2\kappa_2}$ both $\lambda_{1/2}$ and $\tilde{\lambda}_{1/2}$ are real and $G(r)$ is a pure exponential decay with correlation length ξ

$$\xi = [\ln(\lambda_1/\tilde{\lambda}_1)]^{-1} \quad (4.8)$$

For $\cosh \kappa_1 < e^{-2\kappa_2}$, $\tilde{\lambda}_{1/2}$ is complex so that $G(r)$ is an exponential envelope function controlling the amplitude of an oscillatory function $\cos(qr)$. q is a temperature dependent wave vector given by

$$q = \arctan(\text{Im } \tilde{\lambda}_1 / \text{Re } \tilde{\lambda}_1) \quad (4.9)$$

The analytical results presented above are illustrated in Fig. 4.2.⁸ For $\kappa \equiv -J_2/J_1 > 0.5$, the modulation wave vector q changes continuously with temperature approaching the ground state value of $\pi/2$ as temperature approaches 0 K. For $\kappa < 0.5$ on the other hand, $G(r)$ is modulated at high temperature, and becomes a non-oscillatory exponential decay below a disorder line defined by $\cosh \kappa_1 = e^{-2\kappa_2}$.

The analytical results for $G(r)$ allow a comprehensive comparison between theoretical and experimental results. Neutron scattering directly measures $\tilde{G}(q)$, the Fourier transform of $G(r)$, and the magnetic susceptibility χ can be readily calculated from $G(r)$ through

$$\chi \equiv \lim_{h \rightarrow 0} \frac{\partial \langle M \sum_i S_i \rangle}{\partial h} = NM^2 \beta \tilde{G}(q=0) \quad (4.10)$$

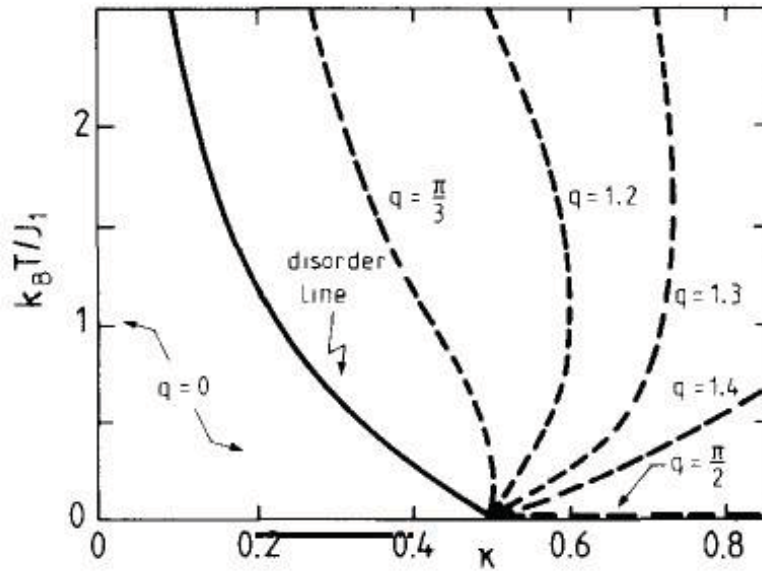


Figure 4.2: Contours of constant modulation q for 1D ANNNI model in $(k_B T / J_1, \kappa = -J_2 / J_1)$ plane. The solid line is the disorder line below which $G(r)$ is a pure exponential function.⁸

where N is the number of sites in the spin chain, M is the dipole moment of each spin, h is the magnetic field, and $\beta = 1/k_{\text{B}}T$. The comparisons of both $\tilde{G}(q)$ and χ will be employed below to understand the correlated magnetism of SrHo_2O_4 .

4.3 Experimental Results

SrHo_2O_4 single crystals were synthesized by the floating zone technique at the Institute for Quantum Matter. Elastic neutron scattering (ENS) maps down to 1.5 K were acquired on MACS⁵⁶ at NIST with $E_f = 5$ meV neutrons with a room temperature Be filter in the scattered beam. A 4.3 g single crystal was mounted for consecutive experiments in the $(HK0)$ and $(0KL)$ planes. Single crystal elastic neutron scattering down to 0.28 K was carried out on HB-1A at the HFIR of ORNL. 0.34 g and 0.19 g crystals cut to the shape of small cubes to reduce effect from absorption were used for measurements in the $(0KL)$ and $(H0L)$ planes respectively.

4.3.1 Single Ion Magnetic Anisotropy

SrHo_2O_4 crystallizes in space group $Pnam$ ⁹⁹ with two inequivalent Ho sites (Fig. 4.3(a)). Both are Wyckoff $4c$ sites with mirror planes perpendicular to the \mathbf{c} axis wherein Ho is surrounded by 6 oxygen atoms forming a distorted octahedron. The magnetic lattice consists of zig-zag ladders which extend along \mathbf{c} and form a honeycomb-like pattern in the \mathbf{ab} plane (Fig. 4.3(b)).

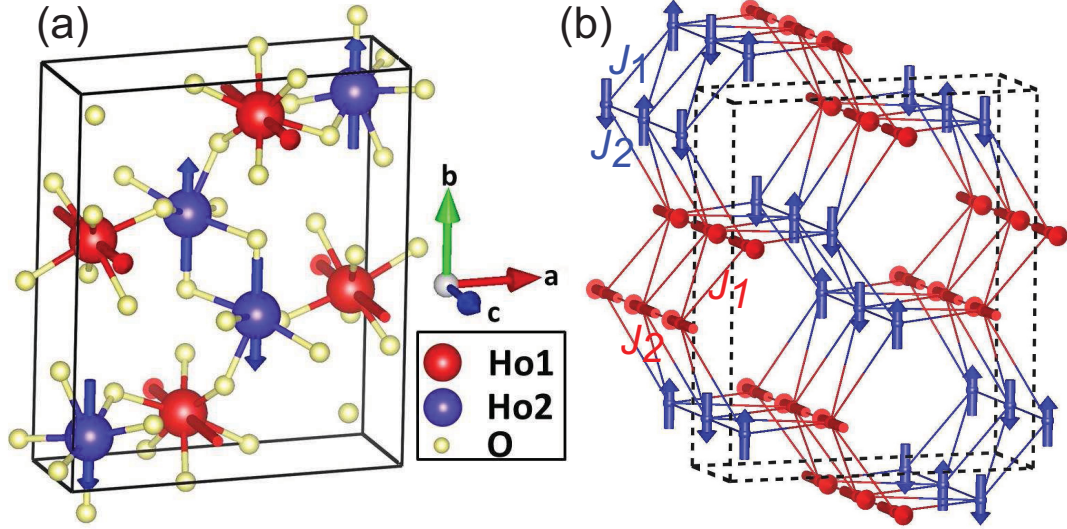


Figure 4.3: (a) Crystallographic unit cell of SrHo_2O_4 . Sr atoms were omitted for clarity. Red and Blue spheres show two distinct Ho sites, and the corresponding arrows show the Ising spin directions. (b) Magnetic lattice formed by Ho and a schematic representation of the spin structure determined by neutron diffraction.⁹

Indicating the Ising character of SrHo_2O_4 , the magnetic susceptibility χ , approximated by M/H , is shown in Fig. 4.4(a). χ_b and χ_c are found to be an order of magnitude larger than χ_a . In the anisotropic environment of a solid, the $J = 8$ multiplet of Ho^{3+} is split into multiple levels resulting in the anisotropic susceptibility.⁵⁹ The C_s point group symmetry of the Ho^{3+} site implies an easy magnetic axis either along **c** or within the **ab** plane. To gain more insight into the magnetic anisotropy a CEF calculation based on the point charge approximation⁴⁸ was carried out, and the level schemes for the two different sites are shown in Fig. 4.11. Calculations of single ion magnetic susceptibility based on these level schemes show that red Ho1 (blue Ho2) sites have an Ising doublet ground state with easy axis along **c** (b), as

shown in Fig. 4.6. We thus infer the T -dependent susceptibility for fields along \mathbf{c} and \mathbf{b} are due to red and blue sites respectively. For blue sites a finite moment along \mathbf{a} is allowed by symmetry, however, since χ_a is minimal it will be neglected.

4.3.2 Neutron Scattering from the Short Range Ordered State

The broad peaks for $T \approx 4$ K in M/H (Fig. 4.4(a)) are indicative of antiferromagnetic short range order.⁹⁹⁻¹⁰¹ For a direct view of these correlations, Fig. 4.7(a)-(d) show elastic neutrons scattering intensity maps covering the $(HK0)$ and $(0KL)$ reciprocal lattice planes. These show quasi-1D correlations along the \mathbf{c} -axis consistent with previous data.^{100,103} The modulation in the $(HK0)$ plane forms of a checkerboard-like structure (Fig. 4.7(a) and (c)). The maxima correspond to the inter-leg distances of zig-zag spin ladders, indicating intra-ladder correlations. The scattering in the $(HK0)$ plane can be unambiguously assigned to red ladders because there is no decrease in intensity for $\mathbf{q} \parallel (0K0)$ which would be the case for easy \mathbf{b} -axis blue sites due to the polarization factor in the magnetic neutron scattering cross section.⁴⁷ The fact that this scattering occurs for $\mathbf{q}_c = 0$ but vanishes near $\mathbf{q} = 0$ indicates an antiferromagnetic structure that is not modulated along \mathbf{c} as depicted for the red spin ladders in Fig. 4.3(b). The $(0KL)$ intensity map reveals another type of correlations with $\mathbf{q}_c \sim 0.5\mathbf{c}^*$, where $\mathbf{c}^* \equiv \frac{2\pi}{c}$. An analogous polarization argument shows this scat-

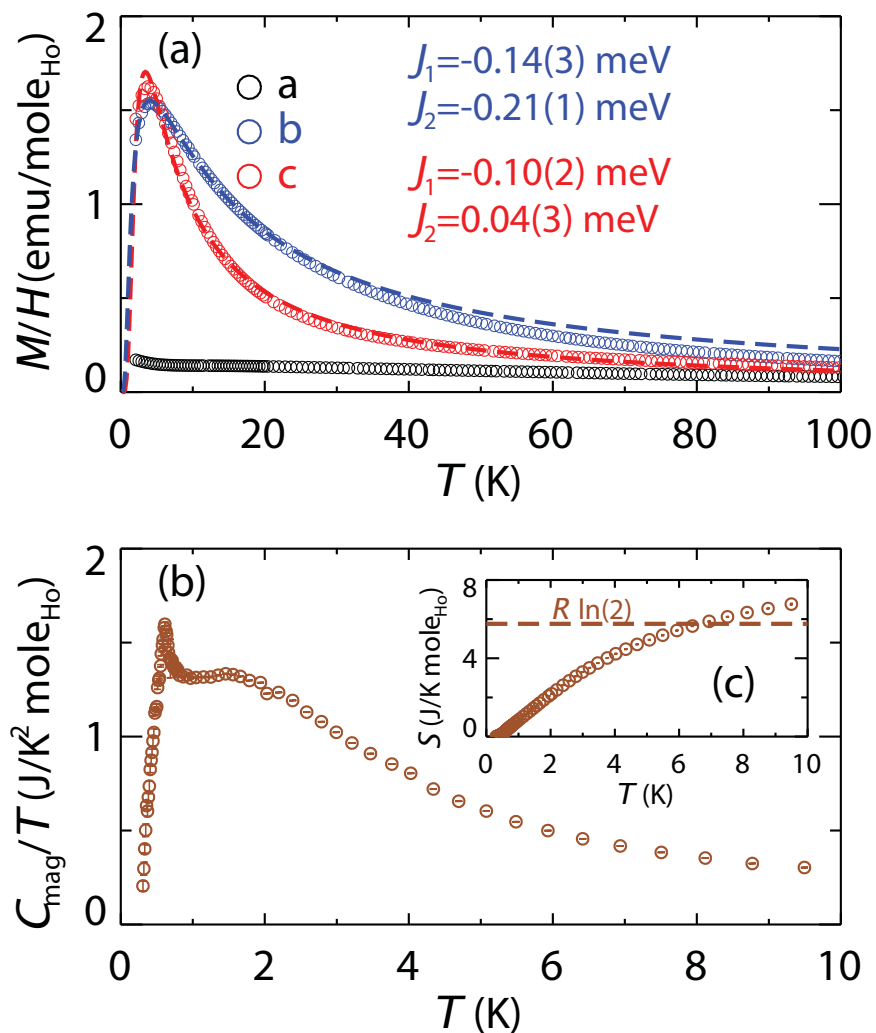


Figure 4.4: (a) Magnetic susceptibility of SrHo_2O_4 along three axes measured under 200 Oe. Dashed lines show fits to $J_1 - J_2$ Ising models. (b) Magnetic heat capacity over T versus T . (c) shows the entropy versus T . The dashed line shows the entropy of an Ising doublet.⁹



Figure 4.5: CEF level schemes for Ho1 and Ho2 calculated with point charge approximation. Thick and thin lines represent doublets and singlets. Both sites are found to have a magnetic doublet ground state.

tering arises from blue sites. The intensity maximum near $\mathbf{q}_c \sim 0.5\mathbf{c}^*$ indicates spins displaced by \mathbf{c} are anti-parallel (blue spins in Fig. 4.3(b)). The correlation lengths were estimated by $2/(\text{FWHM}_{\text{exp}}^2 - \text{FWHM}_{\text{reso}}^2)^{-\frac{1}{2}}$, where FWHM_{exp} , $\text{FWHM}_{\text{reso}}$ are experimental and instrumental full width at half maximum in \AA^{-1} . The correlation lengths along \mathbf{c} at $T = 1.5$ K were found to be indistinguishable at $13.3(3)\text{\AA}$ and $13.6(3)\text{\AA}$ for red and blue ladders respectively.

4.3.3 Zig-Zag Spin Ladders and the ANNNI Model

The minimal model of SrHo_2O_4 is a collection of two types of independent Ising zig-zag spin ladders with inter-leg interaction J_1 and intra-leg interaction J_2 . This can be described by the exactly solvable 1D ANNNI model that was introduced in Sec. 4.2. Dipolar interactions between NN spins in SrHo_2O_4 are estimated to be of order 0.1 meV, which indicates significant longer range interactions. The ANNNI

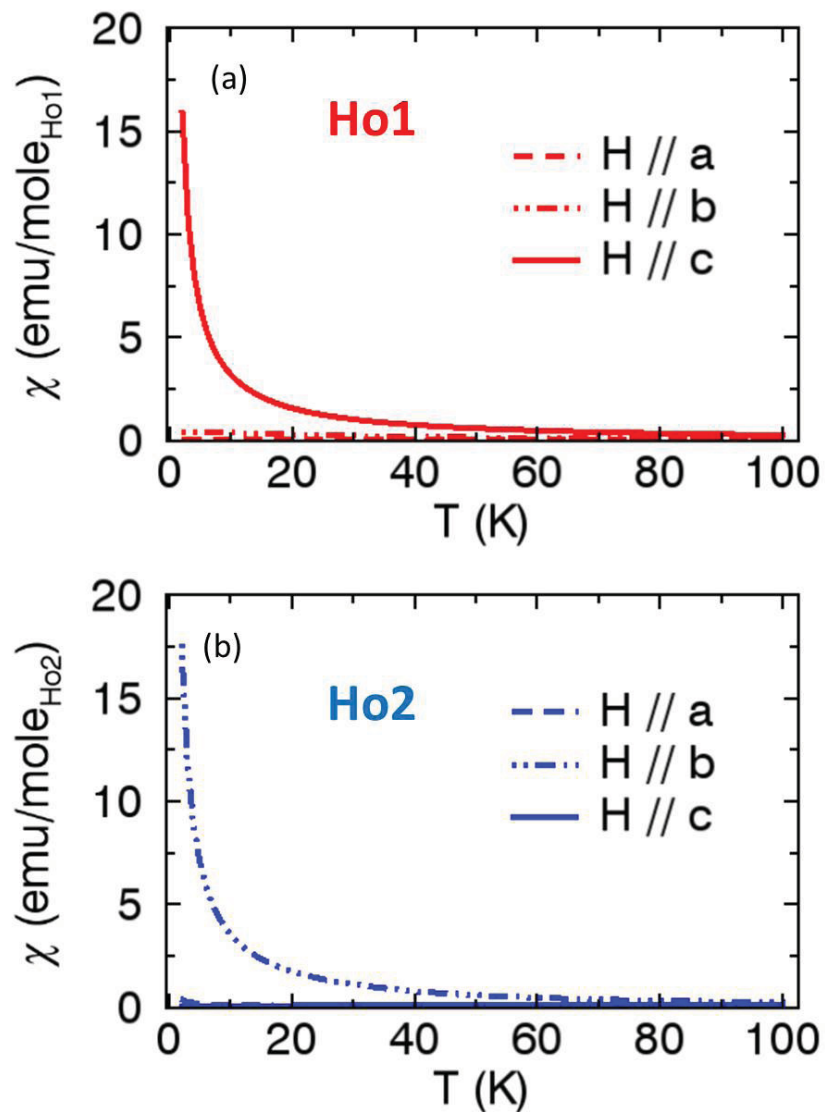


Figure 4.6: Magnetic susceptibility along three crystalline axes calculated based the point charge model CEF level scheme for (a)Ho1 and (b)Ho2. Ho1 is found to have an Ising doublet ground state along **c** while Ho2 has an Ising doublet along **b**.

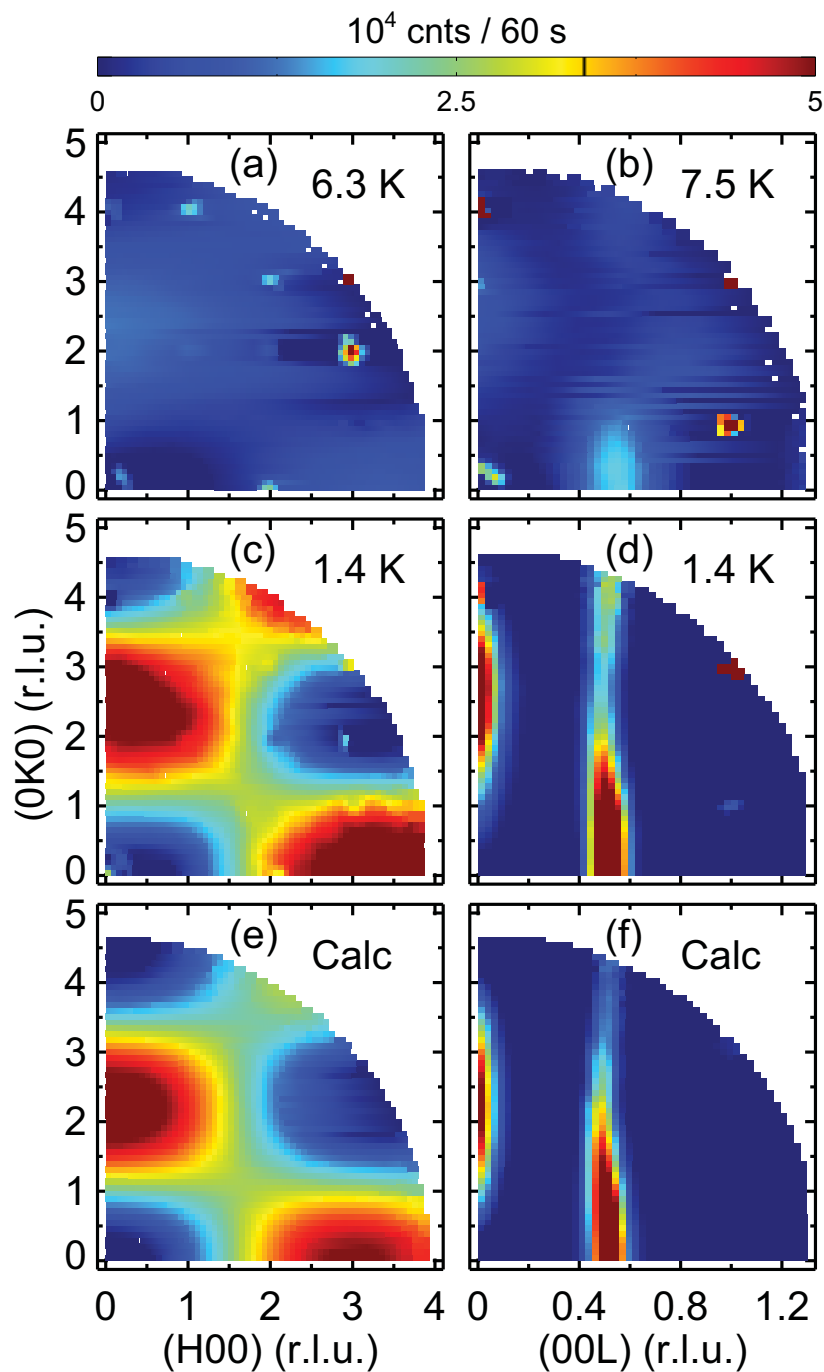


Figure 4.7: T -dependent elastic magnetic neutron scattering from the SRO of SrHo_2O_4 . (a)(c) show measurements in the $(HK0)$ plane while (b)(d) are from the $(0KL)$ plane. Measurements at 50 K were subtracted to eliminate nuclear scattering. (e) and (f) show $J_1 - J_2$ model calculations at 1.4 K with exchange constants determined from Fig. 4.2(a).⁹

CHAPTER 4. DISORDER FROM ORDER AMONG ANNNI SPIN CHAINS IN SrHo_2O_4

model should thus be considered as a minimal effective model for SrHo_2O_4 .

To determine the exchange constants we fit the anisotropic susceptibility to the analytical ANNNI susceptibility. The uniform magnetic susceptibility χ is calculated by Eq. 4.10. The fits were restricted to data points with $T \leq 20$ K to minimize the influence from higher CEF levels. For red chains (accessible through χ_c), the best fit is achieved for $J_1 = -0.10(2)$ meV, $J_2 = 0.04(3)$ meV. These exchange parameters define an unfrustrated spin chain where all interactions are simultaneously satisfied by the Néel structure ($\uparrow\downarrow\uparrow\downarrow$). χ_b for blue chains is best fit with $J_1 = -0.14(3)$ meV, $J_2 = -0.21(1)$ meV. While these competing interactions produce incommensurate correlations at finite temperatures the ground state is the double Néel structure ($\uparrow\uparrow\downarrow\downarrow$).⁸ The magnetic moment sizes extracted from fitting for red and blue sites are $5.5(3) \mu_B$ and $8.1(2) \mu_B$, which are consistent with neutron diffraction measurements.^{102,104}

A critical test of this quasi-1D model for SrHo_2O_4 is offered by Fig. 4.7. Frames (e) and (f) show a calculation of the diffuse magnetic neutron scattering intensity from such spin chains based on the Fourier transformation of the two-point correlation function $G(r)$ for the exchange constants derived from χ_c and χ_b and the structure of the ladders. Only an overall scale factor and a constant background were varied to achieve the excellent account of the elastic neutron scattering data in Fig. 4.7(c)-(d). Though no correlations between spin chains are included, the finite width of the zig-zag spin ladders and the two different red ladder orientations in SrHo_2O_4 (Fig. 4.3(b))

produce the checker-board-like structure in the $(HK0)$ plane. It is remarkable that a purely 1D model can account for the magnetism of a dense 3D assembly of spin chains. Contributing to this is surely the different spin orientations for red and blue sites and the incompatible modulation wave vectors.

4.3.4 Magnetic Long Range Order

While the strictly 1D ANNNI model can only form long range order at $T = 0$ K, finite inter-chain interactions induce long range order at finite T . Fig. 4.4(b) shows evidence for such a bulk phase transition in low T heat capacity. Here the magnetic part of heat capacity C_{mag} was obtained after subtracting a Nuclear Schottky Anomaly associated with the hyperfine field on the holmium nuclei.⁵³ The peak position in C_{mag}/T at 0.61(2) K, is consistent with the onset of magnetic Bragg diffractions (Fig. 4.10(a)).^{102,103} The corresponding change in entropy (Fig. 4.4(c)) exceeds $R\ln(2)$ because of higher lying crystal field levels.

We now investigate the low temperature static spin configuration in detail through single crystal elastic neutron scattering in the $(0KL)$ and $(H0L)$ planes. Firstly $L-$ scans at all reachable (n_a, n_b, n_c) and $(n_a, n_b, n_c + 1/2)$ positions (n_a, n_b, n_c being integers) in both planes are resolution limited at $T = 0.28$ K. This is evidence of quasi-1D correlations exceeding 286(5) Å and 100(1) Å for red and blue chains, respectively. The different limits arise because the different longitudinal and transverse resolutions come into play: the $L-$ scan is a rocking scan for red chains but a longitudinal scan

CHAPTER 4. DISORDER FROM ORDER AMONG ANNNI SPIN CHAINS IN SRHO_2O_4

for blue chains, which results in better resolution for red chains.

T -dependent $(0K0)$ scans for $K \in [0.5, 4.5]$ between 0.28 K and 10 K were carried out to probe correlation between red chains along **b**. As shown in Fig. 4.12(a), upon cooling, a broad intensity modulation develops and turns into resolution limited Bragg peaks for T below $T_N = 0.68(2)$ K. Measurements at (200) and (030) indicate the correlation length for red spins exceeds $57(1)$ Å and $64(1)$ Å respectively along **a** and **b** below T_N .

Despite a spin correlation length exceeding $100(1)$ Å along **c**, blue chains fail to develop conventional long range inter-chain correlations, as shown in Fig. 4.12(b)(c). Significant inter-chain correlations develops at low temperatures as manifested by sharpening of peak shapes, but no long range order is formed. For a closer look at the low temperature correlations between blue chains, H - and K - scans through $(00\frac{1}{2})$ at 0.28 K are shown in Fig. 4.9. The broad modulations are well described by Lorentzian fits that correspond to correlation length along **a** and **b** of just $6.0(1)$ Å and $17.5(3)$ Å respectively. The H - scan includes a small sharp component that indicates some correlations between blue chains persists to a separation of $165(9)$ Å perpendicular to their easy axis, a curious discovery that merits further exploration.

To understand the interplay between the two types of spin chains, detailed T dependent scans were carried out through the (030) and $(00\frac{1}{2})$ peaks, which respectively arise from red and blue chains (Fig. 4.10). The result for red sites is shown in Fig. 4.10(a). The integrated intensity of the peak, a measure of the staggered magneti-

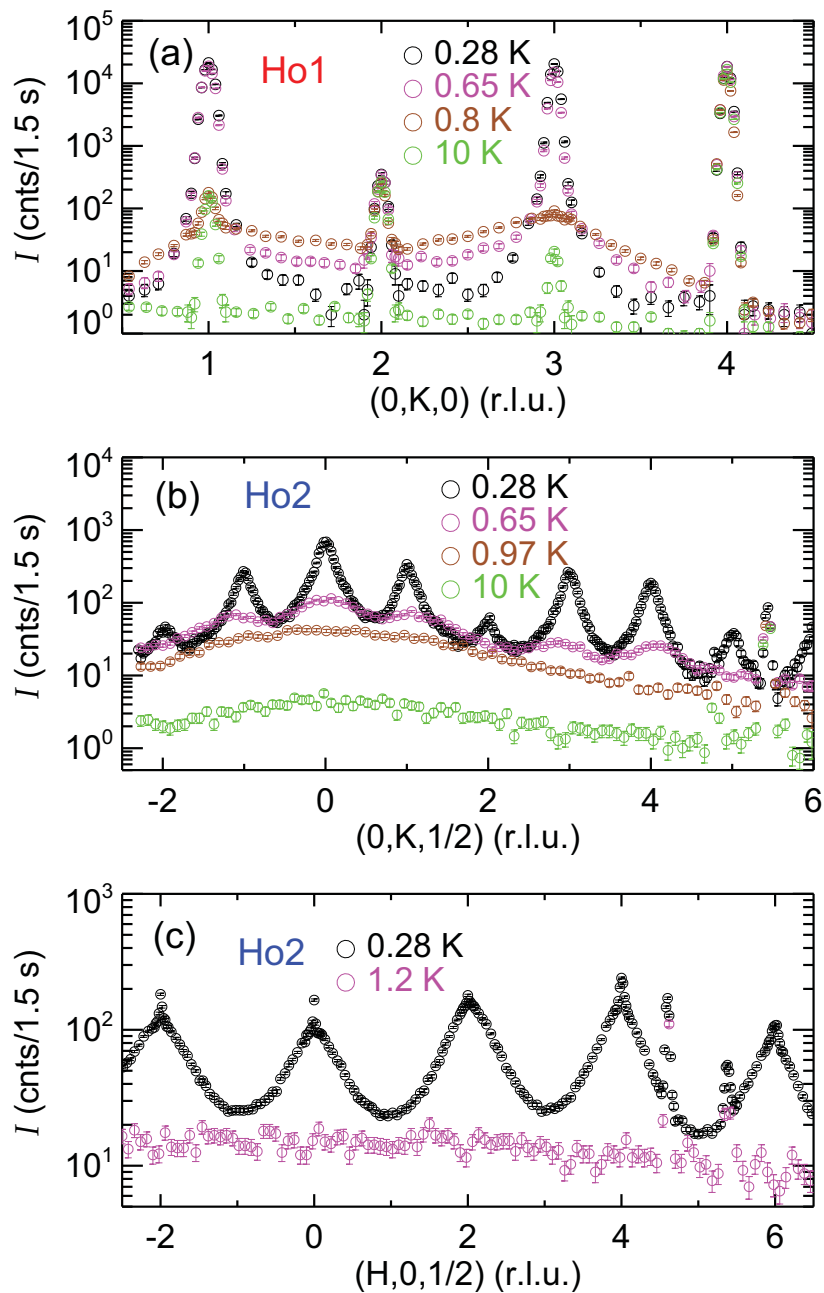


Figure 4.8: Thermal evolution of inter-chain correlations for (a) red Ho1 chains along \mathbf{b} , and blue Ho2 chains (b) along \mathbf{b} and (c) along \mathbf{a} .

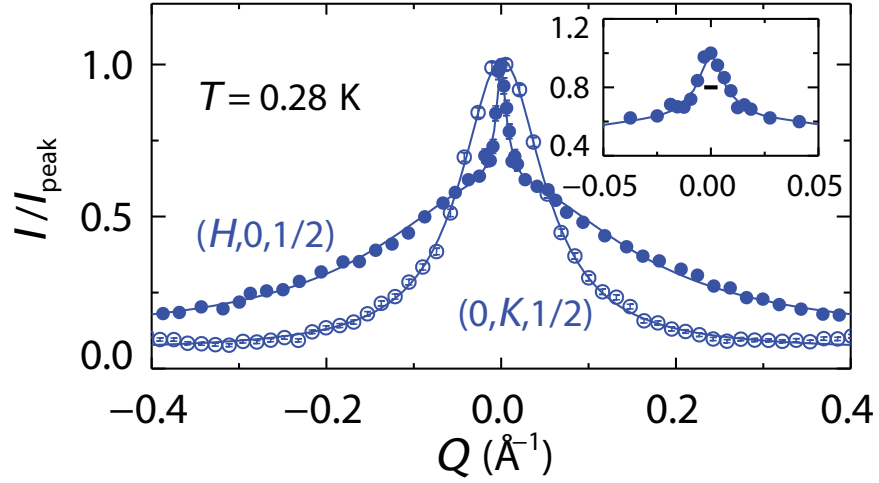


Figure 4.9: Inter-chain correlations for blue sites probed by neutrons. Filled and empty circles are from H - and K - scans at $(00\frac{1}{2})$ measured at 0.28 K. The solid lines show fits to the data. Inset shows sharp component of H - scan in detail, the horizontal bar is the instrumental resolution. Data from different sample orientations are normalized by the peak count rate.⁹

zation, grows below T_N then saturates at $T_S = 0.52(2)$ K. This saturation is consistent with a second order phase transition in a uniaxial spin system where the gap in the magnetic excitation spectrum produces a characteristic saturation temperature. Near T_N , the critical exponent $\beta = 0.36(2)$ is consistent with that for the 3D Ising model ($\beta_{3DI} = 0.3258(14)$), but also indistinguishable from 3D XY ($\beta_{3DXY} = 0.3470(14)$) and 3D Heisenberg models ($\beta_{3DH} = 0.3662(25)$).¹⁰⁷ The peak width (not shown) decreases markedly upon cooling towards T_N signalling the development of commensurate long range correlations among red spins.

A rather different situation is found for the blue chains. There is no anomaly in T dependent L -integrated intensity of the $(00\frac{1}{2})$ peak at T_N but a gradual increase upon cooling that terminates at T_S . The nature of spin correlations along the blue chains is

CHAPTER 4. DISORDER FROM ORDER AMONG ANNNI SPIN CHAINS IN SRHO_2O_4

probed by the position and width of the $(00\frac{1}{2})$ peak. Both evolve continuously across T_N in semi-quantitative agreement with the ANNNI model, using the parameters that also describe the susceptibility and diffuse neutron scattering data. The trend however, ceases abruptly at T_S with a peak center position of $0.501\mathbf{c}^*$. The deviation, Δq_c , from the commensurate position $\mathbf{c}^*/2$ is significant and a long wave length modulated structure is also apparent as an oscillation of the centers for other $(0K\frac{1}{2})$ type peaks with $K = 1, 2, 3, 4, 5$, which is consistent with $G(r)$ for the incommensurate zig-zag ladder (insert to Fig. 4.10(c)).

To understand the very different behaviors of red and blue spin chains it is useful to consult the 3D ANNNI model.⁸ For the red chains, where $J_2/J_1 = -0.4(3)$, the mean field phase diagram predicts a single phase transition from paramagnetic (PM) phase to 3D Néel order, which is consistent with the experimental observation. The exchange parameters of the blue chains however, place these in a complicated part of the phase diagram. Between the PM phase and the 3D double-Néel order exists a large number of 3D LRO phases with different modulation wave vectors. These can be described in terms of different arrangements of domain-wall-like defects within the double Néel structure. Effective interactions between defects stabilize these various phases at different temperatures. With this picture in mind, the continuous peak center shift observed in Fig. 4.10(c) actually reflects domain wall rearrangement along the chains. With four sites per magnetic unit cell there are four different types of domains that correspond to shifting the $(\uparrow\uparrow\downarrow\downarrow)$ motif with respect to the

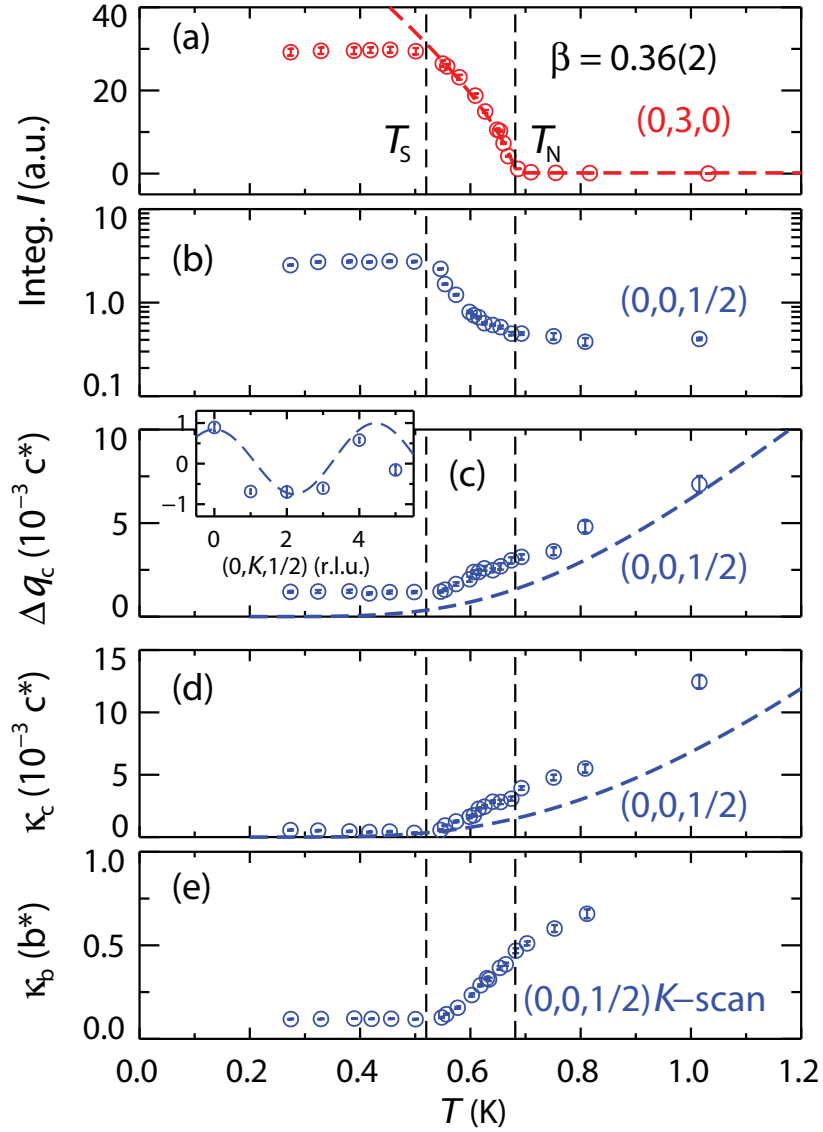


Figure 4.10: Spin correlations versus T in SrHo_2O_4 probed by neutrons. (a)-(d) show results from L -scans at (030) (red) and $(00\frac{1}{2})$ (blue) that probe correlations along red and blue chains respectively. (a)(b) show integrated intensities. (c) shows the peak shift from $(00\frac{1}{2})$. The inset shows the peak shift along c^* from $(0K\frac{1}{2})$. The dashed line shows the predicted shift based on the $J_1 - J_2$ model. (d) shows the inverse correlation length κ_c determined by half width at half maximum of resolution convoluted Lorentzian fits. (e) shows κ_b extracted from K -scans at $(00\frac{1}{2})$. Black dashed lines indicate T_N and T_S . Blue dashed lines in (c)(d) are ANNNI model calculations.⁹

CHAPTER 4. DISORDER FROM ORDER AMONG ANNNI SPIN CHAINS IN SRHO_2O_4

origin. Focusing on domain walls, full 3D LRO requires registry in the placement of transitions between domains along all blue spin chains. Such collective domain wall motion requires rearrangement of large numbers of spins and so can be a slow process. Further, in the non-Kramers doublet ground state of Ho^{3+} , a spin flip can only take place through tunneling or a thermal process involving higher CEF levels. In the recently proposed CEF level scheme based on neutron scattering measurements,¹⁰⁴ which is in qualitative agreement with our point charge model calculations, blue sites have a large energy gap (~ 12 meV) to the first excited state (compared to ~ 1 meV for red sites), which reduces the tunneling and thermal rate for blue spin flips at low temperature. The experimental observation that the spin configuration on blue chains ceases to evolve when red chains become fully ordered for $T < T_S$ (Fig. 4.10) indicates fluctuating exchange fields from spin dynamics in the red chains - which have a lower barrier to spin flips - are the dominant source of spin dynamics on blue chains. Ironically, it is then the development of saturated order on red chains that increases the relaxation time for domain wall motion in blue chains and stunts their inter-chain correlations.

4.3.5 Static magnetic moment size

The static magnetic moment sizes of Ho ions below T_S can be estimated by the elastic scattering intensities measured at 0.3 K.

First consider Ho1 ions which form the 3D long range order. Since the propagation

CHAPTER 4. DISORDER FROM ORDER AMONG ANNNI SPIN CHAINS IN SRHO₂O₄

vector $\mathbf{k} = 0$, the Bragg peak intensities are in general a mixture of nuclear and magnetic scattering. For unpolarized neutrons which were used in this study, the total scattering intensity is simply the sum of these two contributions:

$$I_1(\mathbf{q}) = \mathcal{C}_0[S_N(\mathbf{q}) + \sum_{\alpha\beta} (\delta_{\alpha\beta} - \frac{q^\alpha q^\beta}{|\mathbf{q}|^2}) S_M^{\alpha\beta}(\mathbf{q}) F(|\mathbf{q}|)^2] R(\mathbf{q}) \quad (4.11)$$

here $I_1(\mathbf{q})$ is the integrated intensity of a scan through the peak position \mathbf{q} , \mathcal{C}_0 is the overall scale factor, $S_N(\mathbf{q})$ is the nuclear structure factor, $S_M^{\alpha\beta}(\mathbf{q})$ is the magnetic structure factor, $F(|\mathbf{q}|)$ is the magnetic form factor of Ho³⁺, and $R(\mathbf{q})$ is the corresponding integrated instrumental resolution at \mathbf{q} . Note that Debye-Waller factor was neglected in the analysis since its $|\mathbf{q}|$ dependence is negligible at the temperature and in the range of $|\mathbf{q}|$ where the measurements were done.

Representation analysis using SARAH¹⁰⁸ showed that with $\mathbf{k} = 0$ there are only two magnetic structures that are compatible with the easy \mathbf{c} -axis anisotropy and the short range magnetic order inferred from the diffusive scattering pattern. Using the labeling of red Ho1 atoms in the unit cell as shown in Fig. 4.11, these two structures can be represented as $\phi_{1,2} \equiv (\mathbf{m}_1, \mathbf{m}_2, \mathbf{m}_3, \mathbf{m}_4) = m\hat{\mathbf{c}}(1, \pm 1, -1, \mp 1)$, where \mathbf{m}_i is the magnetic moment on atom i , m is the moment size, and $\hat{\mathbf{c}}$ is the unit vector along \mathbf{c} -axis. The experimental observation that all nuclear forbidden Bragg peaks in the (HOL) plane with even H indices have negligible magnetic scattering intensity shows

CHAPTER 4. DISORDER FROM ORDER AMONG ANNNI SPIN CHAINS IN SrHo_2O_4

that ϕ_1 is the appropriate magnetic structure, since ϕ_2 would give rise to magnetic Bragg peaks at such locations.

In order to extract the magnetic moment size for Ho1, the L -integrated intensities of all reachable Bragg peak positions with integer indices were compared to calculations of Eq. 4.11. Measurements in the $(0KL)$ and $(H0L)$ planes were co-refined together while keeping the ratio of pre-factors, \mathcal{C}_0 in the two reciprocal lattice planes fixed at the mass ratio of the samples used in the corresponding settings. The best fit is shown in Fig. 4.12(a) with the moment size extracted for Ho1 of $6.8 \pm 0.4 \mu_B$.

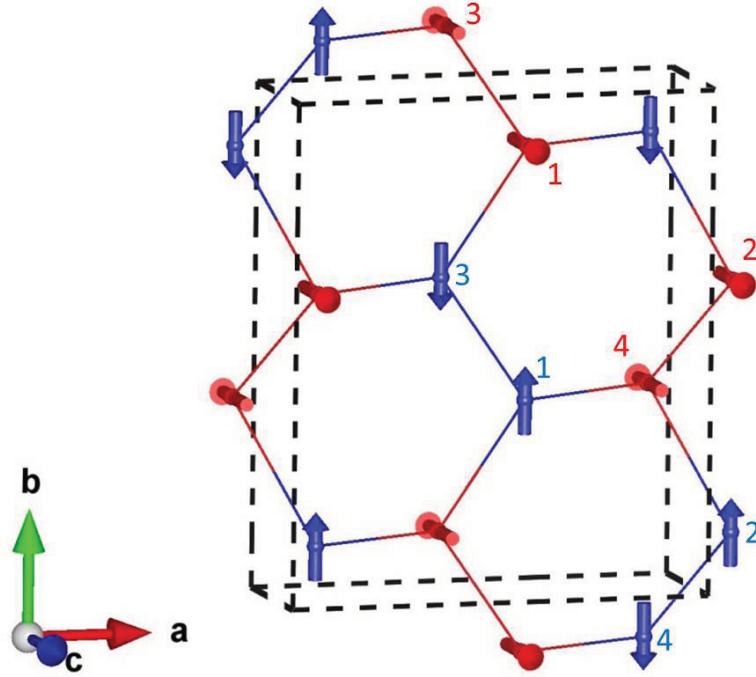


Figure 4.11: Schematic representation of the spin structure in SrHo_2O_4 . 4 Ho1 spins and 4 Ho2 spins in the unit cell are labeled by 1-4 respectively.

As for the Ho2 ions, since the correlation length is short along \mathbf{a} and \mathbf{b} directions,

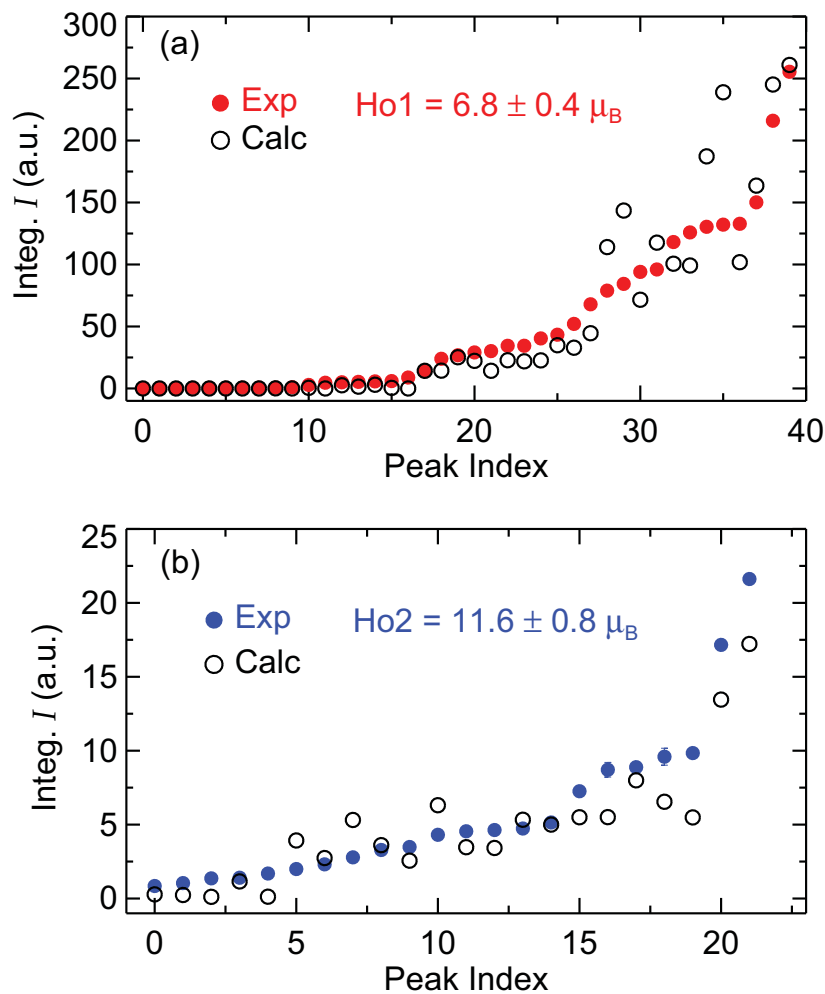


Figure 4.12: Magnetic moment size refinements. Filled circles are the experimental L -integrated intensities for peaks with integer L index in (a) and half odd integer L index in (b) that correspond to Ho1 and Ho2 sites respectively. Open circle show the fitting results as described in the text. All experimental peak intensities are plotted in ascending order.

CHAPTER 4. DISORDER FROM ORDER AMONG ANNNI SPIN CHAINS IN SRHO_2O_4

we assume that the peak shape is a direct production of a sharp Gaussian along \mathbf{c} with two broad Lorentzians along \mathbf{a} and \mathbf{b} . For measurements in $(0KL)$ plane, the peak width of the Gaussian and the in-plane Lorentzian were taken from fittings to the experimental data, while the peak width for the out of plane Lorentzian was assumed to be the same at all peak positions and was approximated by the average peak width along \mathbf{a} measured in $(H0L)$ plane. Note that when taking the average, each peak width was weighted by the corresponding integrated intensity so that stronger peaks, whose peak width are more reliable, have large weights during the averaging: $\text{FWHM} = \sum_i \text{FWHM}_i \cdot I_i / \sum_i I_i$. Following the same procedure, the out of plane width for peaks within the $(H0L)$ plane were obtained from measurements in the $(0KL)$ plane.

The integrated intensities are related to the magnetic structure factor through

$$I_2(\mathbf{q}) = C_0 \sum_{\alpha\beta} \left(\delta_{\alpha\beta} - \frac{q^\alpha q^\beta}{|\mathbf{q}|^2} \right) S_M^{\alpha\beta}(\mathbf{q}) F(|\mathbf{q}|)^2 R'(\mathbf{q}), \quad (4.12)$$

where $R'(\mathbf{q})$ was obtained by integrating the convolution of the instrumental resolution and the peak shape. Representation analysis for $\mathbf{k} = (0, 0, 0.5)$ allows for spin structures of the form $\psi = m_1 \hat{\mathbf{b}}(1, 1, 0, 0) + m_2 \hat{\mathbf{b}}(0, 0, 1, 1)$. Since there is no 3D long range order, this magnetic structure only reflects the local ordered pattern. It was assumed $|m_1| = |m_2|$ since all four Ho2 ions in the unit cell are equivalent in the

CHAPTER 4. DISORDER FROM ORDER AMONG ANNNI SPIN CHAINS IN SRHO_2O_4

paramagnetic phase, and no significant improvement in refinement was obtained by allowing them to vary separately. After enforcing this constraint, there are still two different magnetic structures $\psi_{1,2} = m\hat{\mathbf{b}}(1, 1, \pm 1, \pm 1)$, which can be considered as two domain types that are related by mirror reflection about the \mathbf{ab} plane. With no *a priori* reason to favor one domain over the other, it was assumed that both domains contribute equally. Using the same \mathcal{C}_0 values obtained from refinement of the Ho1 moment size, a fitting of Eq. 4.12 to all the L -intergrated intensities of peaks in $(0KL)$ and $(H0L)$ planes with half-odd integer L index was carried out, and resulted in a moment size of $11.6 \pm 0.8 \mu_B$ for Ho2, as shown in Fig. 4.12(b). The difference in the moment sizes for Ho1 and Ho2 is allowed by the different CEF environments for these two sites.

The magnetic moment sizes extracted from the neutron measurements ($6.8(4) \mu_B$ and $11.6(8) \mu_B$ for red and blue Ho) are in good agreement with those obtained from ANNNI susceptibility fit ($5.5(3) \mu_B$ and $8.1(2) \mu_B$ respectively). $11.6(8) \mu_B$ for blue Ho2 is close to the maximal magnetic moment size of $10 \mu_B$ for a Ho^{3+} ion, indicating an extremely strong Ising character for blue Ho2 ions. Note that the corresponding magnetic moment sizes calculated according to the point charge model CEF ground state (Fig. 4.11) are $9.3 \mu_B$ and $9.8 \mu_B$ for red and blue sites respectively.

4.4 Conclusion

In conclusion, our experiments on SrHo_2O_4 show a magnetically disordered state can be realized within a high quality crystal not because it is energetically favorable but because it is the thermodynamic equilibrium state when, upon cooling, ergodicity is lost. SrHo_2O_4 also illustrates the remarkably disruptive impact of topological defects in d dimensions (here $d = 1$) on $d+1$ dimensional order. Combining the ingredients of large scale emergent structures from frustration and reduced dimensionality, kinetically trapped spin disorder may actually be possible without quenched disorder.

Chapter 5

Conclusion

Through the experimental study of unconventional magnetism in three frustrated magnets $\text{Pr}_2\text{Zr}_2\text{O}_7$, NiGa_2S_4 , and SrHo_2S_4 , this thesis showcases the emergence of various types of short range order at low temperatures in nominally pure crystalline samples, which arise as a result of the intricate interplay between magnetic frustration and other degrees of freedom at play in the particular material.

In $\text{Pr}_2\text{Zr}_2\text{O}_7$, the discovery of extreme sensitivity of the magnetic state to material physical properties and details in sample synthesis emphasizes the importance of careful synthesis work in research on frustrated magnetism where details do matter in significant ways. Through elastic neutron scattering measurements, the spins are found to be correlated according to the local “2-in 2-out” ice rule over long time scales. Inelastic neutron scattering revealed a continuous spectrum that carries most of the neutron scattering spectral weight, consistent with the theoretical proposal that Pr

CHAPTER 5. CONCLUSION

based spin ice should be more dynamical at low temperatures. From the temperature and magnetic field dependence of the spectrum, an inhomogeneous distribution of transverse field that splits the non-Kramers doublet ground state of Pr^{3+} was inferred, suggesting reduced symmetry at the Pr site. Such effects might also be relevant in other non-Kramers pyrochlore materials. The physical origin of the disorder at the Pr site requires further investigation of local structure. Efforts in such direction will help to resolve whether there is an intrinsic lattice instability in $\text{Pr}_2\text{Zr}_2\text{O}_7$.

NiGa_2S_4 is a case where an elusive factor beyond the frustrated inter-spin interactions leads to the short range ordered state. The continuum neutron spectrum that was reported in this thesis provides an essential test for any theoretical model proposed for this material. The magnetic field dependence of the spectrum will be informative to determine the origin of the continuum. Another future direction will be to try to drive this material close/into a long range ordered state by perturbations such as pressure or uniaxial strain. Successfully producing an ordered state is likely to reveal insight into the relevant degrees of freedom that precludes ordering under ambient conditions.

The detailed study of magnetic ordering in SrHo_2O_4 brings out another aspect of frustrated magnetism that could be responsible for precluding long range order: The spin relaxation time scale in this Ising spin system becomes extremely long as a result of the formation of weakly interacting large scale incommensurate structures due to frustration, and single ion crystal field effects that hinder spin flips. Because of this

CHAPTER 5. CONCLUSION

inability to equilibrate, the spin system is not ergodic but trapped in a short range ordered state. To directly probe the changing of relaxation time scale it will be interesting to measure the frequency dependent AC magnetic susceptibility of SrHo_2O_4 at low temperatures. The measurement of the evolution of magnetic correlations under the influence of a transverse field along the \mathbf{a} direction, which should facilitate spin flips and reduce the relaxation time scale, is also worth pursuing to elucidate the proposed “disorder by order” mechanism.

The materials studied in this thesis provides only a minuscule view into the vast possibilities of novel correlated magnetism in frustrated magnets. With advances in solid state chemistry more frustrated compounds with interesting properties will come to the table, and with its unique sensitivity to magnetic and structural properties, and advances in instrumentation and sources neutron scattering will continue to play a very important role in this exploration of the exotic properties of quantum correlated spins.

Appendix A

Neutron Scattering

A.1 Basic Properties of Neutrons

Some properties of neutrons make them an ideal experimental tool for condensed matter systems. Charge neutral and thus highly penetrating, neutrons are easy to work with in different sample environments such as cryostats, furnaces, and pressure cells. The mass of the neutron is such that neutrons with *de Broglie* wavelength 1 \AA have a kinetic energy of 81.81 meV, thus both the length and energy scales are appropriate for probing most crystals. Furthermore, neutrons carry spin-1/2 which allows investigation of magnetic materials.

A.2 Production and Detection of Neutrons

Neutrons can be produced through nuclear reactions such as fission, photofission, fusion, and spallation.¹⁰⁹ Fission of ^{235}U or ^{239}Pu and proton induced spallation of heavy target such as Hg, U, W, Ta, Pb are the dominant methods for generating neutrons from nuclei at neutron scattering facilities.

Due to the weakness of interaction between neutrons and matter it is difficult to detect neutrons directly, and they are usually detected through secondary ionization after neutron absorption. In the commonly used ^3He gas proportional detector, a neutron captured by ^3He goes through the following reaction



The reaction products cause ionization in the gas, which is picked up by an anode wire at high voltage and produces an electric signal for neutron detection.¹⁰⁹

A.3 Neutron Scattering Cross-Section and Correlation Functions

The quantity measured in a neutron scattering experiment is the neutron scattering cross-section.

APPENDIX A. NEUTRON SCATTERING

The differential cross-section which is measured in a diffraction experiment is defined as¹⁰⁹

$$\frac{d\sigma}{d\Omega} = \frac{N(\Omega)}{\phi_0 d\Omega}, \quad (\text{A.2})$$

where $N(\Omega)$ is the number of neutrons scattered per second into a solid angle $d\Omega$, ϕ_0 is the incident flux.

The double differential cross-section where the change of neutron energy is also measured is defined by¹⁰⁹

$$\frac{d^2\sigma}{d\Omega dE_f} = \frac{N(\Omega, E_f)}{\phi_0 d\Omega dE_f}, \quad (\text{A.3})$$

where $N(\Omega, E_f)$ is the number of neutrons scattered per second into a solid angle $d\Omega$ with final energy between E_f and $E_f + dE_f$.

Since neutrons act only as a weak perturbation, the Born approximation can be used to calculate the scattering cross-section, which allows a direct connection between the neutron scattering cross-section and various correlation functions associated with the material under investigation:

$$\frac{d^2\sigma}{d\Omega dE_f}(\mathbf{q}, \omega) \sim \int dt \langle O(\mathbf{q})O(-\mathbf{q}, t) \rangle e^{-i\omega t}, \quad (\text{A.4})$$

where $O(\mathbf{q}, t) \equiv \sum_{\mathbf{r}} e^{i\mathbf{q}\cdot\mathbf{r}(t)}$ for nuclear scattering, while $O(\mathbf{q}, t) \equiv \sum_{\mathbf{r}} \mathbf{S}(\mathbf{r}, t)e^{i\mathbf{q}\cdot\mathbf{r}}$ for

APPENDIX A. NEUTRON SCATTERING

magnetic scattering with \mathbf{S} the spin operator. This correspondence between cross-section and correlation function is used extensively in the interpretation and modeling of neutron scattering data in this thesis. The detail derivations can be found in books by Squires⁴⁷ and Lovesey.¹¹⁰

Appendix B

Vanadium Normalization of neutron scattering from $\text{Pr}_2\text{Zr}_2\text{O}_7$

B.1 Basic Idea

The neutron scattering intensity I measured on a spectrometer is related to the cross section by (assume I is monitor normalized):

$$I(\mathbf{q}, \omega) = C \cdot \int \frac{k_i}{k_f} \frac{d^2\sigma}{d\Omega dE}(\mathbf{q}', \omega') R(\mathbf{q} - \mathbf{q}', \omega - \omega') d\mathbf{q}' d\omega' \quad (\text{B.1})$$

where C is a numerical constant that depends on the specific instrumental configuration, $R(\mathbf{q}, \omega)$ is the unity normalized instrumental resolution function. In order to put the measured scattering cross section in absolute unit, we need to obtain the value of

APPENDIX B. VANADIUM NORMALIZATION OF NEUTRON SCATTERING FROM $\text{Pr}_2\text{Zr}_2\text{O}_7$

\mathcal{C} . One way to do this is to measure with the same instrumental configuration a well known scattering cross section. This could be a nuclear Bragg peak with a known structure factor, or an acoustic phonon, or it could be the incoherent elastic scattering from a known quantity of Vanadium. Here the latter Vanadium measurement was used for the normalization. The neutron cross section from Vanadium takes a simple form:

$$\left(\frac{d^2\sigma}{d\Omega dE}\right)_V(\mathbf{q}, \omega) = N_V \frac{\sigma_i}{4\pi} \exp(-\langle \mathbf{q} \cdot \mathbf{u} \rangle^2) \delta(\hbar\omega) \quad (\text{B.2})$$

where N_V is the number of Vanadium atom, $\frac{\sigma_i}{4\pi}$ is the incoherent neutron scattering cross section of Vanadium, \mathbf{u} is the thermal displacement parameter. $\exp(-\langle \mathbf{q} \cdot \mathbf{u} \rangle^2)$ is near unity for the relevant range of temperatures and momentum transfer and will be neglected in the following analysis.

Thus the measured neutron scattering intensity from Vanadium sample is

$$I_V(\mathbf{q}, \omega) = \mathcal{C} \cdot N_V \frac{\sigma_i}{4\pi} \int R(\mathbf{q} - \mathbf{q}', \omega) d\mathbf{q}' \quad (\text{B.3})$$

B.2 Elastic VS Inelastic

Elastic scattering from $\text{Pr}_2\text{Zr}_2\text{O}_7$ is sharp in energy and broad in \mathbf{q} , thus the elastic scattering intensity is related to elastic cross section by

APPENDIX B. VANADIUM NORMALIZATION OF NEUTRON SCATTERING
FROM $\text{Pr}_2\text{Zr}_2\text{O}_7$

$$I_{\text{EL}}(\mathbf{q}) = \mathcal{C} \cdot N_{\text{Pr}} \left(\frac{d\sigma}{d\Omega} \right)_{\text{EL}}(\mathbf{q}) \int R(\mathbf{q} - \mathbf{q}', 0) d\mathbf{q}' \quad (\text{B.4})$$

where N_{Pr} is the number of Pr in the sample.

By comparing to Eq. B.3, we get the normalized elastic cross section for $\text{Pr}_2\text{Zr}_2\text{O}_7$:

$$\left(\frac{d\sigma}{d\Omega} \right)_{\text{EL}}(\mathbf{q}) = \frac{I_{\text{EL}}(\mathbf{q})}{I_{\text{V}}(\mathbf{q}, \omega = 0)} \frac{N_{\text{V}} \frac{\sigma_i}{4\pi}}{N_{\text{Pr}}} \quad (\text{B.5})$$

Following the same procedure and noticing that inelastic scattering from $\text{Pr}_2\text{Zr}_2\text{O}_7$ is broad in both energy and \mathbf{q} , we obtain the normalized inelastic cross section as follows:

$$\frac{k_i}{k_f} \left(\frac{d^2\sigma}{d\Omega dE} \right)_{\text{IN}}(\mathbf{q}, \omega) = \frac{I_{\text{IN}}(\mathbf{q}, \omega)}{\int I_{\text{V}}(\mathbf{q}, \omega') d\omega'} \frac{N_{\text{V}} \frac{\sigma_i}{4\pi}}{N_{\text{Pr}}} \quad (\text{B.6})$$

Appendix C

$\text{Pr}_2\text{Zr}_2\text{O}_7$ Random Phase

Approximation

Before going into the details of RPA calculation on pyrochlore lattice, I will first establish a convenient way of labeling spins on the lattice. The pyrochlore lattice can be described in terms of a FCC lattice of tetrahedra. Fig. C.1 indicates a particular way of labeling sites. All spins (\mathbf{J}) on the pyrochlore lattice can be labelled by a two component index: $\mathbf{J}_i, i \equiv (\mathbf{R}_i, \sigma)$. Here \mathbf{R} points to the center of a tetrahedron and $\sigma = 1, 2, 3, 4$ label the particular spins on the tetrahedron. The spatial position of a spin is then $\mathbf{r}_i = \mathbf{R}_i + \mathbf{e}_\sigma$, where $\mathbf{e}_1 = a/8(1, -1, 1)$, $\mathbf{e}_2 = a/8(-1, 1, 1)$, $\mathbf{e}_3 = a/8(-1, -1, -1)$, $\mathbf{e}_4 = a/8(1, 1, -1)$, with a the lattice constant.

The RPA calculation of the magnetic susceptibility takes the forms of (Eq. 2.13

APPENDIX C. $\text{Pr}_2\text{Zr}_2\text{O}_7$ RANDOM PHASE APPROXIMATION

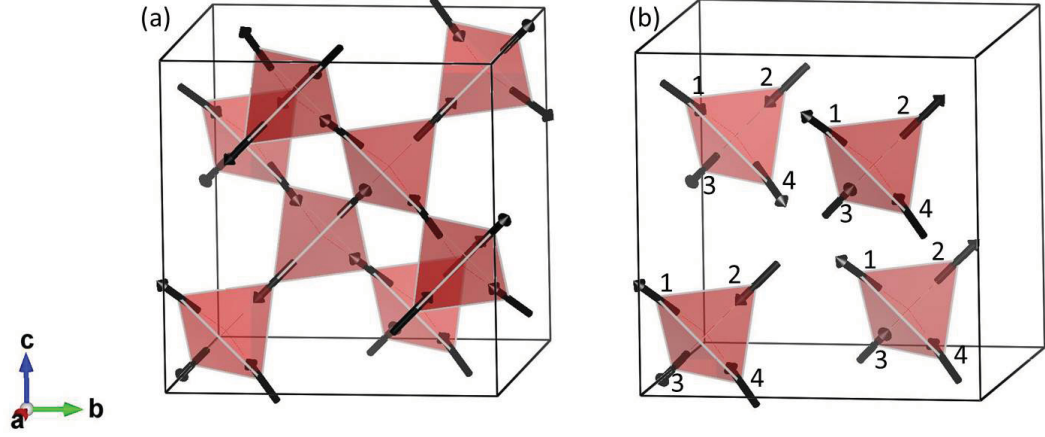


Figure C.1: (a) Conventional unit cell of Pyrochlore lattice. It can be considered as a FCC lattice of tetrahedra as shown in (b). One particular way of labeling spins is shown.

in Chapt. 2)

$$\chi(ij, \omega) = \chi_i^0(\omega)(\delta_{ij} + \sum_{j'} J(ij')\chi(j'j, \omega)) \quad (\text{C.1})$$

Here $\chi^0(\omega)$ is the single ion susceptibility due to non-interacting part of the Hamiltonian and $J(ij)$ is the exchange constant between spins at site i and j .

It is convenient to do the calculation in reciprocal space. For this purpose I will first define the Fourier transform of the two point susceptibility as

$$\chi_\sigma(\mathbf{q}, \omega) = \sum_j \chi(ij, \omega) e^{-i\mathbf{q} \cdot (\mathbf{r}_j - \mathbf{r}_i)}, \quad (\text{C.2})$$

where $i = (\mathbf{R}_i, \sigma)$. Fourier transforming Eq. C.1 considering only nearest neighbor

APPENDIX C. $\text{Pr}_2\text{Zr}_2\text{O}_7$ RANDOM PHASE APPROXIMATION

interaction, we get

$$\chi_\sigma(\mathbf{q}, \omega) = \chi_\sigma^0(\omega) \left\{ 1 + 2J \sum_{\sigma' \neq \sigma} \chi_{\sigma'}(\mathbf{q}, \omega) \cos[\mathbf{q} \cdot (\mathbf{e}_{\sigma'} - \mathbf{e}_\sigma)] \right\} \quad (\text{C.3})$$

From $\chi_\sigma(\mathbf{q}, \omega)$, the neutron cross section can then readily be calculated as follows⁵⁹

$$\frac{d^2\sigma}{d\Omega dE}(\mathbf{q}, E) \sim \sum_{\alpha\beta} \left(\delta_{\alpha\beta} - \frac{q_\alpha q_\beta}{|\mathbf{q}|^2} \right) S^{\alpha\beta}(\mathbf{q}, \omega) |F(\mathbf{q})|^2 \quad (\text{C.4})$$

$$S^{\alpha\beta}(\mathbf{q}, \omega) = \sum_{\sigma} 2\hbar \frac{1}{1 - e^{-E/k_B T}} (\chi_\sigma^{\alpha\beta})''(\mathbf{q}, E/\hbar). \quad (\text{C.5})$$

Here $F(\mathbf{q})$ is the magnetic form factor for Pr^{3+} , and $\alpha, \beta = x, y, z$ are Cartesian coordinate axes.

To calculate $\chi_\sigma(\mathbf{q}, \omega)$, the non-interacting single ion susceptibility $\chi_\sigma^0(\omega)$ needs to be calculated first. Recall that the single ion part of the Hamiltonian is

$$\mathcal{H}_{\text{SI}} = -g\mathbf{H} \cdot \mathbf{e}_z J_{eff}^z \sigma_z + \Delta \sigma_x \quad (\text{C.6})$$

with two eigenstates $|\phi\rangle$, $\phi = 1, 2$, whose eigenenergies are $E = \pm \sqrt{(g\mathbf{H} \cdot \mathbf{e}_z J_{eff}^z)^2 + \Delta^2}$ respectively.

The single ion susceptibility $\chi_\sigma^0(\omega)$ can be calculated using standard linear re-

APPENDIX C. PR₂ZR₂O₇ RANDOM PHASE APPROXIMATION

sponse theory:⁵⁹

$$(\chi_\sigma^{0\alpha\beta})''(\omega) = \pi \frac{(\mathbf{e}_\alpha \cdot \mathbf{e}_\sigma)(\mathbf{e}_\beta \cdot \mathbf{e}_\sigma)}{|\mathbf{e}_\sigma|^2} (J_{eff}^z)^2 \times \sum_{\phi\phi'} \langle \phi | \sigma_z | \phi' \rangle \langle \phi' | \sigma_z | \phi \rangle (n_\phi - n_{\phi'}) \delta(\hbar\omega - (E_{\phi'} - E_\phi)) \quad (\text{C.7})$$

$$(\chi_\sigma^{0\alpha\beta})'(\omega) = \frac{(\mathbf{e}_\alpha \cdot \mathbf{e}_\sigma)(\mathbf{e}_\beta \cdot \mathbf{e}_\sigma)}{|\mathbf{e}_\sigma|^2} (J_{eff}^z)^2 \times \sum_{\phi\phi'}^{E_\phi \neq E_{\phi'}} \frac{\langle \phi | \sigma_z | \phi' \rangle \langle \phi' | \sigma_z | \phi \rangle}{E_{\phi'} - E_\phi - \hbar\omega} (n_\phi - n_{\phi'}) + (\chi_\sigma^{0\alpha\beta})'(el) \delta_{\omega 0} \quad (\text{C.8})$$

where $\mathbf{e}_{\alpha,\beta}$ are the unit vectors along the corresponding Cartesian coordinate axes and $n_\phi = \frac{e^{-E_\phi/k_B T}}{\sum_{\phi'} e^{-E_{\phi'}/k_B T}}$ is the population factor. $(\chi_\sigma^{0\alpha\beta})'(el)$ is the Curie-Weiss susceptibility

$$(\chi_\sigma^{0\alpha\beta})'(el) = \frac{1}{k_B T} \frac{(\mathbf{e}_\alpha \cdot \mathbf{e}_\sigma)(\mathbf{e}_\beta \cdot \mathbf{e}_\sigma)}{|\mathbf{e}_\sigma|^2} (J_{eff}^z)^2 \left(\sum_{\phi\phi'}^{E_{\phi'}=E_\phi} \langle \phi | \sigma_z | \phi' \rangle \langle \phi' | \sigma_z | \phi \rangle n_\phi \right) \quad (\text{C.9})$$

Due to the Ising anisotropy of the spins, the susceptibility is not isotropic and Eq. C.1 is a tensorial equation. The most convenient way to obtain $\chi_\sigma(\mathbf{q}, \omega)$ is by solving this set of linear equations numerically. For a numerical representation of the δ functions, I will introduce two damping factors Γ_i and Γ_e that respectively gives a small finite width to the δ functions for inelastic and elastic peaks. These damping

APPENDIX C. $\text{Pr}_2\text{Zr}_2\text{O}_7$ RANDOM PHASE APPROXIMATION

factors were set to be 0.001 meV in the calculation. The single ion susceptibility is then calculated by

$$(\chi_\sigma^{0\alpha\beta})''(\omega) = \frac{(\mathbf{e}_\alpha \cdot \mathbf{e}_\sigma)(\mathbf{e}_\beta \cdot \mathbf{e}_\sigma)}{|\mathbf{e}_\sigma|^2} (J_{eff}^z)^2 \times \sum_{\phi\phi'} \frac{\langle \phi | \sigma_z | \phi' \rangle \langle \phi' | \sigma_z | \phi \rangle}{(E_{\phi'} - E_\phi - \hbar\omega)^2 + \Gamma_i^2} \Gamma_i (n_\phi - n_{\phi'}) + \frac{\hbar\omega\Gamma_e}{(\hbar\omega)^2 + \Gamma_e^2} (\chi_\sigma^{0\alpha\beta})'(el) \quad (\text{C.10})$$

$$(\chi_\sigma^{0\alpha\beta})'(\omega) = \frac{(\mathbf{e}_\alpha \cdot \mathbf{e}_\sigma)(\mathbf{e}_\beta \cdot \mathbf{e}_\sigma)}{|\mathbf{e}_\sigma|^2} (J_{eff}^z)^2 \times \sum_{\phi\phi'}^{E_\phi \neq E_{\phi'}} \frac{\langle \phi | \sigma_z | \phi' \rangle \langle \phi' | \sigma_z | \phi \rangle}{(E_{\phi'} - E_\phi - \hbar\omega)^2 + \Gamma_i^2} (E_{\phi'} - E_\phi - \hbar\omega)(n_\phi - n_{\phi'}) + \frac{\Gamma_e^2}{(\hbar\omega)^2 + \Gamma_e^2} (\chi_\sigma^{0\alpha\beta})'(el) \quad (\text{C.11})$$

$\chi_\sigma(\mathbf{q}, \omega, \Delta)$ calculated in this way describes a spin system with homogeneous transverse field, Δ . To account for the fact that in $\text{Pr}_2\text{Zr}_2\text{O}_7$ there is a continuous distribution of Δ , the final susceptibility is approximated by a weighted sum of $\chi_\sigma(\mathbf{q}, \omega, \Delta)$ as

$$\chi_\sigma(\mathbf{q}, \omega) = \int \rho(\Delta) \chi(\mathbf{q}, \omega, \Delta) d\Delta \quad (\text{C.12})$$

where $\rho(\Delta)$ is extracted from the 0 T data in Fig. 2.20(b).

Bibliography

- [1] L. Balents, “Spin liquids in frustrated magnets.” *Nature*, vol. 464, no. 7286, pp. 199–208, Mar. 2010. [Online]. Available: <http://dx.doi.org/10.1038/nature08917>
- [2] M. Hermele, M. P. A. Fisher, and L. Balents, “Pyrochlore photons: The $u(1)$ spin liquid in a $s = \frac{1}{2}$ three-dimensional frustrated magnet,” *Phys. Rev. B*, vol. 69, p. 064404, Feb 2004. [Online]. Available: <http://link.aps.org/doi/10.1103/PhysRevB.69.064404>
- [3] S. Nakatsuji, Y. Nambu, H. Tonomura, O. Sakai, S. Jonas, C. Broholm, H. Tsunetsugu, Y. Qiu, and Y. Maeno, “Spin disorder on a triangular lattice,” *Science*, vol. 309, no. 5741, pp. 1697–1700, 2005. [Online]. Available: <http://www.sciencemag.org/content/309/5741/1697.abstract>
- [4] S. Koohpayeh, J.-J. Wen, B. Trump, C. Broholm, and T. McQueen, “Synthesis, floating zone crystal growth and characterization of the quantum spin ice $\text{pr}_2\text{zr}_2\text{o}_7$ pyrochlore,” *Journal of Crystal Growth*,

BIBLIOGRAPHY

- vol. 402, no. 0, pp. 291 – 298, 2014. [Online]. Available: <http://www.sciencedirect.com/science/article/pii/S0022024814004217>
- [5] K. Kimura, S. Nakatsuji, J.-J. Wen, C. Broholm, M. B. Stone, E. Nishibori, and H. Sawa, “Quantum fluctuations in spin-ice-like $\text{Pr}_2\text{Zr}_2\text{O}_7$,” *Nature communications*, vol. 4, p. 1934, jun 2013. [Online]. Available: <http://www.ncbi.nlm.nih.gov/pubmed/23770751>
- [6] S. Lee, S. Onoda, and L. Balents, “Generic quantum spin ice,” *Phys. Rev. B*, vol. 86, p. 104412, Sep 2012. [Online]. Available: <http://link.aps.org/doi/10.1103/PhysRevB.86.104412>
- [7] A. P. Ramirez, A. Hayashi, R. J. Cava, R. Siddharthan, and B. S. Shastry, “Zero-point entropy in ‘spin ice’,” *Nature*, vol. 399, no. 6734, pp. 333–335, 1999. [Online]. Available: <http://www.nature.com/nature/journal/v399/n6734/abs/399333a0.html>
- [8] W. Selke, “The {ANNNI} model theoretical analysis and experimental application,” *Physics Reports*, vol. 170, no. 4, pp. 213 – 264, 1988. [Online]. Available: <http://www.sciencedirect.com/science/article/pii/0370157388901408>
- [9] J.-J. Wen, W. Tian, V. O. Garlea, S. M. Koohpayeh, T. M. McQueen, H.-F. Li, J.-Q. Yan, D. Vaknin, and C. L. Broholm, “Disorder from Order Among ANNNI Spin Chains in SrHo_2O_4 ,” *ArXiv e-prints*, Jul. 2014.

BIBLIOGRAPHY

- [10] P. W. Anderson, “More is different,” *Science*, vol. 177, no. 4047, pp. 393–396, 1972. [Online]. Available: <http://www.sciencemag.org/content/177/4047/393>.
short
- [11] R. B. Laughlin and D. Pines, “The theory of everything,” *Proceedings of the National Academy of Sciences*, vol. 97, no. 1, pp. 28–31, 2000. [Online]. Available: <http://www.pnas.org/content/97/1/28.abstract>
- [12] P. Anderson, *Basic Notions Of Condensed Matter Physics*, ser. Advanced Books Classics Series. Westview Press, 2008.
- [13] N. Mott, *Metal-Insulator Transitions*. Taylor & Francis, 1990.
- [14] R. White, *Quantum Theory of Magnetism: Magnetic Properties of Materials*, ser. Springer Series in Solid-State Sciences. Springer, 2007.
- [15] J. Goldstone, A. Salam, and S. Weinberg, “Broken symmetries,” *Phys. Rev.*, vol. 127, pp. 965–970, Aug 1962. [Online]. Available: <http://link.aps.org/doi/10.1103/PhysRev.127.965>
- [16] X.-G. Wen, “Quantum orders and symmetric spin liquids,” *Phys. Rev. B*, vol. 65, p. 165113, Apr 2002. [Online]. Available: <http://link.aps.org/doi/10.1103/PhysRevB.65.165113>
- [17] A. M. Essin and M. Hermele, “Classifying fractionalization: Symmetry classification of gapped F_2 spin liquids in two dimensions,” *Phys.*

BIBLIOGRAPHY

- Rev. B*, vol. 87, p. 104406, Mar 2013. [Online]. Available: <http://link.aps.org/doi/10.1103/PhysRevB.87.104406>
- [18] T. Giamarchi, *Quantum Physics in One Dimension*, ser. International Series of Monographs on Physics. Clarendon Press, 2004.
- [19] L. Faddeev and L. Takhtajan, “What is the spin of a spin wave?” *Physics Letters A*, vol. 85, no. 6C7, pp. 375 – 377, 1981. [Online]. Available: <http://www.sciencedirect.com/science/article/pii/0375960181903352>
- [20] D. A. Tennant, T. G. Perring, R. A. Cowley, and S. E. Nagler, “Unbound spinons in the $s=1/2$ antiferromagnetic chain KCuF_3 ,” *Phys. Rev. Lett.*, vol. 70, pp. 4003–4006, Jun 1993. [Online]. Available: <http://link.aps.org/doi/10.1103/PhysRevLett.70.4003>
- [21] H.-C. Jiang, H. Yao, and L. Balents, “Spin liquid ground state of the spin- $\frac{1}{2}$ square J_1 - J_2 heisenberg model,” *Phys. Rev. B*, vol. 86, p. 024424, Jul 2012. [Online]. Available: <http://link.aps.org/doi/10.1103/PhysRevB.86.024424>
- [22] C. Lacroix, P. Mendels, and F. Mila, *Introduction to Frustrated Magnetism: Materials, Experiments, Theory*, ser. Springer Series in Solid-State Sciences. Springer, 2011.
- [23] M. J. P. Gingras, “Spin ice,” *ArXiv e-prints*, Mar. 2009. [Online]. Available: <http://arxiv.org/abs/0903.2772>

BIBLIOGRAPHY

- [24] L. Pauling, “The structure and entropy of ice and of other crystals with some randomness of atomic arrangement,” *Journal of the American Chemical Society*, vol. 57, no. 12, pp. 2680–2684, 1935. [Online]. Available: <http://pubs.acs.org/doi/abs/10.1021/ja01315a102>
- [25] W. F. Giauque and M. F. Ashley, “Molecular rotation in ice at 10k. free energy of formation and entropy of water,” *Phys. Rev.*, vol. 43, pp. 81–82, Jan 1933. [Online]. Available: <http://journals.aps.org/pr/abstract/10.1103/PhysRev.43.81.2#>
- [26] C. L. Henley, “The coulomb phase in frustrated systems,” *Annual Review of Condensed Matter Physics*, vol. 1, no. 1, pp. 179–210, 2010. [Online]. Available: <http://dx.doi.org/10.1146/annurev-conmatphys-070909-104138>
- [27] M. Kardar, *Statistical Physics of Fields*. Cambridge University Press, 2007. [Online]. Available: <http://books.google.com/books?id=nTxBhGX01P4C>
- [28] C. Castelnovo, R. Moessner, and S. L. Sondhi, “Magnetic monopoles in spin ice,” *Nature*, vol. 451, no. 7174, pp. 42–45, 2008. [Online]. Available: <http://www.ncbi.nlm.nih.gov/pubmed/18172493>
- [29] D. E. Freedman, T. H. Han, A. Prodi, P. Mller, Q.-Z. Huang, Y.-S. Chen, S. M. Webb, Y. S. Lee, T. M. McQueen, and D. G. Nocera, “Site specific x-ray anomalous dispersion of the geometrically frustrated kagom magnet, herbertsmithite, $\text{zncu}_3(\text{oh})_6\text{cl}_2$,” *Journal of the American Chemical*

BIBLIOGRAPHY

- Society*, vol. 132, no. 45, pp. 16 185–16 190, 2010. [Online]. Available: <http://pubs.acs.org/doi/abs/10.1021/ja1070398>
- [30] T. Taniguchi, H. Kadowaki, H. Takatsu, B. Fåk, J. Ollivier, T. Yamazaki, T. J. Sato, H. Yoshizawa, Y. Shimura, T. Sakakibara, T. Hong, K. Goto, L. R. Yaraskavitch, and J. B. Kycia, “Long-range order and spin-liquid states of polycrystalline $\text{tb}_{2+x}\text{ti}_{2-x}\text{o}_{7+y}$,” *Phys. Rev. B*, vol. 87, p. 060408, Feb 2013. [Online]. Available: <http://link.aps.org/doi/10.1103/PhysRevB.87.060408>
- [31] T. Fennell, P. P. Deen, A. R. Wildes, K. Schmalzl, D. Prabhakaran, A. T. Boothroyd, R. J. Aldus, D. F. McMorrow, and S. T. Bramwell, “Magnetic coulomb phase in the spin ice $\text{ho}_2\text{ti}_2\text{o}_7$,” *Science*, vol. 326, no. 5951, pp. 415–417, 2009. [Online]. Available: <http://www.sciencemag.org/content/326/5951/415.abstract>
- [32] D. J. P. Morris, D. A. Tennant, S. A. Grigera, B. Klemke, C. Castelnovo, R. Moessner, C. Czternasty, M. Meissner, K. C. Rule, J.-U. Hoffmann, K. Kiefer, S. Gerischer, D. Slobinsky, and R. S. Perry, “Dirac strings and magnetic monopoles in the spin ice $\text{dy}_2\text{ti}_2\text{o}_7$,” *Science*, vol. 326, no. 5951, pp. 411–414, 2009. [Online]. Available: <http://www.sciencemag.org/content/326/5951/411.abstract>
- [33] N. Shannon, O. Sikora, F. Pollmann, K. Penc, and P. Fulde, “Quantum ice: A

BIBLIOGRAPHY

- quantum monte carlo study,” *Phys. Rev. Lett.*, vol. 108, p. 067204, Feb 2012.
[Online]. Available: <http://link.aps.org/doi/10.1103/PhysRevLett.108.067204>
- [34] O. Benton, O. Sikora, and N. Shannon, “Seeing the light: Experimental signatures of emergent electromagnetism in a quantum spin ice,” *Phys. Rev. B*, vol. 86, p. 075154, Aug 2012. [Online]. Available: <http://link.aps.org/doi/10.1103/PhysRevB.86.075154>
- [35] S. Onoda and Y. Tanaka, “Quantum melting of spin ice: Emergent cooperative quadrupole and chirality,” *Phys. Rev. Lett.*, vol. 105, p. 047201, Jul 2010. [Online]. Available: <http://link.aps.org/doi/10.1103/PhysRevLett.105.047201>
- [36] H. D. Zhou, C. R. Wiebe, J. A. Janik, L. Balicas, Y. J. Yo, Y. Qiu, J. R. D. Copley, and J. S. Gardner, “Dynamic spin ice: $\text{Pr}_2\text{Sn}_2\text{O}_7$,” *Phys. Rev. Lett.*, vol. 101, p. 227204, Nov 2008. [Online]. Available: <http://link.aps.org/doi/10.1103/PhysRevLett.101.227204>
- [37] K. A. Ross, L. Savary, B. D. Gaulin, and L. Balents, “Quantum excitations in quantum spin ice,” *Phys. Rev. X*, vol. 1, p. 021002, Oct 2011. [Online]. Available: <http://link.aps.org/doi/10.1103/PhysRevX.1.021002>
- [38] L.-J. Chang, S. Onoda, Y. Su, Y.-J. Kao, K.-D. Tsuei, Y. Yasui, K. Kakurai, and M. R. Lees, “Higgs transition from magnetic coulomb liquid to a ferromagnet in $\text{Yb}_2\text{Ti}_2\text{O}_7$,” *Nature Commun.*, vol. 3, p. 992, 2012.

BIBLIOGRAPHY

- [39] K. A. Ross, T. Proffen, H. A. Dabkowska, J. A. Quilliam, L. R. Yaraskavitch, J. B. Kycia, and B. D. Gaulin, “Lightly stuffed pyrochlore structure of single-crystalline $\text{yb}_2\text{ti}_2\text{o}_7$ grown by the optical floating zone technique,” *Phys. Rev. B*, vol. 86, p. 174424, Nov 2012. [Online]. Available: <http://link.aps.org/doi/10.1103/PhysRevB.86.174424>
- [40] M. Subramanian, G. Aravamudan, and G. S. Rao, “Oxide pyrochlores a review,” *Progress in Solid State Chemistry*, vol. 15, no. 2, pp. 55 – 143, 1983. [Online]. Available: <http://www.sciencedirect.com/science/article/pii/0079678683900018>
- [41] K. Matsuhira, C. Sekine, C. Paulsen, M. Wakeshima, Y. Hinatsu, T. Kitazawa, Y. Kiuchi, Z. Hiroi, and S. Takagi, “Spin freezing in the pyrochlore antiferromagnet $\text{pr}_2\text{zr}_2\text{o}_7$,” *Journal of Physics: Conference Series*, vol. 145, no. 1, p. 012031, 2009. [Online]. Available: <http://stacks.iop.org/1742-6596/145/i=1/a=012031>
- [42] S. Ferro, “Physicochemical and electrical properties of praseodymium oxides,” *International Journal of Electrochemistry*, vol. 2011.
- [43] D. P. Shoemaker, R. Seshadri, M. Tachibana, and A. L. Hector, “Incoherent bi off-centering in $\text{bi}_2\text{ti}_2\text{o}_6$ and $\text{bi}_2\text{ru}_2\text{o}_6$: Insulator versus metal,” *Phys. Rev. B*, vol. 84, p. 064117, Aug 2011. [Online]. Available: <http://link.aps.org/doi/10.1103/PhysRevB.84.064117>

BIBLIOGRAPHY

- [44] S. Koohpayeh, D. Fort, and J. Abell, “The optical floating zone technique: A review of experimental procedures with special reference to oxides,” *Progress in Crystal Growth and Characterization of Materials*, vol. 54, no. 3C4, pp. 121 – 137, 2008. [Online]. Available: <http://www.sciencedirect.com/science/article/pii/S096089740800003X>
- [45] K. Kimura, S. Nakatsuji, and A. Nugroho, “Single-crystal study on the low-temperature magnetism of the pyrochlore magnet $\text{Pr}_2\text{Zr}_2\text{O}_7$,” *Journal of the Korean Physical Society*, vol. 63, no. 3, pp. 719–721, 2013. [Online]. Available: <http://dx.doi.org/10.3938/jkps.63.719>
- [46] D. L. Abernathy, M. B. Stone, M. J. Loguillo, M. S. Lucas, O. Delaire, X. Tang, J. Y. Y. Lin, and B. Fultz, “Design and operation of the wide angular-range chopper spectrometer arcs at the spallation neutron source,” *Review of Scientific Instruments*, vol. 83, no. 1, 2012. [Online]. Available: <http://scitation.aip.org/content/aip/journal/rsi/83/1/10.1063/1.3680104>
- [47] G. Squires, *Introduction to the Theory of Thermal Neutron Scattering*. Cambridge University Press, 2012.
- [48] M. Hutchings, “Point-charge calculations of energy levels of magnetic ions in crystalline electric fields,” *Solid State Physics*, vol. 16, pp. 227 – 273, 1964. [Online]. Available: <http://www.sciencedirect.com/science/article/pii/S0081194708605172>

BIBLIOGRAPHY

- [49] K. W. H. Stevens, “Matrix elements and operator equivalents connected with the magnetic properties of rare earth ions,” *Proceedings of the Physical Society. Section A*, vol. 65, no. 3, p. 209, 1952. [Online]. Available: <http://stacks.iop.org/0370-1298/65/i=3/a=308>
- [50] J. Van Vleck, *The Theory of Electric and Magnetic Susceptibilities*, ser. The International series of monographs on physics. Oxford University Press, 1944.
- [51] S. Rosenkranz, A. P. Ramirez, A. Hayashi, R. J. Cava, R. Siddharthan, and B. S. Shastry, “Crystal-field interaction in the pyrochlore magnet $\text{Ho}_2\text{Ti}_2\text{O}_7$,” *Journal of Applied Physics*, vol. 87, no. 9, pp. 5914–5916, 2000. [Online]. Available: <http://scitation.aip.org/content/aip/journal/jap/87/9/10.1063/1.372565>
- [52] J. Snyder, B. G. Ueland, J. S. Slusky, H. Karunadasa, R. J. Cava, and P. Schiffer, “Low-temperature spin freezing in the $\text{dy}_2\text{ti}_2\text{o}_7$ spin ice,” *Phys. Rev. B*, vol. 69, p. 064414, Feb 2004. [Online]. Available: <http://link.aps.org/doi/10.1103/PhysRevB.69.064414>
- [53] A. Tari, *The Specific Heat of Matter at Low Temperatures*. Imperial College Press, 2003. [Online]. Available: <http://books.google.com/books?id=ymFQ0pRezKwC>
- [54] B. Bleaney, “Hyperfine interactions in rare earth metals,” *Journal of Applied Physics*, vol. 34, no. 4, pp. 1024–1031, 1963. [Online]. Available: <http://scitation.aip.org/content/aip/journal/jap/34/4/10.1063/1.1729355>

BIBLIOGRAPHY

- [55] E. Bertin, P. Bonville, J. P. Bouchaud, J. A. Hodges, J. Sanchez, and P. Vulliet, “Effective hyperfine temperature in frustrated $\text{Gd}_2\text{Sn}_2\text{O}_7$: two level model and ^{155}Gd mössbauer measurements,” *Eur. Phys. J. B*, vol. 27, no. 3, pp. 347–354, JUN 2002.
- [56] J. A. Rodriguez, D. M. Adler, P. C. Brand, C. Broholm, J. C. Cook, C. Brocker, R. Hammond, Z. Huang, P. Hundertmark, J. W. Lynn, N. C. Maliszewskyj, J. Moyer, J. Orndorff, D. Pierce, T. D. Pike, G. Scharfstein, S. A. Smee, and R. Vilaseca, “Macsa new high intensity cold neutron spectrometer at nist,” *Measurement Science and Technology*, vol. 19, no. 3, p. 034023, 2008. [Online]. Available: <http://stacks.iop.org/0957-0233/19/i=3/a=034023>
- [57] J. Copley and J. Cook, “The disk chopper spectrometer at nist: a new instrument for quasielastic neutron scattering studies,” *Chem. Phys.*, vol. 292, no. 2C3, pp. 477 – 485, 2003. [Online]. Available: <http://www.sciencedirect.com/science/article/pii/S0301010403001241>
- [58] J. van Duijn, K. H. Kim, N. Hur, D. Adroja, M. A. Adams, Q. Z. Huang, M. Jaime, S.-W. Cheong, C. Broholm, and T. G. Perring, “Inhomogeneous level splitting in $\text{pr}_{2-x}\text{bi}_x\text{ru}_2\text{o}_7$,” *Phys. Rev. Lett.*, vol. 94, p. 177201, May 2005. [Online]. Available: <http://link.aps.org/doi/10.1103/PhysRevLett.94.177201>
- [59] J. Jensen and A. Mackintosh, *Rare earth magnetism: structures and excitations*, ser. International series of monographs on physics. Clarendon Press, 1991.

BIBLIOGRAPHY

- [60] G. A. Gehring and K. A. Gehring, “Co-operative jahn-teller effects,” *Rep. Prog. Phys.*, vol. 38, no. 1, p. 1, 1975. [Online]. Available: <http://stacks.iop.org/0034-4885/38/i=1/a=001>
- [61] K. Binder and A. P. Young, “Spin glasses: Experimental facts, theoretical concepts, and open questions,” *Rev. Mod. Phys.*, vol. 58, pp. 801–976, Oct 1986. [Online]. Available: <http://link.aps.org/doi/10.1103/RevModPhys.58.801>
- [62] L. Capriotti, A. E. Trumper, and S. Sorella, “Long-range néel order in the triangular heisenberg model,” *Phys. Rev. Lett.*, vol. 82, pp. 3899–3902, May 1999. [Online]. Available: <http://link.aps.org/doi/10.1103/PhysRevLett.82.3899>
- [63] R. Coldea, D. A. Tennant, and Z. Tylczynski, “Extended scattering continua characteristic of spin fractionalization in the two-dimensional frustrated quantum magnet cs_2cucl_4 observed by neutron scattering,” *Phys. Rev. B*, vol. 68, p. 134424, Oct 2003. [Online]. Available: <http://link.aps.org/doi/10.1103/PhysRevB.68.134424>
- [64] T. Ono, H. Tanaka, H. Aruga Katori, F. Ishikawa, H. Mitamura, and T. Goto, “Magnetization plateau in the frustrated quantum spin system cs_2cubr_4 ,” *Phys. Rev. B*, vol. 67, p. 104431, Mar 2003. [Online]. Available: <http://link.aps.org/doi/10.1103/PhysRevB.67.104431>
- [65] K. Takeda, K. Ubukoshi, T. Haseda, and K. Hirakawa, “Heat capacities of the

BIBLIOGRAPHY

- two-dimensional triangular heisenberg antiferromagnets Vx_2 (x; cl, br, and i),” *Journal of the Physical Society of Japan*, vol. 53, no. 4, pp. 1480–1486, 1984. [Online]. Available: <http://dx.doi.org/10.1143/JPSJ.53.1480>
- [66] A. Olariu, P. Mendels, F. Bert, B. G. Ueland, P. Schiffer, R. F. Berger, and R. J. Cava, “Unconventional dynamics in triangular heisenberg antiferromagnet NaCr_2O_4 ,” *Phys. Rev. Lett.*, vol. 97, p. 167203, Oct 2006. [Online]. Available: <http://link.aps.org/doi/10.1103/PhysRevLett.97.167203>
- [67] K. Kimura, H. Nakamura, K. Ohgushi, and T. Kimura, “Magnetoelectric control of spin-chiral ferroelectric domains in a triangular lattice antiferromagnet,” *Phys. Rev. B*, vol. 78, p. 140401, Oct 2008. [Online]. Available: <http://link.aps.org/doi/10.1103/PhysRevB.78.140401>
- [68] J. Park, J.-G. Park, G. S. Jeon, H.-Y. Choi, C. Lee, W. Jo, R. Bewley, K. A. McEwen, and T. G. Perring, “Magnetic ordering and spin-liquid state of YMnO_3 ,” *Phys. Rev. B*, vol. 68, p. 104426, Sep 2003. [Online]. Available: <http://link.aps.org/doi/10.1103/PhysRevB.68.104426>
- [69] T. McQueen, Q. Huang, J. W. Lynn, R. F. Berger, T. Klimczuk, B. G. Ueland, P. Schiffer, and R. J. Cava, “Magnetic structure and properties of the $s = 5/2$ triangular antiferromagnet $\alpha\text{-NaFeO}_2$,” *Phys. Rev. B*, vol. 76, p. 024420, Jul 2007. [Online]. Available: <http://link.aps.org/doi/10.1103/PhysRevB.76.024420>

BIBLIOGRAPHY

- [70] T. Kimura, J. C. Lashley, and A. P. Ramirez, “Inversion-symmetry breaking in the noncollinear magnetic phase of the triangular-lattice antiferromagnet CuFeO_2 ,” *Phys. Rev. B*, vol. 73, p. 220401, Jun 2006. [Online]. Available: <http://link.aps.org/doi/10.1103/PhysRevB.73.220401>
- [71] L. E. Svistov, A. I. Smirnov, L. A. Prozorova, O. A. Petrenko, L. N. Demianets, and A. Y. Shapiro, “Quasi-two-dimensional antiferromagnet on a triangular lattice $\text{RbFe}(\text{moo}_4)_2$,” *Phys. Rev. B*, vol. 67, p. 094434, Mar 2003. [Online]. Available: <http://link.aps.org/doi/10.1103/PhysRevB.67.094434>
- [72] R. Ishii, S. Tanaka, K. Onuma, Y. Nambu, M. Tokunaga, T. Sakakibara, N. Kawashima, Y. Maeno, C. Broholm, D. P. Gautreaux, J. Y. Chan, and S. Nakatsuji, “Successive phase transitions and phase diagrams for the quasi-two-dimensional easy-axis triangular antiferromagnet $\text{rb}_4\text{mn}(\text{moo}_4)_3$,” *EPL (Europhysics Letters)*, vol. 94, no. 1, p. 17001, 2011. [Online]. Available: <http://stacks.iop.org/0295-5075/94/i=1/a=17001>
- [73] S. E. Dutton, E. Climent-Pascual, P. W. Stephens, J. P. Hodges, A. Huq, C. L. Broholm, and R. J. Cava, “Helical magnetism and structural anomalies in triangular lattice $\alpha\text{-SrCr}_2\text{O}_4$,” *Journal of Physics: Condensed Matter*, vol. 23, no. 24, p. 246005, 2011. [Online]. Available: <http://stacks.iop.org/0953-8984/23/i=24/a=246005>
- [74] Y. Shimizu, K. Miyagawa, K. Kanoda, M. Maesato, and G. Saito,

BIBLIOGRAPHY

- “Spin liquid state in an organic mott insulator with a triangular lattice,”
Phys. Rev. Lett., vol. 91, p. 107001, Sep 2003. [Online]. Available:
<http://link.aps.org/doi/10.1103/PhysRevLett.91.107001>
- [75] T. Itou, A. Oyamada, S. Maegawa, M. Tamura, and R. Kato, “Quantum spin liquid in the spin-1m2 triangular antiferromagnet $\text{Etme}_3\text{Sb}[\text{Pd}(\text{dmit})_2]_2$,”
Phys. Rev. B, vol. 77, p. 104413, Mar 2008. [Online]. Available:
<http://link.aps.org/doi/10.1103/PhysRevB.77.104413>
- [76] S. Nakatsuji, Y. Nambu, H. Tonomura, O. Sakai, S. Jonas, C. Broholm, H. Tsunetsugu, Y. Qiu, and Y. Maeno, “Spin disorder on a triangular lattice,” *Science*, vol. 309, no. 5741, pp. 1697–1700, 2005. [Online]. Available:
<http://www.sciencemag.org/content/309/5741/1697.abstract>
- [77] S. Nakatsuji, H. Tonomura, K. Onuma, Y. Nambu, O. Sakai, Y. Maeno, R. T. Macaluso, and J. Y. Chan, “Spin disorder and order in quasi-2d triangular heisenberg antiferromagnets: Comparative study of fega_2s_4 , $\text{fe}_2\text{ga}_2\text{s}_5$, and niga_2s_4 ,” *Phys. Rev. Lett.*, vol. 99, p. 157203, Oct 2007. [Online]. Available:
<http://link.aps.org/doi/10.1103/PhysRevLett.99.157203>
- [78] D. E. MacLaughlin, Y. Nambu, S. Nakatsuji, R. H. Heffner, L. Shu, O. O. Bernal, and K. Ishida, “Unconventional spin freezing and fluctuations in the frustrated antiferromagnet niga_2s_4 ,” *Phys. Rev. B*, vol. 78, p. 220403, Dec 2008. [Online]. Available: <http://link.aps.org/doi/10.1103/PhysRevB.78.220403>

BIBLIOGRAPHY

- [79] H. Takeya, K. Ishida, K. Kitagawa, Y. Ihara, K. Onuma, Y. Maeno, Y. Nambu, S. Nakatsuji, D. E. MacLaughlin, A. Koda, and R. Kadono, “Spin dynamics and spin freezing behavior in the two-dimensional antiferromagnet NiGa_2S_4 revealed by ga-nmr, nqr and μSR measurements,” *Phys. Rev. B*, vol. 77, p. 054429, Feb 2008. [Online]. Available: <http://link.aps.org/doi/10.1103/PhysRevB.77.054429>
- [80] H. Yamaguchi, S. Kimura, M. Hagiwara, Y. Nambu, S. Nakatsuji, Y. Maeno, and K. Kindo, “High-field electron spin resonance in the two-dimensional triangular-lattice antiferromagnet niga_2s_4 ,” *Phys. Rev. B*, vol. 78, p. 180404, Nov 2008. [Online]. Available: <http://link.aps.org/doi/10.1103/PhysRevB.78.180404>
- [81] C. Stock, S. Jonas, C. Broholm, S. Nakatsuji, Y. Nambu, K. Onuma, Y. Maeno, and J.-H. Chung, “Neutron-scattering measurement of incommensurate short-range order in single crystals of the $s = 1$ triangular antiferromagnet niga_2s_4 ,” *Phys. Rev. Lett.*, vol. 105, p. 037402, Jul 2010. [Online]. Available: <http://link.aps.org/doi/10.1103/PhysRevLett.105.037402>
- [82] K. Takubo, T. Mizokawa, J.-Y. Son, Y. Nambu, S. Nakatsuji, and Y. Maeno, “Unusual superexchange pathways in an nis_2 triangular lattice with negative charge-transfer energy,” *Phys. Rev. Lett.*, vol. 99, p. 037203, Jul 2007. [Online]. Available: <http://link.aps.org/doi/10.1103/PhysRevLett.99.037203>

BIBLIOGRAPHY

- [83] I. I. Mazin, “Ab *initio* investigation of magnetic interactions in the frustrated triangular magnet NiGa_2S_4 ,” *Phys. Rev. B*, vol. 76, p. 140406, Oct 2007. [Online]. Available: <http://link.aps.org/doi/10.1103/PhysRevB.76.140406>
- [84] R. Tamura and N. Kawashima, “First-order phase transition with breaking of lattice rotation symmetry in continuous-spin model on triangular lattice,” *Journal of the Physical Society of Japan*, vol. 80, no. 7, p. 074008, 2011. [Online]. Available: <http://dx.doi.org/10.1143/JPSJ.80.074008>
- [85] H. Tsunetsugu and M. Arikawa, “Spin nematic phase in $s=1$ triangular antiferromagnets,” *Journal of the Physical Society of Japan*, vol. 75, no. 8, p. 083701, 2006. [Online]. Available: <http://dx.doi.org/10.1143/JPSJ.75.083701>
- [86] —, “The spin nematic state in triangular antiferromagnets,” *Journal of Physics: Condensed Matter*, vol. 19, no. 14, p. 145248, 2007. [Online]. Available: <http://stacks.iop.org/0953-8984/19/i=14/a=145248>
- [87] A. Läuchli, F. Mila, and K. Penc, “Quadrupolar phases of the $s = 1$ bilinear-biquadratic heisenberg model on the triangular lattice,” *Phys. Rev. Lett.*, vol. 97, p. 087205, Aug 2006. [Online]. Available: <http://link.aps.org/doi/10.1103/PhysRevLett.97.087205>
- [88] S. Bhattacharjee, V. B. Shenoy, and T. Senthil, “Possible ferro-spin nematic order in NiGa_2S_4 ,” *Phys. Rev. B*, vol. 74, p. 092406, Sep 2006. [Online]. Available: <http://link.aps.org/doi/10.1103/PhysRevB.74.092406>

BIBLIOGRAPHY

- [89] E. M. Stoudenmire, S. Trebst, and L. Balents, “Quadrupolar correlations and spin freezing in $s = 1$ triangular lattice antiferromagnets,” *Phys. Rev. B*, vol. 79, p. 214436, Jun 2009. [Online]. Available: <http://link.aps.org/doi/10.1103/PhysRevB.79.214436>
- [90] D. Podolsky and Y. B. Kim, “Halperin-saslow modes as the origin of the low-temperature anomaly in NiGa_2S_4 ,” *Phys. Rev. B*, vol. 79, p. 140402, Apr 2009. [Online]. Available: <http://link.aps.org/doi/10.1103/PhysRevB.79.140402>
- [91] H. Tsunetsugu and M. Arikawa, “Spin nematic phase in $s=1$ triangular antiferromagnets,” *Journal of the Physical Society of Japan*, vol. 75, no. 8, p. 083701, 2006. [Online]. Available: <http://dx.doi.org/10.1143/JPSJ.75.083701>
- [92] D. A. Tennant, R. A. Cowley, S. E. Nagler, and A. M. Tsvelik, “Measurement of the spin-excitation continuum in one-dimensional KCuF_3 using neutron scattering,” *Phys. Rev. B*, vol. 52, pp. 13 368–13 380, Nov 1995. [Online]. Available: <http://link.aps.org/doi/10.1103/PhysRevB.52.13368>
- [93] M. B. Stone, D. H. Reich, C. Broholm, K. Lefmann, C. Rischel, C. P. Landee, and M. M. Turnbull, “Extended quantum critical phase in a magnetized spin- $\frac{1}{2}$ antiferromagnetic chain,” *Phys. Rev. Lett.*, vol. 91, p. 037205, Jul 2003. [Online]. Available: <http://link.aps.org/doi/10.1103/PhysRevLett.91.037205>
- [94] M. Punk, D. Chowdhury, and S. Sachdev, “Topological excitations and the dynamic structure factor of spin liquids on the kagome lattice,” *Nature*

BIBLIOGRAPHY

- Physics*, vol. 10, no. 4, pp. 289–293, Mar. 2014. [Online]. Available: <http://www.nature.com/doi/10.1038/nphys2887>
- [95] S.-H. Lee, C. Broholm, G. Aeppli, A. P. Ramirez, T. G. Perring, C. J. Carlile, M. Adams, T. J. L. Jones, and B. Hessen, “Spin-glass and noncspin-glass features of a geometrically frustrated magnet,” *EPL (Europhysics Letters)*, vol. 35, no. 2, p. 127, 1996. [Online]. Available: <http://stacks.iop.org/0295-5075/35/i=2/a=127>
- [96] I. A. Zaliznyak, C. Broholm, M. Kibune, M. Nohara, and H. Takagi, “Anisotropic spin freezing in the $s=1/2$ zigzag chain compound SrCu_2 ,” *Phys. Rev. Lett.*, vol. 83, pp. 5370–5373, Dec 1999. [Online]. Available: <http://link.aps.org/doi/10.1103/PhysRevLett.83.5370>
- [97] I. S. Hagemann, Q. Huang, X. P. A. Gao, A. P. Ramirez, and R. J. Cava, “Geometric magnetic frustration in $\text{Ba}_2\text{Sn}_2\text{Ga}_3\text{ZnCr}_7\text{O}_{22}$: A two-dimensional spinel based kagomé lattice,” *Phys. Rev. Lett.*, vol. 86, pp. 894–897, Jan 2001. [Online]. Available: <http://link.aps.org/doi/10.1103/PhysRevLett.86.894>
- [98] Y. Okamoto, H. Yoshida, and Z. Hiroi, “Vesignieite $\text{BaCu}_3\text{V}_2\text{O}_8(\text{OH})_2$ as a candidate spin-1/2 kagome antiferromagnet,” *Journal of the Physical Society of Japan*, vol. 78, no. 3, p. 033701, 2009. [Online]. Available: <http://dx.doi.org/10.1143/JPSJ.78.033701>
- [99] H. Karunadasa, Q. Huang, B. G. Ueland, J. W. Lynn, P. Schiffer, K. A. Regan,

BIBLIOGRAPHY

- and R. J. Cava, “Honeycombs of triangles and magnetic frustration in SrL_2O_4 ($l = \text{Gd, dy, ho, er, tm, and yb}$),” *Phys. Rev. B*, vol. 71, p. 144414, Apr 2005. [Online]. Available: <http://link.aps.org/doi/10.1103/PhysRevB.71.144414>
- [100] S. Ghosh, H. D. Zhou, L. Balicas, S. Hill, J. S. Gardner, Y. Qiu, and C. R. Wiebe, “Short range ordering in the modified honeycomb lattice compound SrHo_2O_4 ,” *Journal of Physics: Condensed Matter*, vol. 23, no. 16, p. 164203, 2011. [Online]. Available: <http://stacks.iop.org/0953-8984/23/i=16/a=164203>
- [101] T. J. Hayes, O. Young, G. Balakrishnan, and O. A. Petrenko, “Magnetisation studies of geometrically frustrated antiferromagnets SrLn_2O_4 , with $\text{Ln} = \text{er, dy, and ho}$,” *Journal of the Physical Society of Japan*, vol. 81, no. 2, p. 024708, 2012. [Online]. Available: <http://dx.doi.org/10.1143/JPSJ.81.024708>
- [102] O. Young, L. C. Chapon, and O. A. Petrenko, “Low temperature magnetic structure of geometrically frustrated SrHo_2O_4 ,” *Journal of Physics: Conference Series*, vol. 391, no. 1, p. 012081, 2012. [Online]. Available: <http://stacks.iop.org/1742-6596/391/i=1/a=012081>
- [103] O. Young, A. R. Wildes, P. Manuel, B. Ouladdiaf, D. D. Khalyavin, G. Balakrishnan, and O. A. Petrenko, “Highly frustrated magnetism in SrHo_2O_4 : Coexistence of two types of short-range order,” *Phys. Rev. B*, vol. 88, p. 024411, Jul 2013. [Online]. Available: <http://link.aps.org/doi/10.1103/PhysRevB.88.024411>

BIBLIOGRAPHY

- [104] A. Fennell, V. Y. Pomjakushin, A. Uldry, B. Delley, B. Prévost, A. Désilets-Benoit, A. D. Bianchi, R. I. Bewley, B. R. Hansen, T. Klimczuk, R. J. Cava, and M. Kenzelmann, “Evidence for SrVO_4 and SrRu_2O_4 as model J_1 - J_2 zigzag chain materials,” *Phys. Rev. B*, vol. 89, p. 224511, Jun 2014. [Online]. Available: <http://link.aps.org/doi/10.1103/PhysRevB.89.224511>
- [105] T. Morita and T. Horiguchi, “Spin orderings of the one-dimensional ising magnet with the nearest and next nearest neighbor interaction,” *Physics Letters A*, vol. 38, no. 4, pp. 223 – 224, 1972. [Online]. Available: <http://www.sciencedirect.com/science/article/pii/0375960172900539>
- [106] R. Hornreich, R. Liebmann, H. Schuster, and W. Selke, “Lifshitz points in ising systems,” *Zeitschrift für Physik B Condensed Matter*, vol. 35, no. 1, pp. 91–97, 1979. [Online]. Available: <http://dx.doi.org/10.1007/BF01322086>
- [107] H. Kleinert, “Critical exponents from seven-loop strong-coupling φ^4 theory in three dimensions,” *Phys. Rev. D*, vol. 60, p. 085001, Sep 1999. [Online]. Available: <http://link.aps.org/doi/10.1103/PhysRevD.60.085001>
- [108] A. Wills, “A new protocol for the determination of magnetic structures using simulated annealing and representational analysis (sarah),” *Physica B: Condensed Matter*, vol. 276C278, no. 0, pp. 680 – 681, 2000. [Online]. Available: <http://www.sciencedirect.com/science/article/pii/S0921452699017226>
- [109] B. Willis and C. Carlile, *Experimental Neutron Scattering*. OUP Oxford, 2009.

BIBLIOGRAPHY

- [110] S. Lovesey, *Theory of neutron scattering from condensed matter*, ser. International series of monographs on physics. Clarendon Press, 1984.

Vita



Jiajia Wen was born in Wenzhou in southeast China on September 23rd 1986. He received his Bachelor degree in Mathematics and Physics from Tsinghua University (Beijing, China) in 2008, and enrolled in the Department of Physics and Astronomy Ph.D. program at Johns Hopkins University in the same year, where he studied low temperature magnetism in frustrated magnets under the supervision of Prof. Collin Broholm.

Starting in November 2014, Jiajia will continue his experimental research at Stanford University as a postdoctoral fellow.